In-situ Observation and Atomistic Modelling of Early Stage Oxidation / Corrosion Behavior of Nickel Base Alloys in Nuclear Power Plants

Jongjin Kim

Department of Nuclear Engineering

Graduate School of UNIST

2014

In-situ Observation and Atomistic Modelling of Early Stage Oxidation / Corrosion Behavior of Nickel Base Alloys in Nuclear Power Plants

Jongjin Kim

Department of Nuclear Engineering

Graduate School of UNIST

In-situ Observation and Atomistic Modelling of Early Stage Oxidation / Corrosion Behavior of Nickel Base Alloys in Nuclear Power Plants
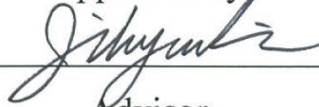
A thesis
submitted to the Graduate School of UNIST
in partial fulfillment of the
requirements for the degree of
Doctor of Philosophy of Science

Jongjin Kim

2. 4. 2014

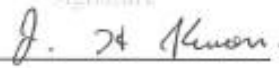Approved by

Advisor

Ji Hyun Kim

In-situ Observation and Atomistic Modelling of Early Stage Oxidation / Corrosion Behavior of Nickel Base Alloys in Nuclear Power Plants

Jongjin Kim

This certifies that the thesis of Jongjin Kim is approved.

2. 4. 2014

Advisor : Ji Hyun Kim

Jun Hyun Kwon

Chi Bum Bahn

Soon Yong Kwon

In Cheol Bang

ABSTRACT

Atomistic modelling and experimental observation has been conducted in order to investigate the early stage oxidation/corrosion behavior on nickel-base alloy in nuclear power plants. In order to fundamental study for the oxidation phenomena on the nickel, high resolution X-ray reflectivity is adopted. To examine the atomistic structure at the Ni(110)/NiO-liquid interface using X-ray reflectivity, the crystallinity of the Ni(110) surface is a very important parameter. To improve the surface crystallinity of Ni(110), the surface treatment by electro-polishing and sequential Ar sputtering/annealing in an ultra-high vacuum chamber is developed. After the successful surface pre-treatment, X-ray measurement at room temperature is conducted using synchrotron X-ray at advanced phonon source in US. Firstly, Crystal Truncation Rod(CTR) test for Ni(110)/NiO surface at room temperature condition in helium gas environment is conducted to obtain reference condition, and pure water is injected into the test cell to measure the water effects on the sample surface. CTR data was measurable with low errors even at lower intensity region. This CTR data also confirms that the surface pre-treatment procedure developed for Ni(110) is suitable for the surface X-ray study. According to results from helium gas environment, there are relaxed Ni layers on the Ni(110) surface with 5Å thickness and then there are stressed Ni + NiO layers on the relaxed Ni layers with 5 Å , and13Å NiO amorphous or polycrystalline layer formed on the top layer. While, the peak position and value is changed when the water is applied. In other word, the position and electron structure of Ni layer at the middle are changed due to the water contact. It can be considered that the water makes change the lattice structure of the Ni surface and NiO

To investigate the chromium effect on the oxidation behavior of Ni, atomistic modelling using first principle method is conducted. Using first principles approach, It has been simulated that the atomistic diffusion of oxygen in Ni-Cr binary alloy to understand the role of chromium during the oxidation of nickel-based alloys which are versatile in a wide range of application. The activation energy of oxygen diffusion is calculated by varying the number and position of the nearest-neighbor (NN) chromium atoms relative to oxygen along the diffusion pathway. The activation energy of oxygen diffusion is found to decrease with the increase in the number of NN chromium in front of oxygen, while that increases with

increase in the number of NN chromium at the back of oxygen. Therefore, in this study, the first principles calculation confirms the role of chromium as a barrier for the atomistic diffusion of oxygen in Ni-Cr binary alloy.

Finally, in-situ Raman spectroscopy has been applied in order to characterize the surface oxide film of nickel-base alloy/low alloy steel dissimilar metal weld interface in simulated primary water conditions of pressurized water reactors (PWRs). In order to directly examine the oxide film in high temperature aqueous conditions, an in-situ Raman spectroscopy system has been developed by constructing a hydrothermal optical cell with direct contact immersion optics.. For the verification of the constructed Raman system, high purity NiO, $NiFe_2O_4$, Cr_2O_3, and $NiCr_2O_4$ powders are examined to obtain reference spectra in room temperature air environment). The specimens were exposed to typical PWR water with 1,200ppm H_3BO_4 and 2 ppm of LiOH at a pressure of 15MPa and 300℃. In-situ Raman spectra were collected for interfaces of as-welded/thermally aged DMW in PWR water condition at 300℃ during 50hrs. Cr_2O_3, Fe_3O_4 and $FeCr_2O_3$ were measured on as-welded DMW, while $Fe_xNi_{1-x}Cr_2O_4$ and $NiFe_2O_4$ were measured on thermally aged DMW. From the ex-situ EDS measurements, the main compositions of the oxide layer after oxidation experiment are Ni and Cr on the as-welded Alloy152 and Fe for A533Gr.B, respectively, while Ni, Cr and Fe on the both of thermally aged Alloy152 and A533Gr.B. The difference of oxidation behavior by thermal aging was found and it was caused by diffusion-assisted chemistry redistribution by thermal aging. And the thermally aged DMW

Key words: Early stage of oxidation, X-ray reflectivity, First-principles, In-situ Raman spectroscopy, Nickel-base alloy, Thermal aging.

Contents

List of Figures

List of Tables

Nomenclature

Q	Momentum transfer
K	Wave vector
θ	Incident angle (°)
λ	Wavelength (m)
d	Bragg plane spacing (Å)
n	Diffraction order, (n=1,2,3,4…)
I	Scattered Intensity, (Arbitrary Unit)
F	Structure factor
c	Regular separation (Å)
f_0	Scattering strength
N	Layer number (N : integer)
V(r)	External potential
ε_j	Orbital energy
F	Structure factor of total structure
O [k]	Electron occupancy of kth atom [0~1]
f [k]	Scattering factor for kth atom
σ_0	Vibration amplitude
η	Attenuation factor
n(r)	Electron density (electrons per cubic bohr)

Subscripts

uc	Unit cell
CTR	Crystal Truncation Rod
Interface	Interface layer

IX

Surf	Surface layer
Ox	Oxide layer
l1	Amorphous layer 1
l2	Amorphous layer 2
w, water	Water layer
bar	Vibration amplitude of the water layer

I. Introduction

1.1 Background

Nickel-base alloys has been widely employed as tubing for steam generator and as penetration nozzles for reactor pressure vessel and pressurizer in many different types of water-cooled nuclear power plants because of its excellent resistance to aqueous corrosion at high temperature. After long-term use in power plants, environmental degradation problems in nickel-base alloys such as stress corrosion cracking, intergranular cracking and pitting corrosion etc. have been observed in reactor environment. Primary water stress corrosion cracking (PWSCC) is one of major degradation modes that occur in Ni-base structural materials for steam generators (SG's) or nozzles in the primary circuit of nuclear power plants. Figure 1-1 shows an example of PWSCC occurred in J-groove weld joint of A182/SS04 [1]. The PWSCC of Ni-base alloy has been observed to occur predominantly along grain boundaries and proceed in a direction roughly perpendicular to the tensile stress axis. The PWSCC of nickel base alloy and weld is directly related with safety concerns of nuclear power plant from the viewpoint that the SG tubing or nozzles may rupture as result of the cracking although alloy 600 components are protected against rupture by relatively large safety margins. Also, it has been intensified in recent years as Ni-base alloys display the increasing number of IGSCC events in components that are critical to the life extension of nuclear power plants. SCC is a complex phenomenon which is affected by synergetic interaction of metallurgical, mechanical and electrochemical parameters.

The PWSCC phenomenon of nickel base alloy has been extensively studied and several mechanistic models, based on slip dissolution/oxidation [2], internal oxidation[3, 4] and creep[5, 6] have been proposed to explain the underlying mechanisms that control IGSCC. Even though there is no general agreement on the mechanism of IGSCC, one common postulation from these studies is that the damage to the alloy substrate can be related to mass transport characteristics, rupture and/or repair properties of overlaying oxide film.

Possible mechanisms which are described above commonly include the formation and break of metal/alloy oxide. One common state in these models is that the damage to the metal/alloy substrate can be related to some transport or repair behavior of overlaying oxide film.

Furthermore, self-protection of metals and alloys to against corrosion in aqueous environments is succeeded by the growth of passive films on the surface. This surface property makes it possible that the sustainable development in numerous applications and industries where metals and alloys are used. Especially, technologically important transition metals including Cr, Fe, and Ni are protected in aqueous environments by ultrathin oxide or hydroxide layer. However, breakdown eventually occur

when the presence of aggressive species like chlorides or leads and it accelerated dissolution of the metals or alloys substrate at localized area.

For this reason, understanding the interfacial structure at solid-water interface and early stage corrosion and is very important to reveal the corrosion or oxidation behavior on the metal or alloy surface. The structural information is crucial to electrical double layer and ion exchange on the metal or alloy surface.

1.2 Goal and approach.

The main goal of this thesis is to understand the early stage oxidation/corrosion behavior on nickel-base alloys from atomistic modelling and in-situ experimental observation and to overcome the limitation of previous researches. Application of first principles within density functional theory is performed to understand the role of chromium on the oxygen diffusion in nickel-chromium binary alloy. To investigate the atomistic structure of Ni(110)/NiO-liquid interface, High resolution X-ray reflectivity technique using synchrotron X-ray source is adopted. Finally, in-situ Raman spectroscopy has been applied in order to characterize the surface oxide film of nickel-base alloy/low alloy steel dissimilar metal weld interface in simulated primary water conditions of pressurized water reactors (PWRs). Figure 1-2 shows a diagram which explains the goal and approaches to understanding the oxidation/corrosion behavior on nickel-base alloys in nuclear power plants
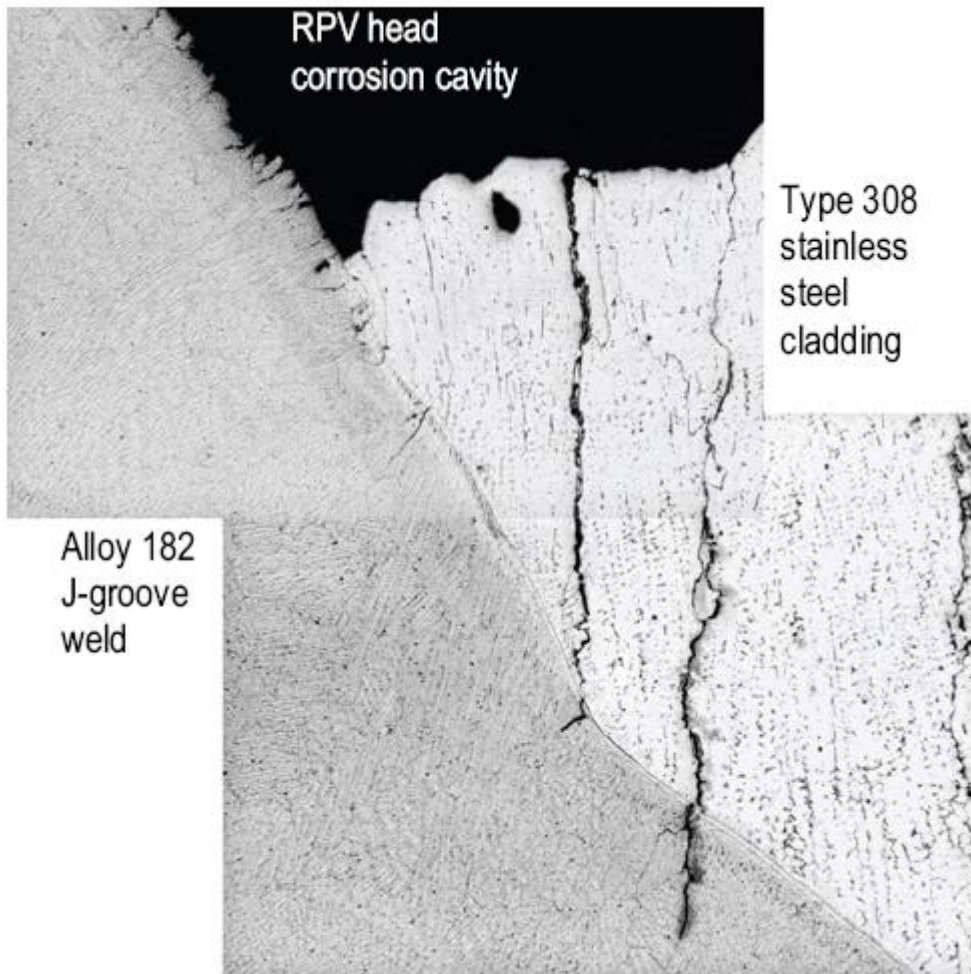
Figure 1-1. Micrograph of the interdendritic cracks initiated from the exposed cladding surface and extending into the J-groove weld. [1]

- Interfacial structure investigation of Ni(110)/NiO-water
- Synchrotron X-ray
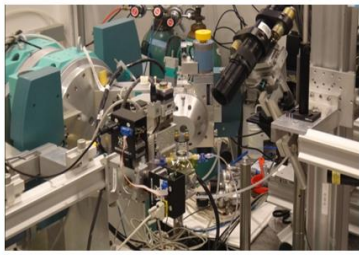
- Atomistic model for oxygen diffusion in Ni-Cr binary alloy
- First-principles

- In-situ oxide analysis on the Ni-base alloy /LAS DMW interface
- Raman spectroscopy
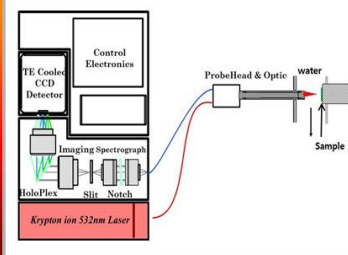
Mechanistic and Fundamental study on early stage oxidation/corrosion behavior on Nickel base alloys using Atomistic modelling and in-situ experimental observation methods

Figure 1-2. A diagram of goal and approach

II. Basic theory and literature study

2.1. High resolution X-ray reflectivity

There are many references about the X-ray reflectivity measurements. The basics of the X-ray reflectivity is summarized base on a user guide made by PA. Fenter [7]. Understanding the interference phenomena of waves is very important to understand the X-ray scattering phenomena. Interference is waves that are in phase add constructively, and waves that are out of phase destructively. Figure 2-1 shows a concept of destructive and constructive interference. The interference phenomenon is observed for all waves and even particles and can be demonstrated by the interference of waves on the surface and water.

The condition for constructive interference is obey the Bragg's law as shown in eq. (2-1)

$$n\lambda = 2d\sin(\theta) \tag{2-1}$$

And the Bragg's law describes the angles at which Bragg reflections occur for crystals as a function of the wave length, λ, the Bragg plane spacing, d, and the diffraction order, n. Figure 2-2 shows the geometry of scattering, and it is general for all Bragg diffraction condition.

Instead of describing interference condition in terms of angle, it is useful to describe the scattering process in "reciprocal space" in terms of momentum transfer, $\mathbf{Q}$, which is a vector consist of magnitude and direction. Equation (2-2) describes the $\mathbf{Q}$ with unit vector specifying the reflected or incident beam direction, $\mathbf{u_f}$ or $\mathbf{u_I}$, having a wave vector $\mathbf{K}=2\pi/\lambda$.

$$\mathbf{Q} = \mathbf{K}_f - \mathbf{K}_i = k(\mathbf{u}_f - \mathbf{u}_i) \tag{2-2}$$

$$Q = |\mathbf{Q}| = \frac{4\pi}{\lambda}\sin(2\theta/2) \tag{2-3}$$

Figure 2-3 shows the Bragg plane described in terms of Q. It allows for a simple description of single-crystal diffraction phenomena.

The scattered intensity is calculated by summing the scattered amplitudes, for each atoms j, in the sample through equation (2-4)

$$\mathbf{I} \propto \left|\sum \varepsilon_j\right|^2 = |F|^2 \tag{2-4}$$

where the magnitude of a complex number, ε, is written $|\varepsilon|^2 = \varepsilon\varepsilon^*$. The sum of all scattering amplitudes within the sample is called **structure factor, F**.

5

The "N-slit" diffraction pattern

The structure factor for N-slit layer is defined as following equation (2-5).

$$\mathbf{F} = f_0 \frac{\exp(-iNQc)-1}{\exp(-iQc)-1} = f_0 exp\left(\frac{-i(N-1)Qc}{2}\right)\left[\frac{\sin(\frac{NQc}{2})}{\sin(\frac{Qc}{2})}\right] \tag{2-5}$$

where the N layers having a regular separation, c, with each layer having a scattering strength f_0. Therefore, the scattering intensity is

$$\mathbf{I} \propto |F|^2 = |f_0|^2 \left[\frac{\sin(\frac{NQc}{2})}{\sin(\frac{Qc}{2})}\right] \tag{2-6}$$

Figure 2-4 shows the calculated scattering intensity as different layer number, N. The Bragg peaks appear at regular intervals and the intensity grows rapidly and develops into sharp Bragg peaks with increasing N. Because the peak intensity varies as , and the width varies as $|f_0|^2N^2$, and the width varies as $\Delta Q \sim 2\pi/(Nc)$. Thus, an integrated intensity that varies as $\sim |f_0|^2N$. Therefore, as N increase, the Bragg peaks become sharper and more intense.

The crystal truncation rod (CTR)

Sum of scattering intensity of semi-infinite lattice is nearly identical to that of the N-slit diffraction pattern with attenuation factor η.

$$\mathbf{F} = f_0 \frac{\eta^N \exp(-iNQc)-1}{\eta\exp(-iQc)-1} \tag{2-7}$$

assume that the structure factor is evaluated in the limit where N becomes very large, the $\eta^N = 0$, since $\eta < 1$. Therefore equation (2-7) can rewrite as follow.

$$\mathbf{F} = f_0 \frac{1}{1-\exp(-iQc)} \tag{2-8}$$

$$\mathbf{I}_{ctr} \propto |F|^2 = \frac{|f_0|^2}{4sin^2\left(\frac{Qc}{2}\right)} \tag{2-9}$$

The calculated intensity cab obtained equation (2-9) and figure 2-5 shows the calculated results of equation (2-9) as different separation number, c.

X-ray scattering was applied to the solid-liquid interface. The application of X-ray scattering to probe the structure of the mineral-water interface was pioneered by Chiarello et al.[8] with measurements of small angle X-ray reflectivity at the calcite-water interface, heteroepitaxial film growth on calcite, and high-resolution crystal truncation rod measurements [9]. These studies were performed for mineral water interface. For the metal-liquid interface, there are some problems regarding surface crystallinity. For this reason, high resolution X-ray reflectivity performed only for noble metals such as Au [10] or Pt [11]. Still, measurement of high X-ray reflectivity for metal-liquid interface is one of biggest challenges facing researchers. Medway et. al.[12] measured Ni(111) –liquid interface using Synchrotron X-ray. However, the measured data were not enough to analysis the interfacial structure. It is noted that the measured data in this study show enough considerable to analyze the atomistic structure of Ni(110)/NiO-water interface. Comparing Medway et. Al. study with results in this study, they measured the CTR for Ni(111) in KOH solution with 10^{-1}~10^{2} intensity range and there are no data point below 10^{-1} intensity. While the intensity range of the CTR data in this study is from 10^{-4} to 10^{1}, and the several data points in low intensity region ($<10^{-1}$) with low error were measured. The data in low intensity region contain key information of interface structure. For this reason, the interface structure can be defined not only NiO-liquid also Ni/NiO.In this study, the surface treatment were developed to improve the surface crystallinity then successfully measured the CTR data in order to clear analysis of Ni(110)/NiO-water interface.

2.2. First-principles method (density functional method)

The fundamental basis of density functional theory (DFT) is that ground state energy of a many electron system is a functional of the electron density, n(r). Therefore, the ground state energy of a system can be obtained by energy minimization with respect to n(r).

In 1926, Erwin Schrödinger published wave equation [13]. The Schrödinger equation contains all of the information available about a system. Unfortunately, most practical systems of interest consist of many interacting electrons, and the time effort to find solutions to Schrödinger's equation increases exponentially with the number of electrons. To solve this limitation, many physicists had developed many methods. [14, 15]

In 1964, Hohenberg and Kohn showed that the ground state total energy of a system of interacting electrons is a unique functional of the electron density[14]. By definition, a function returns a number when given a number.

In 1965, Kohn and Sham[15] made a significant breakthrough and simplify as Kohn-Sham equations. When they showed that the problem of many interacting electrons can be mapped exactly to a set of non-interacting electrons in an effective external potential.

$$\left(-\frac{1}{2}\nabla^2 + v_{\text{eff}}(r) - \varepsilon_j\right)\varphi_j(r) = 0 \qquad (2\text{-}10)$$

$$v_{\text{eff}}(r) = v(r) + \int \frac{n(r')}{|r-r'|}dr' + v_{xc}(r) \qquad (2\text{-}11)$$

where v(r) is the external potential and $v_{xc}(r)$ is the exchange-correlation potential, which depends on the entire density function. Eq. (2-10) can be solved. $\varphi j(\mathbf{r})$ corresponds to the jth KS orbital of energy ε_j. The ground state density is given by

$$n(r) = \sum_{j=1}^{N}\left|\varphi_j(r)\right|^2 \qquad (2\text{-}12)$$

Equation (2-10), (2-11) and (2-12) shows the results are self-consistent. The final ground state energy given by

$$E = \sum_j \varepsilon_j + E_{xc}[n(r)] - \int v_{xc}(r)ndr - \frac{1}{2}\int \frac{n(r)n(r')}{|r-r'|}dr'\,r \qquad (2\text{-}13)$$

where $E_{xc}[n(r)]$ is the exchange-correlation energy functional.

This Kohn-sham equation is solved self-consistently. Because the DFT formalism does not use any parameters except the electron density, it is called as first principles method (or ab-initio method).

Megchiche et al. [16] used first principles calculation to study the diffusion of oxygen in nickel along different diffusion pathways and focused on the thermal expansion effect on the diffusion. They calculated the activation energy of oxygen diffusion in nickel along the octahedral to octahedral pathway and octahedral-tetrahedral-octahedral pathway, and considered the thermal expansion effects using change in lattice parameter as temperature. Figure 2-6 shows their representative result.

Very few studies have been attempted on bimetal alloys such as NiAl [17, 18] . These studies focused on the diffusion of nickel atom in NiAl to see the effect of defect complex. Choudhury et al.[19] used first principles method to model the diffusion in dilute bcc Fe-Ni and Fe-Cr alloys and found a relationship between vacancy/interstitial self-diffusion. Although the chromium contents in nickel base alloys take important role of crack resistance, there are no researches focused on the Ni-Cr binary alloys. Therefore, this study focused on the investigation of the effect of chromium on the diffusion of oxygen in Ni-Cr alloy. The activation energy was calculated by varying the chromium position in the supercell, and the effect of the number of nearest-neighbor (NN) chromium atoms with respect to oxygen was also considered herein.

2.3. Raman spectroscopy

C.V. Raman discovered another type of light scattering in which the frequency changes when the light is scattered. The frequency changes occur when some of energy of the scattered light is taken up by molecule, which is excited into vibration motion. It is the frequency changes of the inelastic scattered light that contains important information related the chemical and structural states. Raman shifted photons can be of either higher or lower energy, depending upon the vibrational state of the molecule under study. Figure 2-7 shows an energy diagram that illustrates these concepts.

The molecule must be symmetric to observe the Raman shift. When the photon is released the molecule relaxes back into vibrational energy state. The molecule will typically relax into the first vibration energy state, and this generates Stokes Raman scattering. If the molecule was already in an elevated vibrational energy state, the Raman scattering is then called Anti-Stokes Raman scattering

Several researchers performed oxide analysis using Raman spectroscopy in aqueous condition. Kumai and Devine [20, 21] conducted the measurements of oxide films by in-situ Raman spectroscopy of aqueous corrosion of pure iron and iron base alloy at high temperature waters. Stainless Steel 304 and Fe-10Ni-xCr as variation of chromium contents at high temperature water were investigated. Also, the effects of several different ranges of dissolved oxygen concentrations ranging from 0 to 208 ppb were studied. They performed surface enhanced Raman technique using noble metal such as gold or silver. Figure 2-8 and 2-9 show the representative results of their study.

Maslar et al. [22-25] have made observations of aqueous corrosion of pure metals (Fe, Ni and Cr) and stainless steels in air saturated and high temperature water conditions. Figure 2-10, 2-11 show their results of in-situ Raman spectroscopic investigation on aqueous corrosion of chromium metal and stainless steel. And J.H. Kim and I.S. Hwang [26] developed an in situ Raman spectra system for surface oxide films on metals and alloys in high temperature water, and they performed in-situ oxide analysis on Alloy600 in PWR primary water conditions with variation of dissolved hydrogen concentration and stress level. Figure 2-12 shows the results of in-situ Raman spectra for Alloy600 in PWR primary water condition.

No one measured the Raman spectra for interface region of dissimilar metal weld. In this study, the in-situ oxide film analysis was performed for interface region of nickel base alloy /low alloy steel dissimilar metal weld in PWR primary water condition. Also, thermal aging effect on the oxide films was investigated.

Destructive   **Constructive**
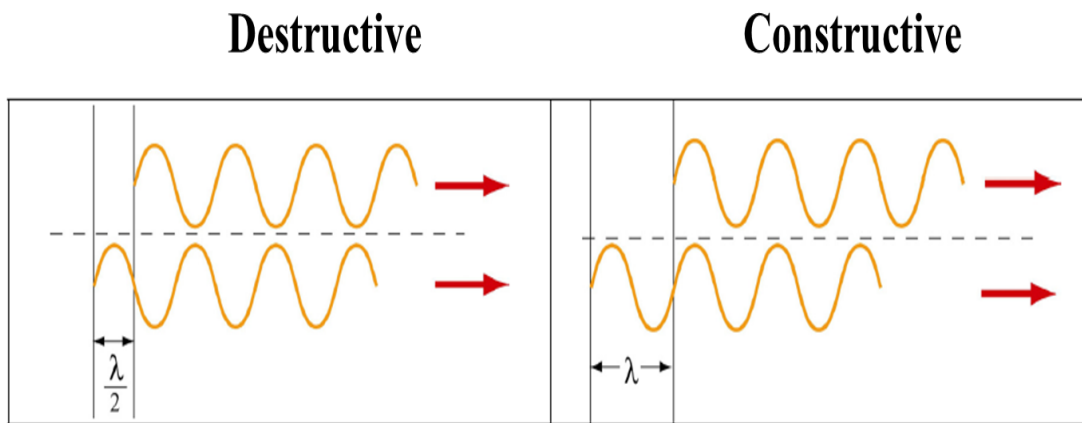
Figure 2-1. Destructive and constructive interference
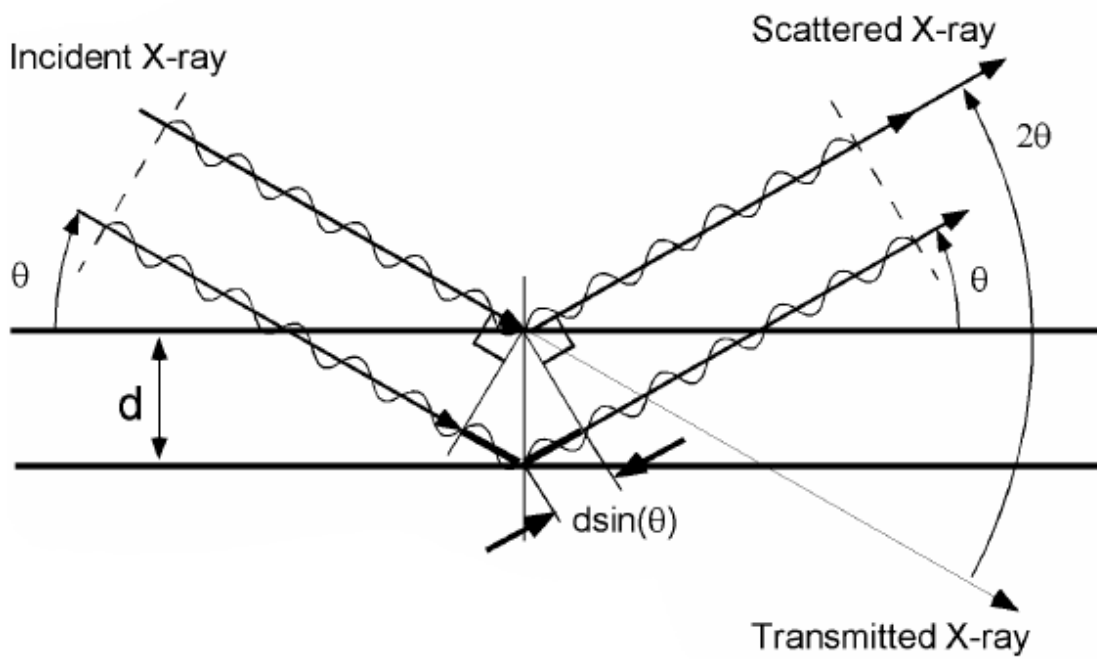
Figure 2-2. The Bragg scattering geometry [7]
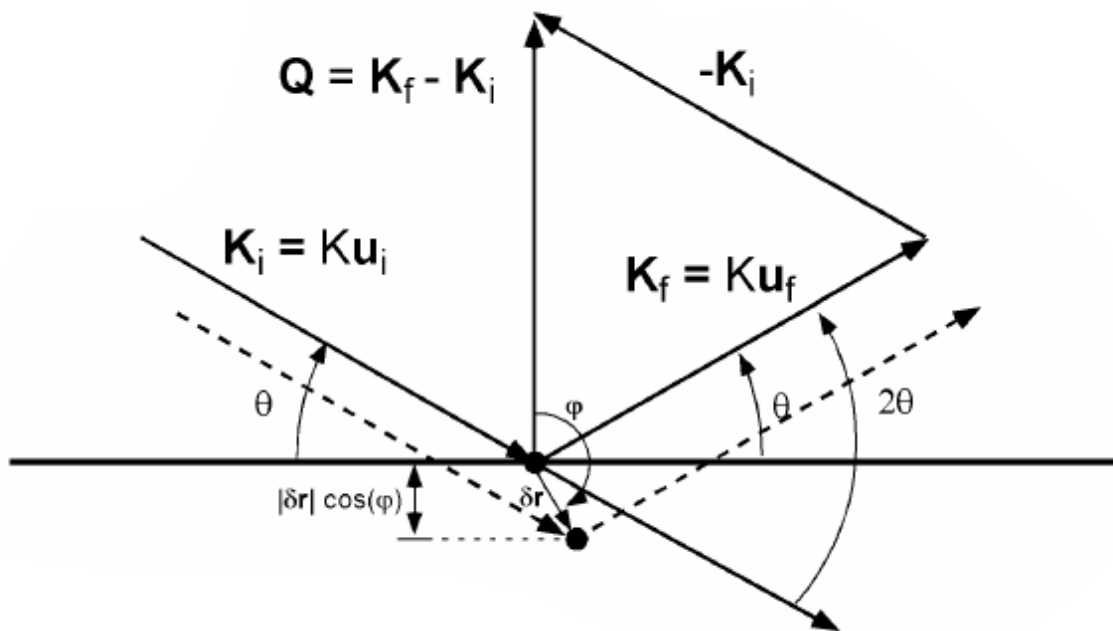
Figure 2-3 The Bragg plane described with momentum transfer, **Q [7]**
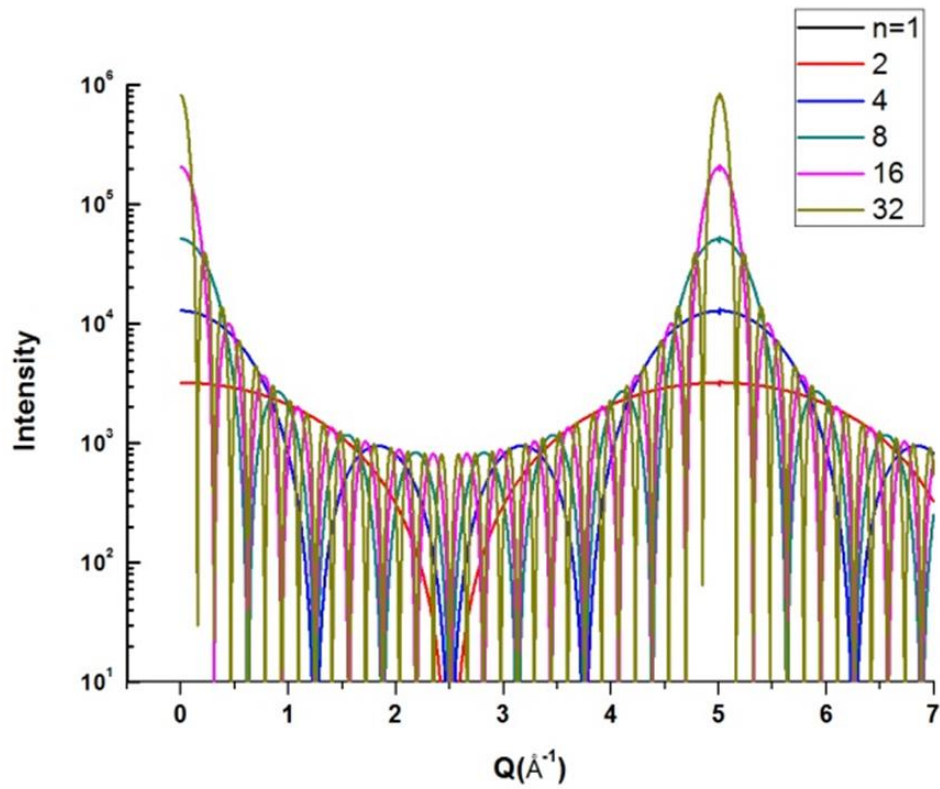
Figure 2-4 Calculated scattering intensity as different layer number, N.
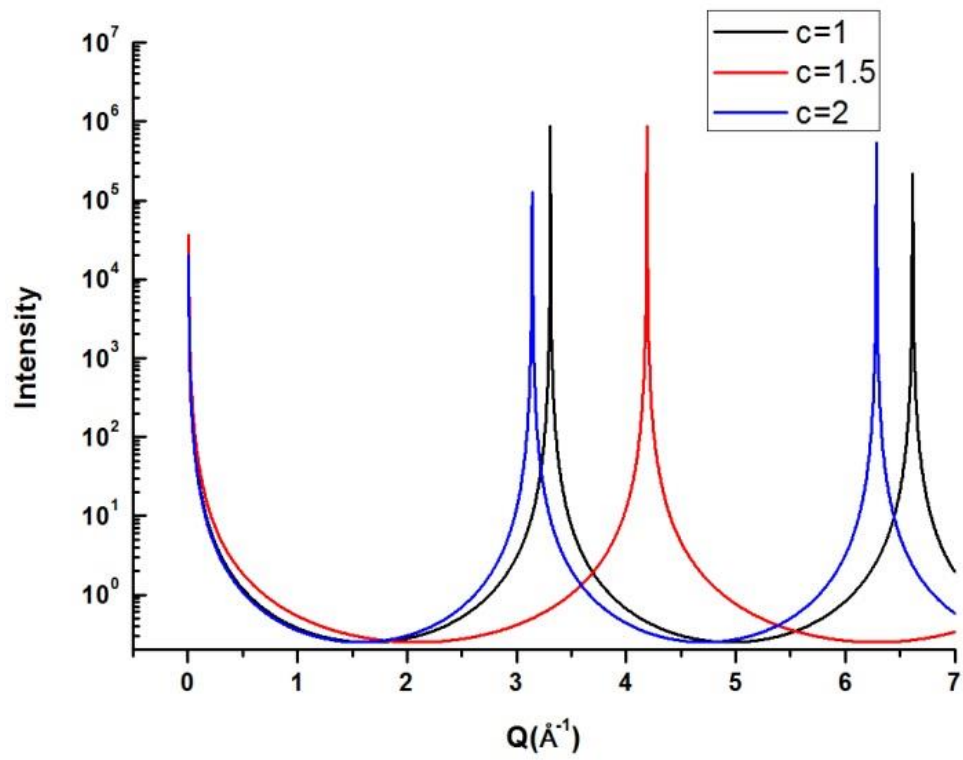
Figure 2-5. Calculated scattering intensity as different separation number, c
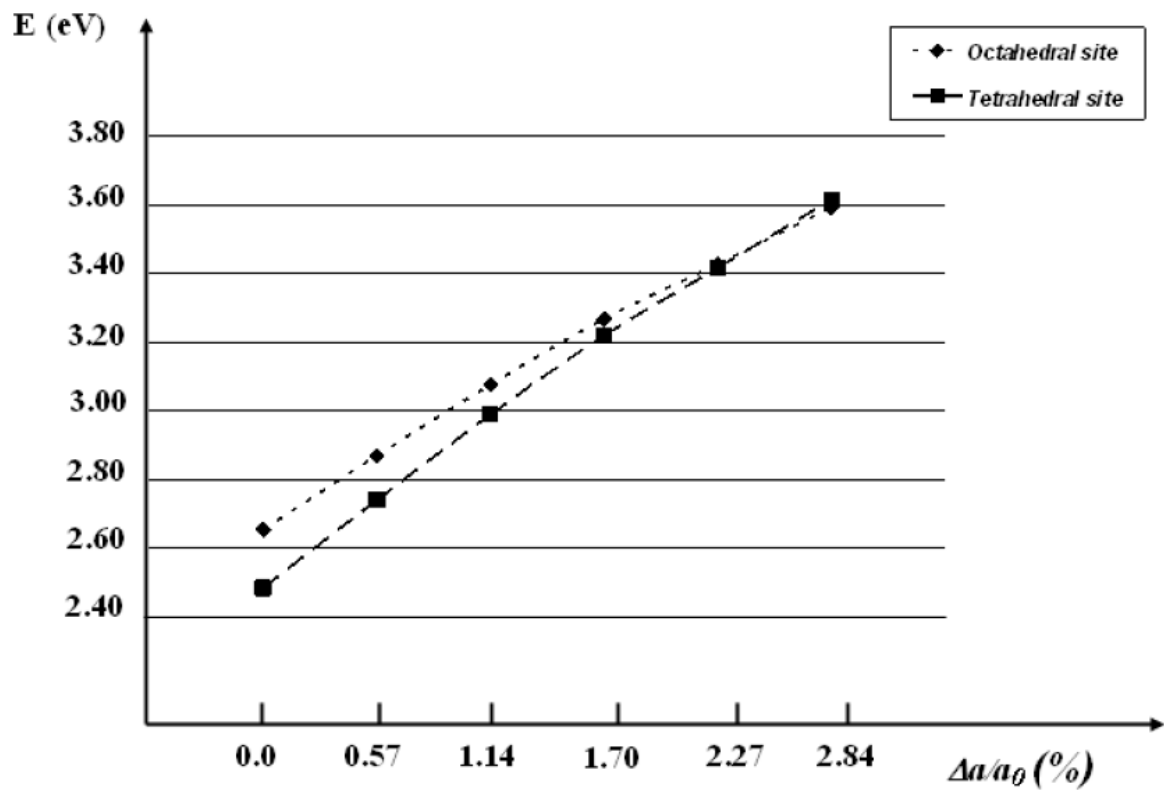
Figure 2-6 Octahedral and tetrahedral insertion energy variations with the linear thermal expansion. [16]
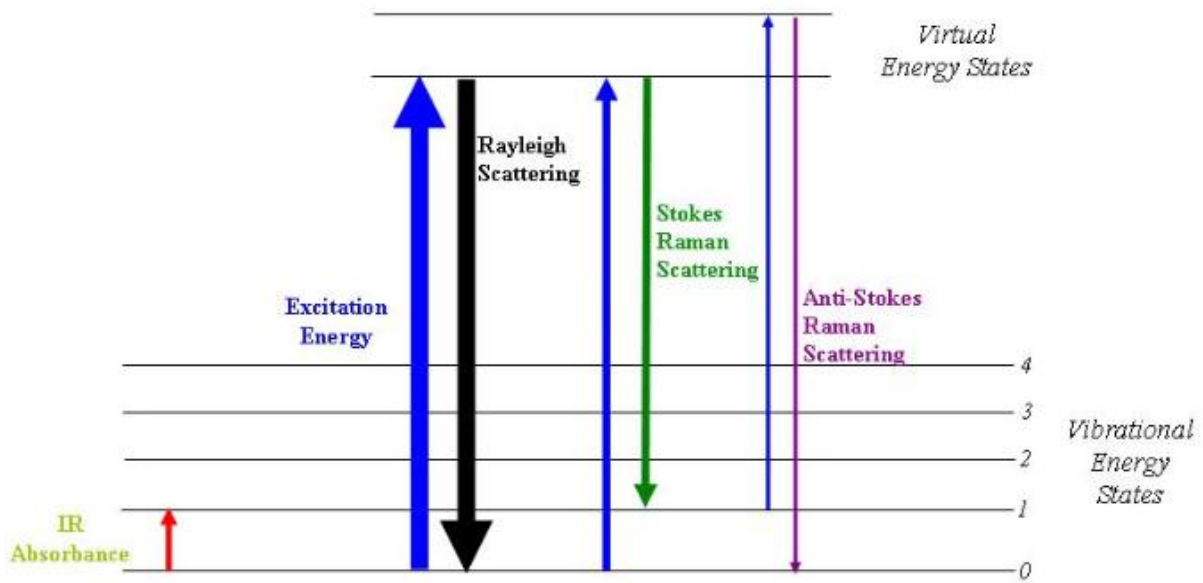
Figure 2-7. Energy diagram of Raman spectroscopy
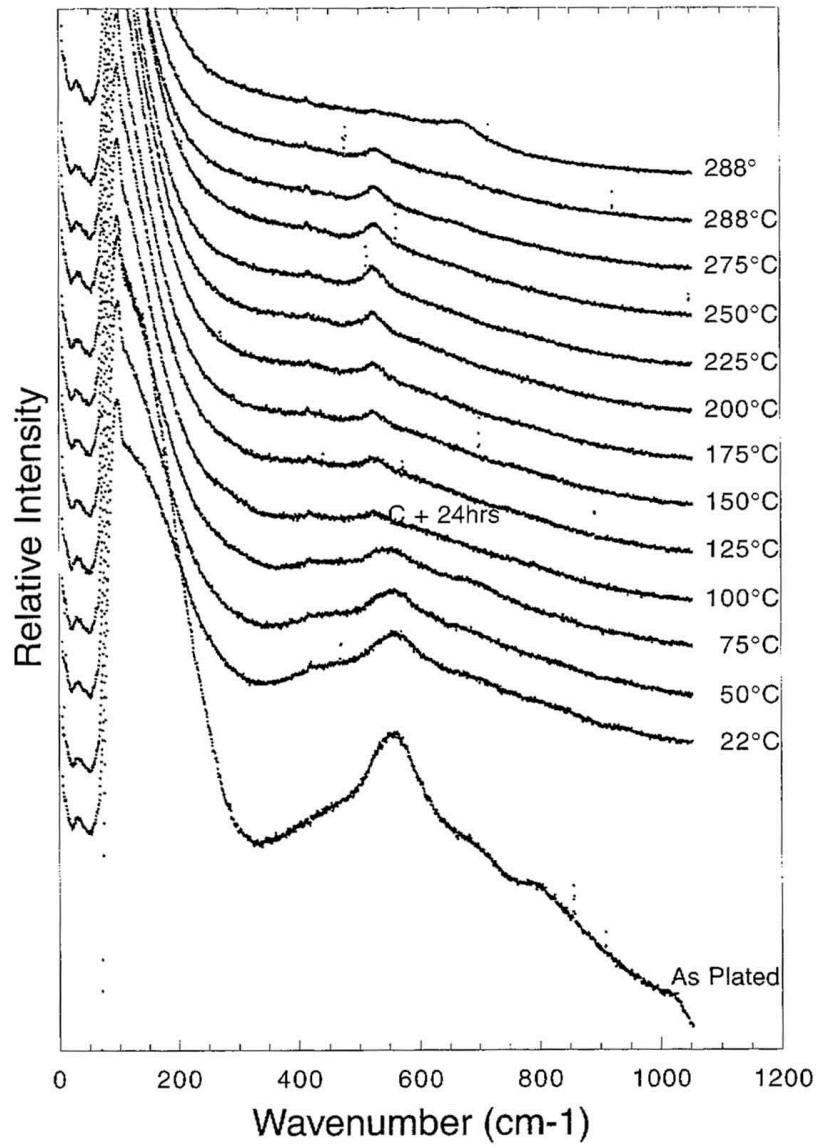
Figure 2-8. Surface enhanced Raman spectra of SS304 during sample preparation and heating to 288℃ in deaerated water. [21]
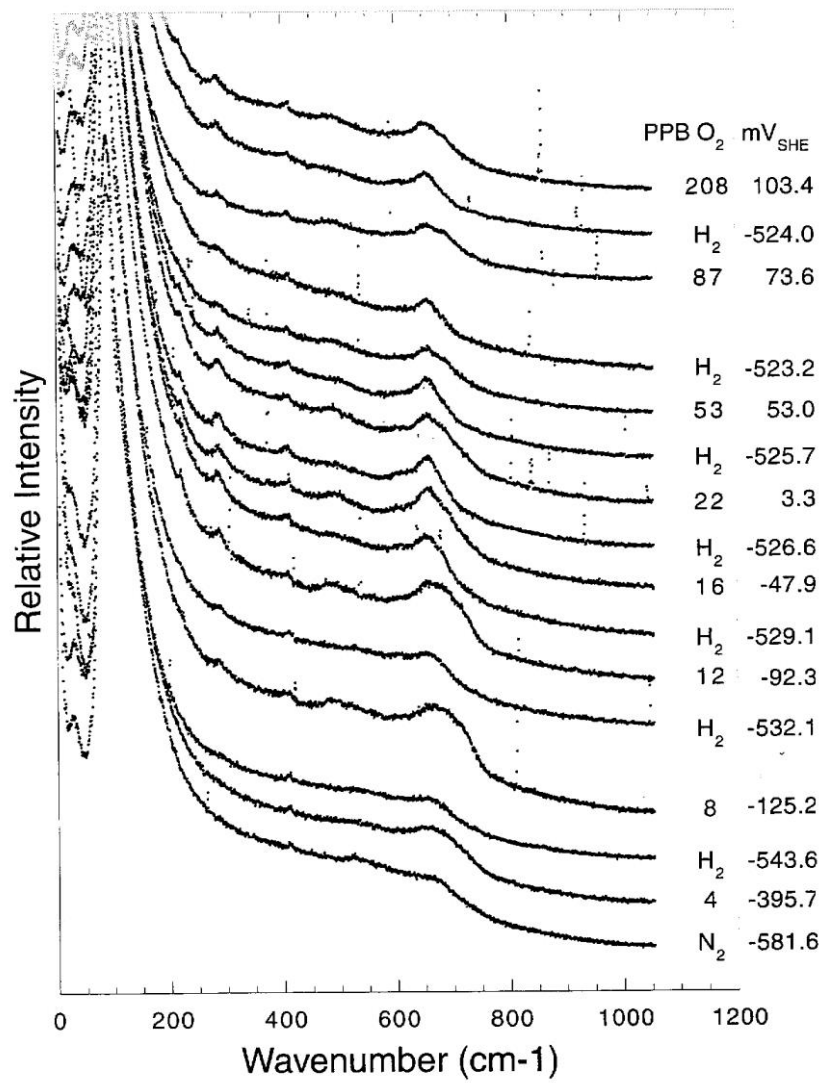
Figure 2-9. Surface enhanced Raman spectra of SS304 during oxygen/hydrogen cycling at 288 ℃. [21]
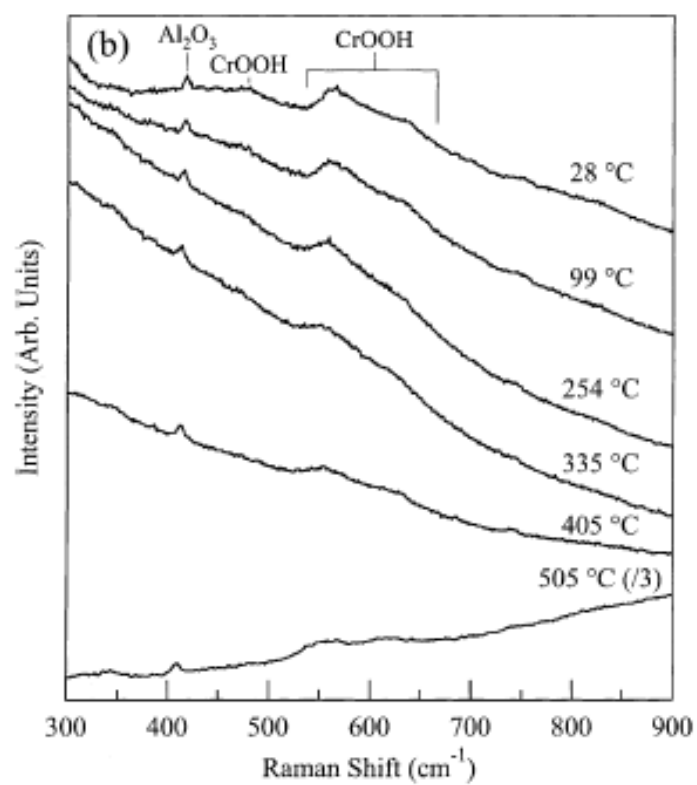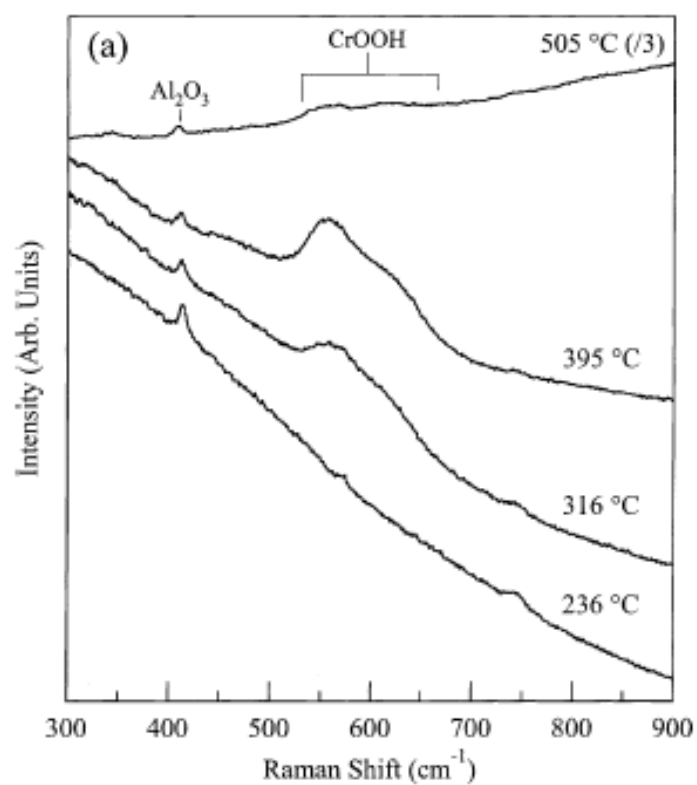
Figure 2-10. In –situ Raman spectra of chromium as it was (a) heated to 505℃ and (b) cooled to 28℃ ［22］
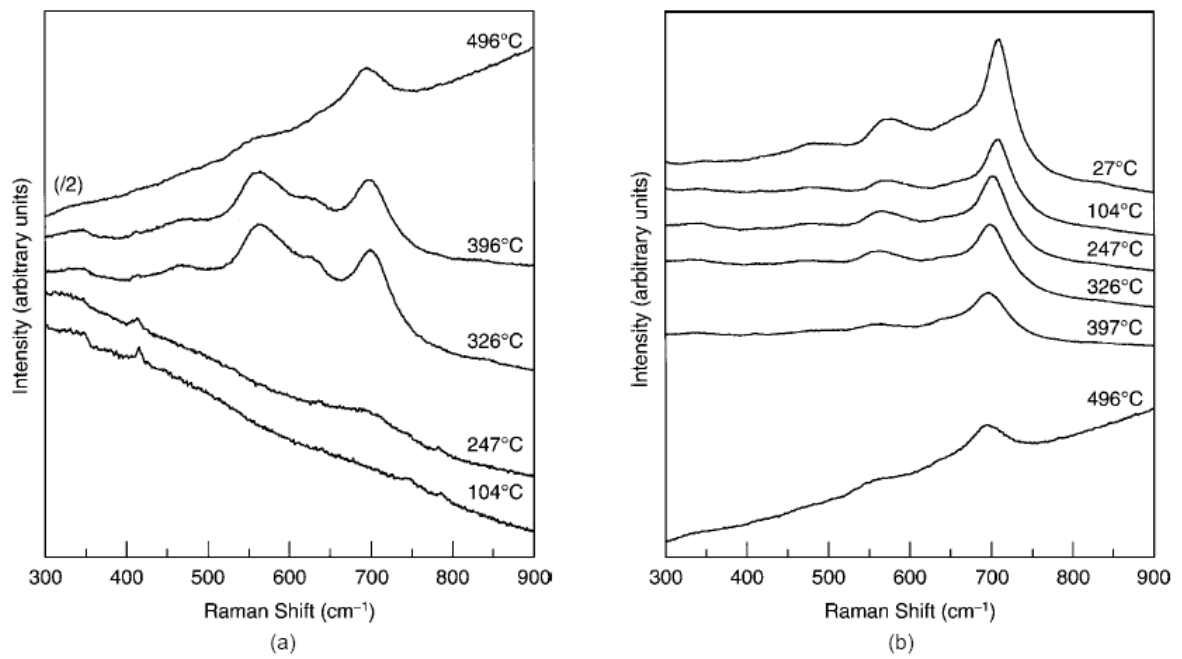
Figure 2-11. In –situ Raman spectra recorded as the Type304L was (a) heated to 496℃ and (b) cooled to 27℃ [23]
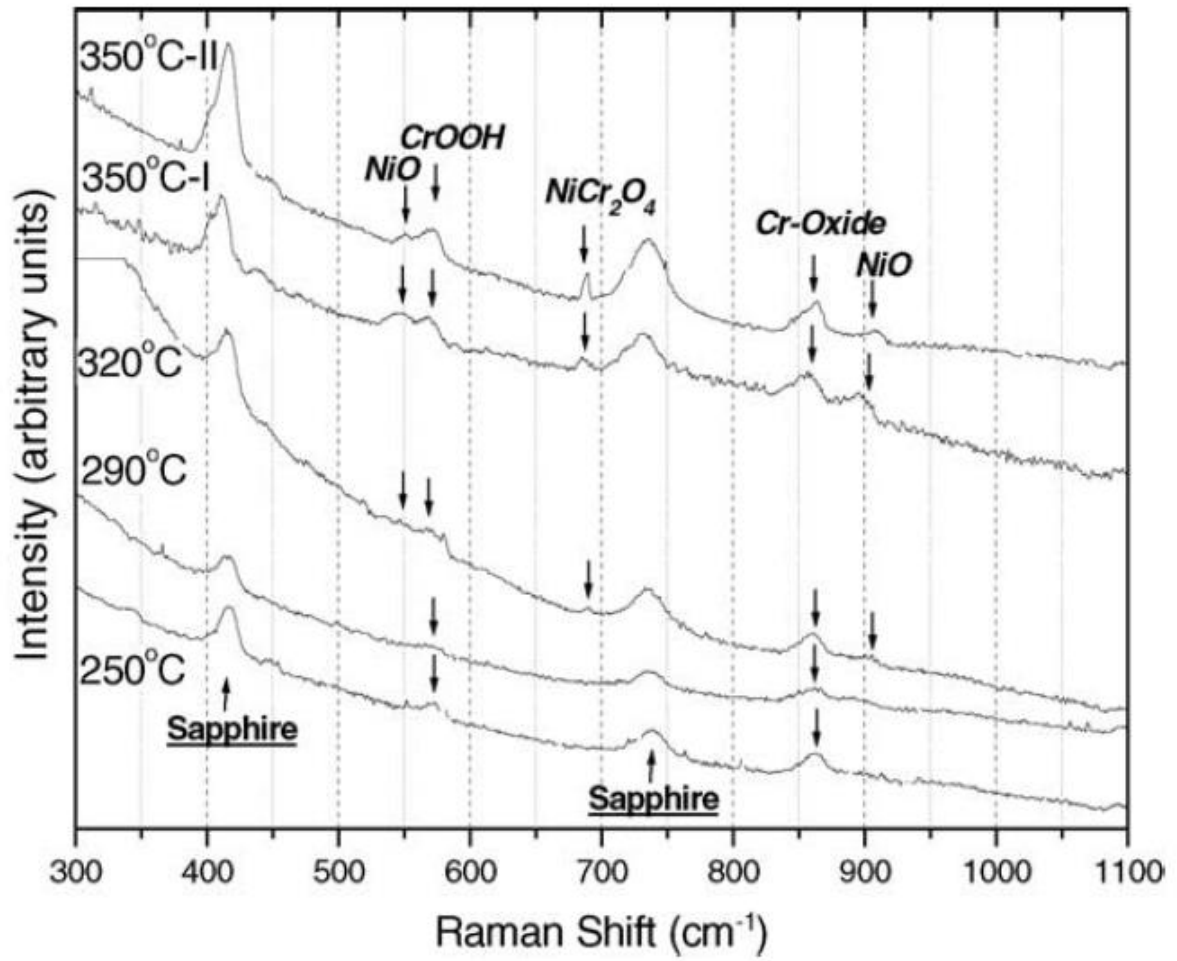
Figure 2-12. In –situ Raman spectra obtained for Alloy600 by holding at 250, 290, 320, and 350 ℃ in PWR water condition with $DH_2 = 30$ cm^3 (STP)/kg. [26]

III. Methods

3.1. In-situ X-ray reflectivity study of interfacial structure between the pre-oxidized Ni(110) surface and deionized water

3.1.1 Introduction

Self-protection of metals and alloys to against corrosion in aqueous environments is succeeded by the growth of passive films on the surface. This surface property makes it possible that the sustainable development in numerous applications and industries where metals and alloys are used. Especially, technologically important transition metals including Cr, Fe, and Ni are protected in aqueous environments by ultrathin oxide or hydroxide layer. However, breakdown eventually occur when the presence of aggressive species like chlorides or leads and it accelerated dissolution of the metals or alloys substrate at localized area.

For this reason, understanding the interfacial structure at solid-water interface is very important to reveal the corrosion or oxidation behavior on the metal or alloy surface. The structural information is crucial to electrical double layer and ion exchange on the metal or alloy surface.

Various studies have been carried out on the surface structures of Ni single crystals in aqueous condition by ex-situ [27, 28] and in-situ [29, 30] Scanning Tunneling Microscope(STM), X-ray-scattering [31], and electrochemical STM study [32]. These test revealed the epitaxial relationship between Ni substrate and the oxide layer as well as those structures.

The passive film structures formed on nickel can be explain by a layer model with inner layer consisting of NiO and the outer layer is a hydroxylated NiO surface or a 3D nickel hydroxide $(Ni(OH)_2)$ layer. [33, 34]

Recently, it is summarized that the nickel exposure to oxygen at room temperature leads to three defined reaction region dependent on the oxygen exposure. The first is the dissociative chemisorption of oxygen on Ni at low exposure. And the second reaction region is NiO nucleation and lateral growth. And thickening of the oxide with the time is last reaction [34]. However, still the resolution of the initial structural data of interface between water and pre oxidized Ni(110) surface is not clear.

To solve this limitation, powerful analytical methods have been established in the past decade based on the high-resolution x-ray reflectivity [35], the resonant anomalous x-ray reflectivity (RAXR) [36] and the x-ray standing wave (XSW) [37] for probing the interfacial structure and the ion-specific density distribution in molecular scale. Various process studies have been performed based on these structure measuring techniques for dissolution kinetics and ion adsorption thermodynamics [38-40].

23

Furthermore, according to the advancement in computer science technology, many researchers have begun focusing on oxidation phenomena. Bouzoubaa et al. [41] investigated the role of surface steps on the interaction of chloride ions with hydroxylated NiO surfaces characteristic of the barrier oxide layer formed on passivated nickel using periodic density functional theory calculation, and Taylor et al [42]. applied the first-principles methods to the determination of water stability over various metal surfaces. These studies provide reasonable agreement with experimental study, and helped understand scientific fundamental phenomena.

Therefore, the objective in this study was to obtain detailed structural data between pre-oxidized Ni(110) and water interfaces to investigate the mechanism of growth the passive film formed on Ni(110) by In-situ high energy X-ray reflectivity study and simulated atomistic model.

3.1.2. Surface treatment

Ni(110) single crystal from a Ni single crystal rod(99.99%, fabricated by Princeton Scientific Corp.) was used. The orientation of the specimen was verified within ±0.01° and the diameter and thickness is 10.00mm and 1.00mm, respectively.

The specimen pretreated. Firstly, the Ni(110) was mechanically polished with a final grade of 0.25μm alumina powder and then it was electropolished at 2~2.5A and ~50V in mixture solution of 30% nitric acid and 70% methanol cooled by dry ice up to 50sec. After polishing, To improve the surface crystallinity of Ni(110), the specimen inserted into an ultra-high vacuum chamber at 33ID-E beamline of Advanced Photon Source(APS) to clean the sample by sputtering with Ar+ and annealing in vacuum at 700℃. Ni(110) specimen mounted on a sample holder of the vacuum chamber is shown in figure 3-1. The cleaned Ni surface is exposed to high-purity oxygen to grow a coalesced NiO layer and the reconstructed surface phase initially characterized using Reflection High-Energy Electron Diffraction (RHEED) before and after each sputtering/annealing cycle. . Figure 3-2 (a) shows RHEED images after the electropolishing and each cycle. Before the sputtering/annealing, the RHEED image shows no crystalline information on the surface. After the 1st cycle, as shown in Figure 3-2 (b), RHEED image clearly shows streak, spots, and Kikuchi lines, suggesting the Ni(110) surface crystallinity was improved. The subsequent cycle appeared to improve the surface crystallinity further, but after the 4th cycle only marginal improvement was observed. Figure 3-2 (f) shows the RHEED image after the 4th cycle with a different electron beam angle from others. The RHEED image shows multiple parallel streaks, which are typically observed with practically flat metal surface As previous data without fine surface pretreatment showed only marginal x-ray reflectivity data quality [12], this procedure is expected to enhance the data quality substantially.

24

3.1.3. High resolution X-ray reflectivity measurements

After the successful surface pre-treatment, high-resolution X-ray reflectivity (or Crystal Truncation Rod) measurements at room temperature were conducted at 5ID-D beamline of APS to determine the interfacial structure between the pre-oxidized Ni surface and deionized water. The Ni sample was transported into an aqueous thin-film cell. The measurement of X-ray reflectivity or crystal truncation rod is fundamentally limited by the incident photon flux as the reflectivity varies several orders of magnitudes as function of reflection angle. Due to the attenuation of water, the X-ray energy should be high around 20KeV. The APS synchrotron sources provide high photon flux and high quality of beam maintenance for this flux-limited and alignment-sensitive experiment.

The CTR measurement was performed for Ni(110)/NiO in helium condition, after that, the water injected on the surface, then CTR measurement was conducted to the Ni(110)/NiO-water interface also. Figure 3-3 shows the CTR measurement of the Ni(110)/NiO-water interface.

3.2. Atomistic modelling of oxygen diffusion in Ni-Cr binary alloy using first-principles calculation

3.2.1 Introduction

Nickel-chromium alloys are widely used in modern industries because of their ability to withstand a wide variety of severe operating conditions, including corrosive environment, high temperature, high stress, and a combination of these factors [43]. Many experimental studies [44-46] have shown that chromium forms a thin but dense protective oxide surface layer, which prevents oxygen from diffusing into the underlying material even at high temperatures. Therefore, chromium is commonly added to nickel-based alloys and stainless steels to provide excellent high-temperature performance.

However, nickel-based alloys conventionally suffer from stress corrosion cracking (SCC) [47] Hence, it is critically important to investigate and understand the mechanisms of SCC in nickel-based alloys to find preventive measures. A significant amount of research has been performed to understand and unravel the mechanism governing SCC in nickel-based alloys. In result, several different hypotheses delineating the process of and ways to prevent SCC have been suggested. However, there are some limitations in explaining the mechanisms underlying SCC in nickel-based alloys.

Recently, thanks to the advancements in computer technology, many researchers have begun focusing on atomistic modeling and simulation methods as alternatives for evaluating the mechanical and thermodynamic properties of metals and alloys. These techniques use calculation methods such as finite element, molecular dynamics [48] and first principles (or ab initio) simulations [49, 50] For instance, Young et al.[51] and Garruchet et al. [52] evaluated the activation energy of diffusion and diffusivity of oxygen in nickel using first-principles and variable-charge molecular dynamics simulations, respectively. Megchiche et al. [16] used first principles calculation to study the diffusion of oxygen in nickel along different diffusion pathways and focused on the thermal expansion effect on the diffusion. Very few studies have been attempted on bimetal alloys such as NiAl [17, 18] . These studies focused on the diffusion of nickel atom in NiAl to see the effect of defect complex. Choudhury et al.[19] used first principles method to model the diffusion in dilute bcc Fe-Ni and Fe-Cr alloys and found a relationship between vacancy/interstitial self-diffusion.

However, as can be noted, all these studies have concentrated on either the diffusion of oxygen in pure Ni or the self-diffusion of metal elements in bimetal alloys. In order to fully understand SCC in Ni-Cr alloys and other nickel-based alloys, we need to extend the focus from pure Ni to Ni-Cr binary system or Ni-Cr-Fe ternary system, because according to experimental data

reported by Laghoutaris et al. [53], the increase in chromium concentration in nickel-based alloys tends to reduce the growth rate of SCC.

Therefore, this study is aimed at realizing the role of chromium in oxidation/corrosion behavior of nickel-based alloys by simulating the diffusion of oxygen in Ni-Cr binary alloy using the first principles method. Specifically, this study focused on the investigation of the effect of chromium on the diffusion of oxygen in Ni-Cr alloy. The activation energy was calculated by varying the chromium position in the supercell, and the effect of the number of nearest-neighbor (NN) chromium atoms with respect to oxygen was also considered herein

3.2.2. Computational method

Atomistic modeling and the calculation were performed by using the Vienna ab initio Simulation Package (VASP) [54, 55]. The modeling framework adopted to calculate the activation energy of oxygen diffusion in nickel using single NN chromium has been described in detail elsewhere [56]. All calculations consider the spin-polarization, and the density functional theory (DFT) was used to calculate the total energies, forces, and energy profiles. Kohn and Sham [57] introduced a method of expressing density as the sum of squared single particle wave functions, with the single particles being fictitiously non-interacting electrons. According to DFT theory, the ground state energy of a system can be obtained by minimizing the energy with respect to the electron density. This is due to the fact that the ground state energy of a system of electrons could be calculated as a function of the electron density.

The projected-augmented wave (PAW) method [58, 59] and the generalized gradient approximation (GGA), which introduces an additional term in the exchange and correlation energy depending on the local gradient of the electronic density, were used with the exchange-correlation functional of Perdew and Wang (PW91) [60]. The PAW formalism is a complex pseudorization scheme close in spirit to the ultrasoft scheme. However, it allows the reconstruction of the real electronic density and the real wave functions with all their oscillations. Because of this reason, this method is expected to increase the efficiency of computational time. Furthermore, in recent theoretical studies such as local density approximation (LDA) to calculate various properties of nickel [61] and the formation and migration enthalpies of vacancies in nickel [62]. the GGA method showed higher accuracy than did other approximation methods. Monkhost-Pack [63] k-point meshes of $5 \times 5 \times 5$ were used to test the Brillouin zone in the reciprocal space, and 400 eV was set as plan-wave cut-off energy.

A supercell consisting of 28 nickel atoms and 4 chromium atoms was adopted for the current

study of Ni-Cr binary alloy. This supercell represents one of the widely used Ni-based structural alloys, namely, alloy 600, which is mainly composed of 72 wt% nickel atoms, 15 wt% chromium atoms, and other minor elements. Changing the wt% to at%, the supercell contained 28 nickel atoms and 4 chromium atoms for calculation with symmetric lattice. As shown in figure 3-4, oxygen diffusion in FCC metals and alloys can take two different pathways. The oxygen atom can pass through an adjacent tetrahedral (T) site via a face of the octahedron (O), which is called as O-T-O path, as represented by short tilted arrows in figure 3-4. Alternatively, oxygen atom can diffuse from one octahedral (O) site to adjacent octahedral (O) site directly which is called as O-O path, as represented by long horizontal arrow in figure 3-4

In order to determine the diffusivity of oxygen in Ni-Cr binary alloy for the possible diffusion path, it is required to calculate the activation energy. The nudged elastic band (NEB) method adopted by Henkelman et al. [64, 65] was used to determine the minimum energy path for the saddle point, corresponding to the movement of the atomic oxygen. For the NEB calculation, seven images per each diffusion path were used to calculate the activation energy of oxygen in Ni-Cr binary alloy. The force on image i can be written as:

$$F_i = -\nabla E(R_i)| \perp + F_i^s \cdot \hat{\tau}_i \hat{\tau}_i \tag{3-1}$$

where $-\nabla E(R_i)$ is the gradient of the energy with respect to the atomic coordinates in the system at image i, and F_i^s is the spring force acting on image i.

The perpendicular component of the gradient could be obtained by subtracting out the parallel component

$$-\nabla E(R_i)| \perp = \nabla E(R_i) - \nabla E(R_i) \cdot \hat{\tau}_\| \hat{\tau}_\| \tag{3-2}$$

Before every test step, lattice relaxation task was performed by using a conjugate-gradient (CG) algorithm for insertion energies. In doing so, all ions were allowed to relax, while the supercell volume was kept constant, but could change shape. In order to calculate the effect of chromium on the oxygen diffusivity in nickel, some of chromium atoms replaced nickel atoms as the nearest-neighbor (NN) atoms of oxygen. Subsequently, calculation of the activation energy of oxygen diffusion was performed as a function of increase in the number of NN chromium atoms. Furthermore, to analyze the effect of chromium position on the oxygen diffusion in nickel with the same number of NN chromium atoms, the activation energies of oxygen diffusion were calculated with chromium atoms in two different positions, namely, in front and at the back of oxygen. The total number of chromium atoms in the supercell was set as 4, for all cases of Ni-Cr binary alloy. Figure 3-5 illustrates the

calculation model focusing on the oxygen diffusion as a function of different number of the NN chromium atoms, and the different position of the chromium atoms for each supercell. The open arrows indicate increase in the number of NN chromium atoms in front of oxygen, while the black arrows indicate that increase in the number of NN chromium atoms at the back of oxygen.

3.3. In-situ oxide analysis on the Ni-base alloy/low alloy steel interface using Raman spectroscopy

3.3.1 Introduction

Dissimilar metal welds (DMWs) are commonly used in the structural components of nuclear energy system as transition joints between the components of different alloys. In particular, reactor pressure vessel nozzles and pressurizer nozzles or cold/hot legs on steam generators in nuclear power plants have DMWs, the integrity of which is highly important to make the nuclear reactors safe. Recently, stress corrosion cracking (SCC), which is one of the main degradation processes of structural materials, was observed in Alloy182 weld metal in high-temperature water. This has aroused serious concerns about the SCC behavior in the fusion boundary (FB) region of Alloy182–low alloy steel (LAS) dissimilar weld joint in light water reactors (LWRs) [66]. In general, Alloy182 is a nickel-based alloy filler metal, where the crack propagates along the grain boundary. When the crack reaches the LAS, it stops propagating. Nevertheless, the cracks start growing inside the grain of the LAS. During pitting, the crack is reactivated when the crack growing inside the grain reaches the grain boundary. Such initiation and SCC behavior have been reported in the Alloy182/82 weld metal of DMWs [67, 68] .

In general, because of the welding process, the transition zone has a more complex microstructure and chemical composition compared to those in the base material between the bulk LAS and filler metal. According to several studies related to the DMW characterization [69-72], this transition is found to cause changes in the mechanical property and corrosion resistance. Thus far, several studies have been performed to unravel the mechanism underlying the cracking phenomena in a DMW. Nevertheless, there is a lack of fundamental understanding of the cracking process in DMWs. At present, the importance of analyzing oxidation behavior or oxidation process is in the recognition stage [73, 74].

It believes that limiting analysis to ex situ observation is the main cause of the current inadequate understanding. Because of the experimental constraints in conducting measurements at elevated temperatures and high pressure, most of the techniques used for analyzing the oxidation behavior or corrosion are not suitable for in situ investigation. However, this may not be true in the case of Raman spectroscopy, which can identify corrosion products and oxide films on a metal surface by in situ investigation. Such an in situ analysis is expected to provide a comprehensive understanding of the corrosion mechanism, because the removal of the material from the corrosion environment can modify the oxide film structure and chemistry. So far, several studies have reported the in situ investigation of aqueous corrosion in pure metals or alloys at elevated temperatures in the boiling-

water environment, air-saturated water, and pressurized water environments [22-26]

Recently, A152 has been extensively used as a filler metal in manufacturing DMWs in LWRs because of the fact that A152 has more chromium and higher crack resistance than Alloy182 in the LWR conditions. In addition, there are no reports or experience of SCC in DMWs when A152 is used as the filler metal in the weld between A690 and LAS. However, the operating time is not sufficiently long to ensure that the high Cr alloys are perfectly immune to PWSCC. Moreover, as-welded conditions at the FB may not cause serious cracking issues, while thermal aging may change the formation of local microstructure oxide and decrease the cracking resistance or mechanical properties.

In this study, the oxide behavior of the as-welded/thermally aged nickel-based alloy/LAS dissimilar metal welding has been investigated by an in situ characterization of the oxide film using Raman spectroscopy. The current study focuses on the characterization of the interface region between A152 and A533Gr.B in a proactive approach rather than a reactive one. The in situ surface oxide film analysis using Raman spectroscopy was conducted on the interface region of an as-welded/thermally aged Ni-based alloy/low alloy steel dissimilar metal weld at 300 ℃

3.3.2 Materials

As-welded and thermally aged dissimilar metal weld samples composed of Alloy 690/Alloy 152/A544 Gr.B were analyzed using the in situ Raman spectroscopy. The samples were fabricated at Argonne National Laboratory (ANL), USA; the chemical composition of the samples is summarized in Table 3-1. The welding procedures comply with the recommendations of ASME Section IX [75]. A533Gr.B was buttered with Alloy 152 by shielded metal arc welding, followed by a post welding heat treatment at 607–635 ℃ for 3 hr. After this process, the weld joint of Alloy 690 and A533Gr.B was prepared by the shielded metal arc welding method with Alloy 152 fillers. Thermal aging was conducted to simulate the typical 30-years lifespan in the energy system operating at 320 ℃. The thermal aging heat treatment, which was calculated by chromium activation energy which is 125 kJ /mol for diffusion in SS304, was performed at 450 ℃ for 2750 h [76].

3.3.3 Hydrothermal optical cell and test loop

The cell for the in situ observation at high temperature and pressure condition was developed for this study. The 3/4 inch union cross of compression fitting made of alloy 600 is used as a main optical cell, which is connected to a 3/4 inch union tee for simulated PWR primary water circulation. The 3/4 inch union tee plays a role of water inlet and outlet with coaxial configuration with 1/4 inch

inner tubing. Through the left arm of union cross, the sample holder will be inserted, and the immersion optics will be inserted through the right arm of the union cross, as shown in figure 3-6. The union cross is fully covered by a main heater and thermal insulation as described in the previous section, thus its temperature should be maintained around 350℃. As shown in figure 3-7, sample holder is made of Zr-rod with surface oxidation and the cap is made of Alloy 718 because the sample should be inserted in the 3/4 inch union cross and electrical insulation around the sample is very important.

To achieve the temperature condition of the maximum 400℃, the flowing-in water is designed to get heating power through the coaxial heat exchanger, and then be heated up primarily using the pre-heater made of a cable-type, and finally by the main heater covering the union cross which is a main hydro thermal optical cell for the experiment.

The test loop, as shown in figure 3-8, has been designed and assembled in order to simulate the PWR primary water conditions for the oxidation of weld samples and the analysis of oxide film grown in this facility. The test loop is cable of heating up to a temperature of 400℃ by the preheater and main heater and will be normally operated in the same environment as a PWR primary water conditions including 350 ℃ and 15 MPa. Also, the water chemistry condition will be maintained in such that the dissolved hydrogen (DH) content is ~ 30 ppm, the dissolved oxygen (DO) content is less than 10ppb and pH is between 6.9 and 7.4 using 1,000 ppm of H_3BO_4 and 2 ppm of LiOH.

3.3.4 Raman spectroscopy system

The Raman spectroscopy system (manufactured by Kaiser Optical Systems, INC) adopted in this work consisted of an excitation laser source, a spectrometer, and optical components, including mirrors and filters. A krypton ion laser with 532 nm wavelength was used for excitation of the in situ spectra. The power density at the specimen was less than 10 mW/cm^2 and the beam size of the laser was 100 μm. The Raman system was equipped with holographic laser band pass-filter, which consisted of volume transmission grating to remove the unwanted signal. The volume transmission grating had dispersions at 5000 grooves/mm with a spectral resolution of 5 cm^{-1}. The charge-coupled device (CCD) detector had an analog-to-digital converter providing 16 bits of precision yielding a maximum of 65545 counts; the aspect ratio was 2/3 (height/width). The immersion collection fiber optics with a sapphire window at the tip was adopted to collect the Raman signal from the samples. The fiber optic system provided the images of the laser excitation light from a 62.5-μm optical fiber

onto the sample and incorporated the images of the sample emission onto a 100-µm optical fiber. Figure 3-9 shows the schematic diagram of the Raman system used in this study.

3.3.5 Experimental procedure

For the confidence of the Raman spectroscopic system, measurements were conducted to obtain reference Raman spectra on oxides using powder samples such as nickel and chromium oxides and spinels. Then an in situ Raman spectroscopy was performed on as-welded/thermally aged dissimilar metal weld interfaces in a primary water environment that includes dissolved hydrogen (DH) of ~30 ppm, dissolved oxygen (DO) of less than 10 ppb, and pH between 6.9 and 7.4, using 1,200 ppm of H_3BO_4 and 2 ppm of LiOH. The test was performed at 300 ℃ for 50 h.

After the in situ Raman analysis, the specimens were characterized ex situ using scanning electron microscopy (SEM), transmission electron microscopy (TEM), energy dispersive x-ray spectrometry (EDS), and Raman spectroscopy. The in situ and ex situ results were compared to provide a comprehensive understanding of the observed results.

TABLE 3-1. Chemical composition of dissimilar metal weld used in this study

Element	Composition (wt%)		
	A690	A152	LAS(A533Gr.B)
C	0.03	0.04	0.22
Al		0.24	
Si	0.07	0.46	0.19
P		<0.003	0.01
S	<0.001	<0.001	0.012
Cr	29.5	29.04	0.18
Mn	0.2	3.56	1.28
Fe	9.9	9.36	Bal.
Co		<0.01	
Ni	59.5	55.25	0.51
Cu	0.01	<0.01	
Nb+Ta		1.84	
Mo		0.01	0.48
Ti		0.15	
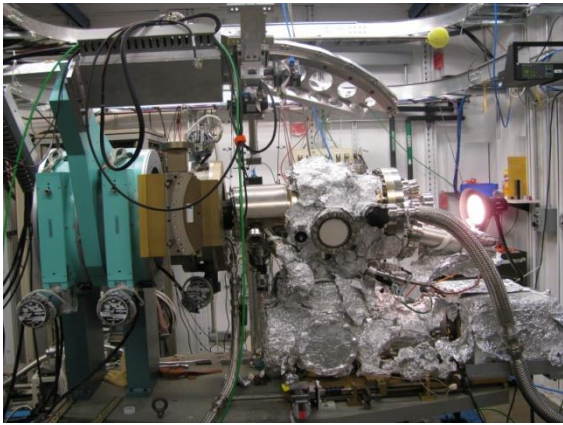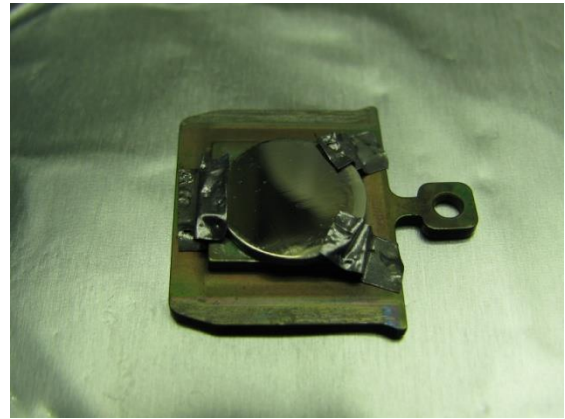
(a)   (b)

Figure 3-1. (a) Overall view of the ultra high vacuum chamber at 33ID-E beamline of APS and (b) Ni(110) sample mounted on a sample holder.
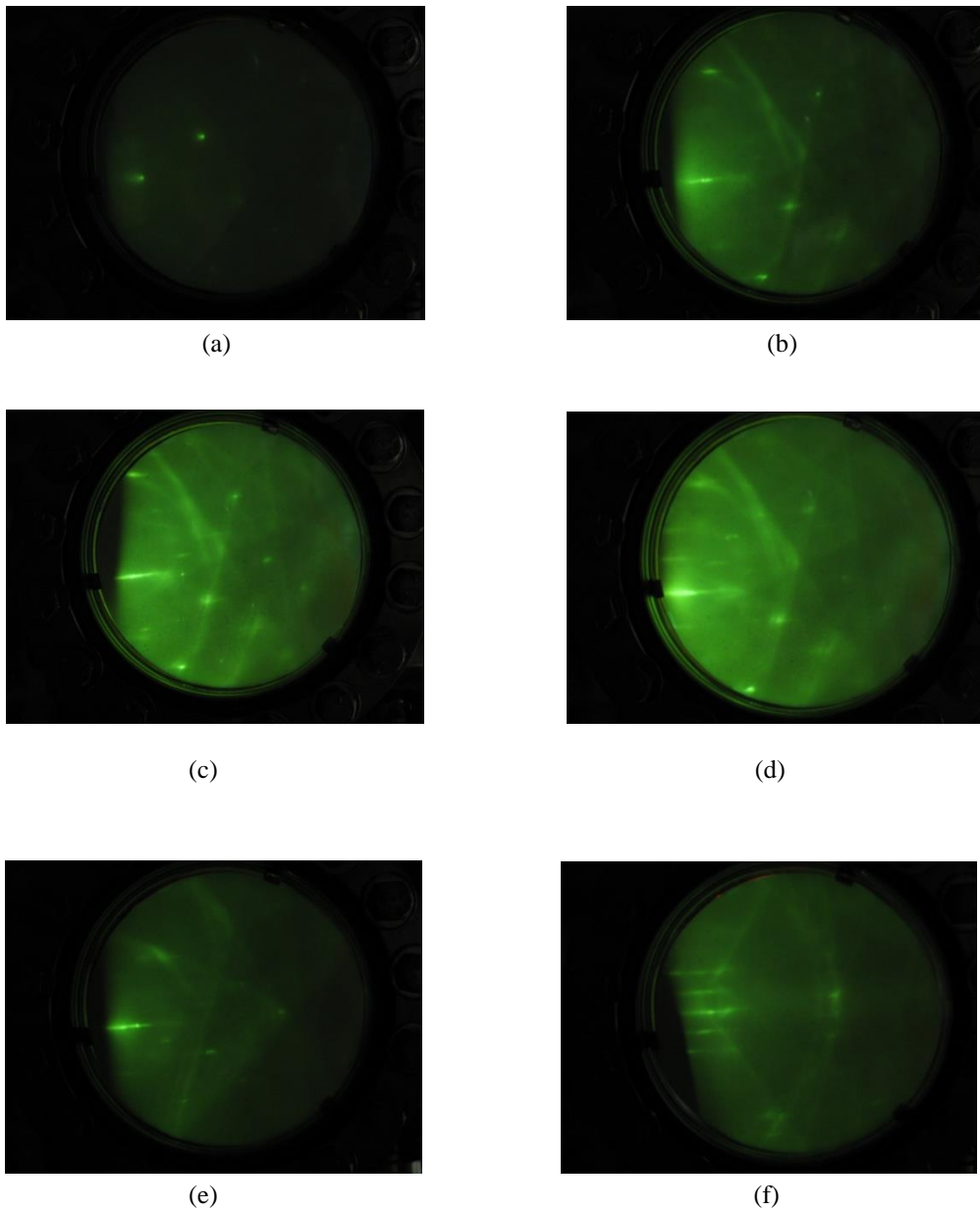
Figure 3-2. RHEED images (a) after electropolishing, after (b) 1st, (c) 2nd, (d) 3rd, and (e) 4th sputtering/annealing cycles; (f) image after 4th cycle with a different angle from (e).
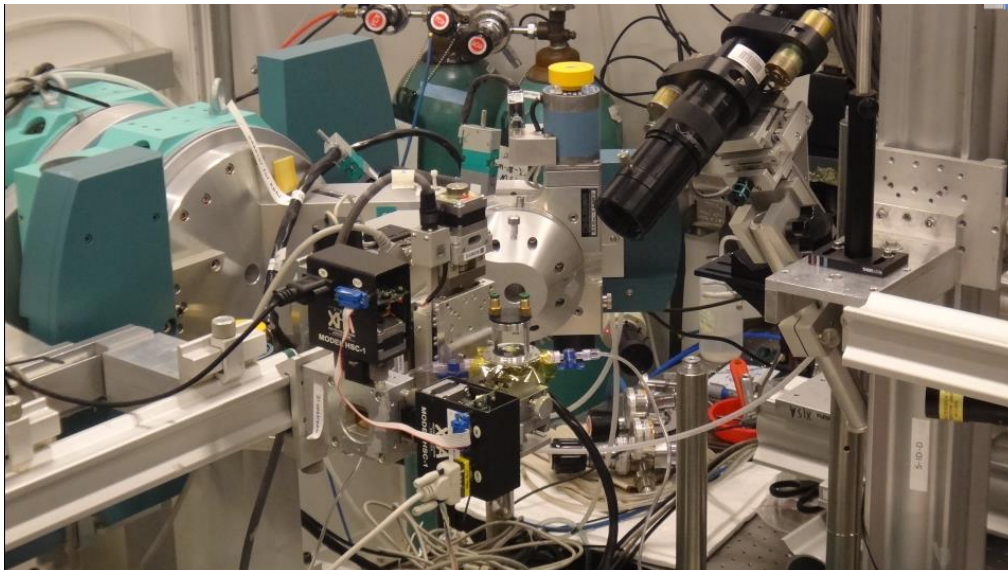
Figure 3-3. The CTR measurement of the Ni(110)/NiO-water interface
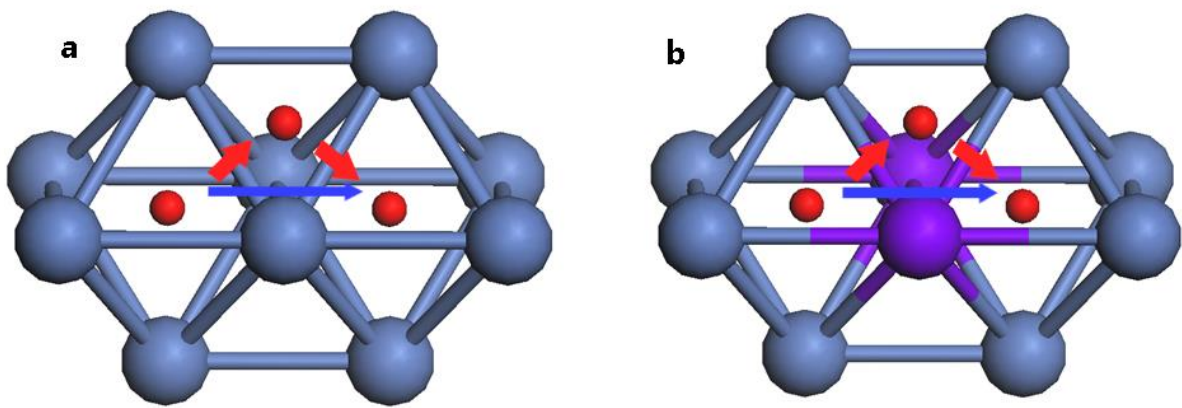
Figure 3-4. Atomic configurations of diffusion pathway of oxygen atom in metal matrices. O atoms are coloured red, Ni atoms are coloured blue, and Cr atoms are coloured violet. Oxygen is assumed to move along either O-T-O represented as red-coloured arrows or O-O path represented as blue-coloured arrows in pure (a) Ni and (b) Ni-Cr binary alloy**.**
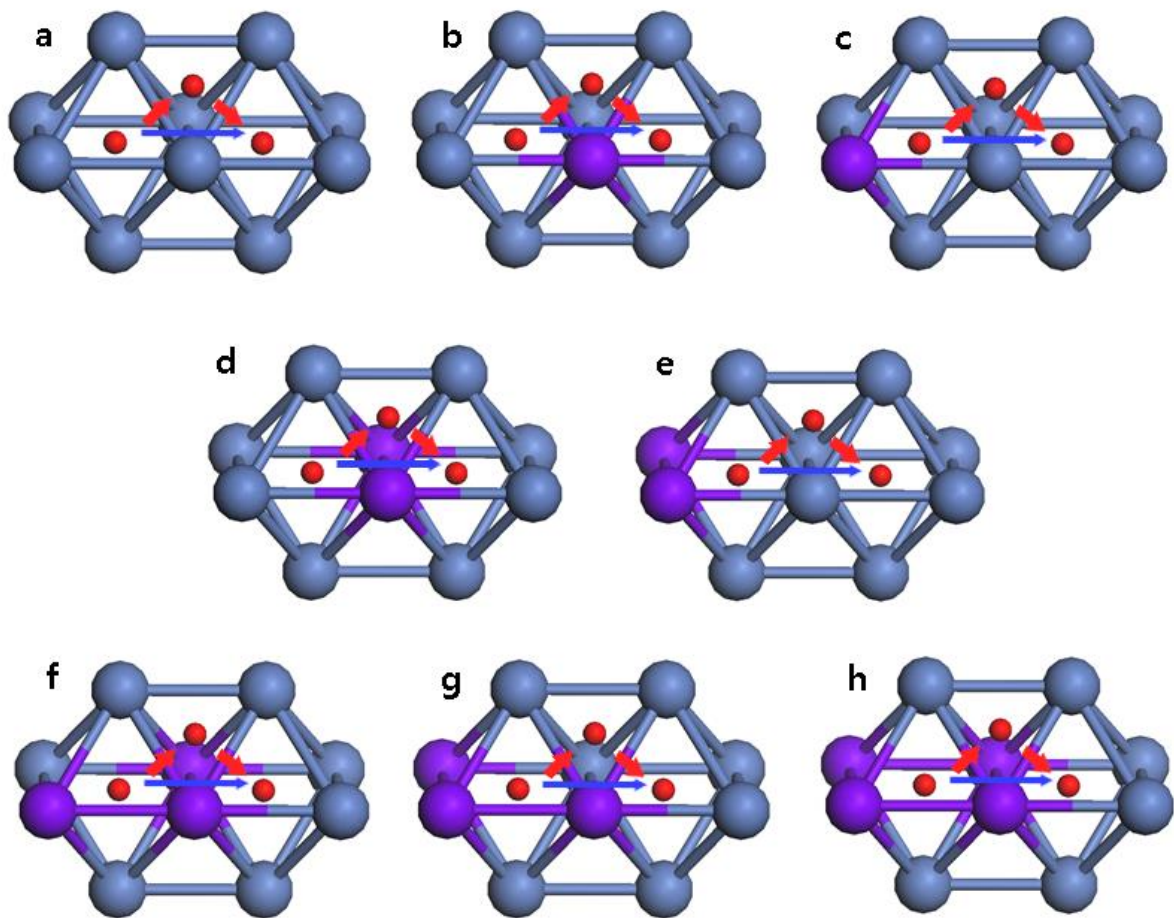
Figure 3-5. Variable models used in the calculation of Ni-Cr binary alloy system which are focused on oxygen diffusion pathways. (a) pure nickel model for reference, for one nearest-neighbor(NN) Cr atom, (b) the Cr atom exist in front of oxygen (1NN Cr (A)) and (c) at the back of oxygen (1NN Cr (B)), for two NN Cr atoms, (d) the Cr atoms exist in front of oxygen (2NN Cr(A)) and (e) at the back of oxygen (2NN Cr (B)), for three NN Cr atoms,(f) two Cr atoms exist in front of oxygen and the other exist at the back of oxygen (3NN Cr_1) and two Cr atoms (g) exist at the back of oxygen and the other exist in front of oxygen (3NN Cr_2) , and (h) four NN Cr atoms.
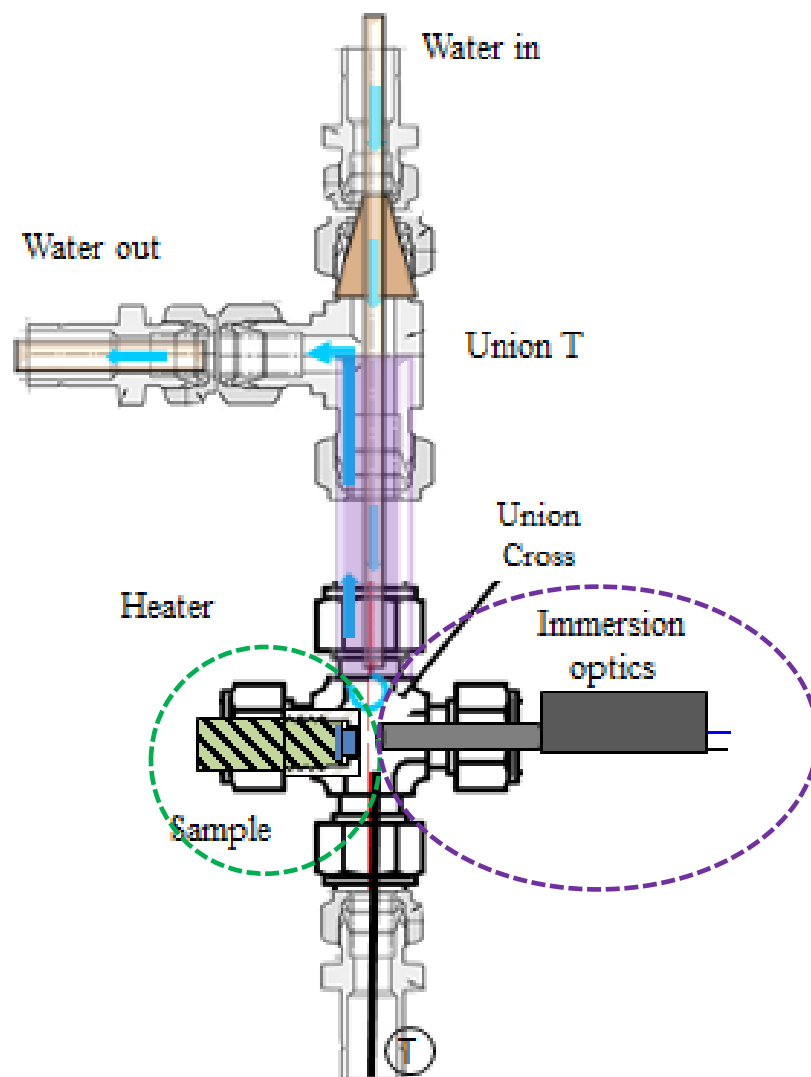
Figure 3-6. The design of hydrothermal optical cell

Figure 3-7. Sample holder
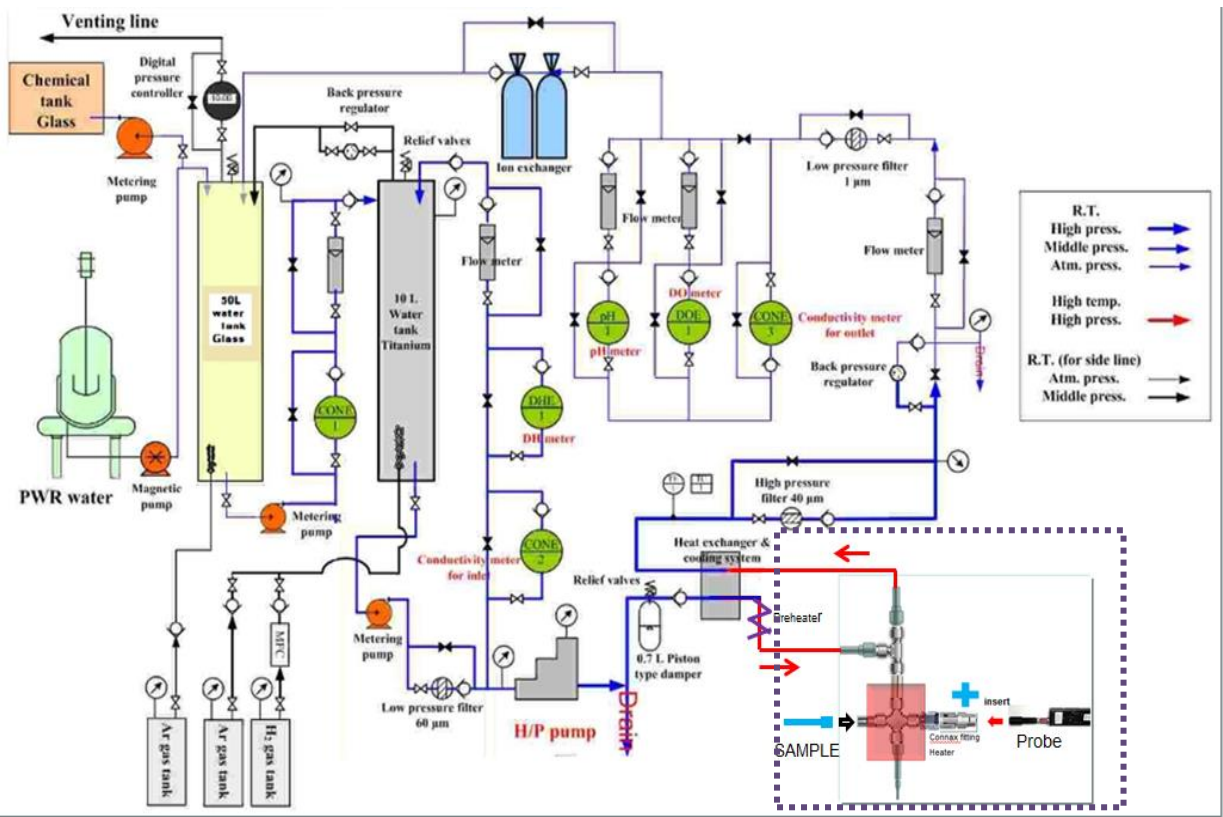
Figure 3-8. Schematic diagram of test loop
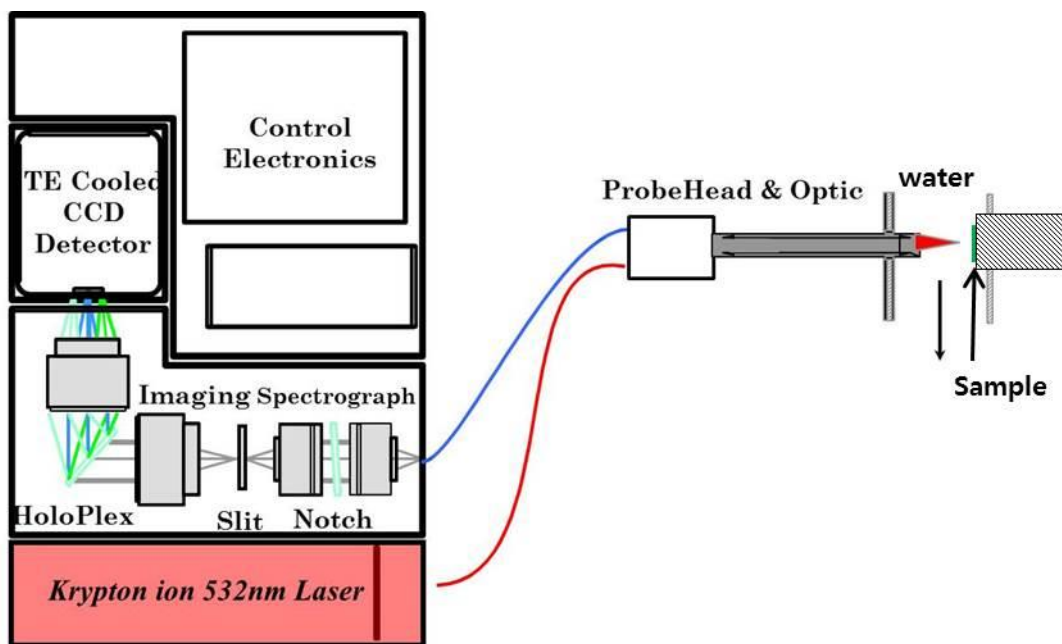
Figure 3-9. Schematic diagram of Raman system used for in situ analysis in this study

IV. Results

4.1. High resolution X-ray reflectivity

4.1.1 Ni(110)/NiO-helium

The X-ray peaks were detected by 2D Pilatus detector and the results of the peak represented by image files as the Q value. In order to get the CTR peaks the peaks at the image files should be integrated. The integration of the peaks was performed using IGOR6.3.4 software which were developed by WaveMetrix.Inc. Figure 4-1 shows the peak integration using the IGOR. The images from detector were selected automatically by IGOR and the regions for back ground and peak were decided manually. Figure 4-2 shows the integrated CTR data of Ni(110)/NiO-helium structure. CTR data is measurable with low errors even at lower intensity region. This CTR data also confirms that the surface pre-treatment procedure developed for Ni(110) was suitable for the surface X-ray study.

4.1.2. Ni(110)/NiO-water

After Ni(110)/NiO-helium measurement, The pure water was injected on the surface. Figure 4-3 shows the (a) schematics of thin film cell and (b) shows the picture of thin film cell used in this study. Figure 4-4 shows the CTR data of Ni(110)/NiO-water interface. There are changes in curvature features in middle range of Q and several data were disappeared. It can be considered that there is miss-cut issue or the sample is slightly moved when the water was injected.

4.2. Activation energy of oxygen diffusion in Ni-Cr alloy

Figure 4-5 shows the energy required for oxygen transport, as calculated by NEB method, based on the different number of NN chromium atoms and their relative positions in Ni-Cr binary alloy along the two diffusion paths. The highest energy barrier indicates the activation energy of oxygen diffusion in each path.

4.2.1. Increase of NN chromium in front of oxygen

In case of increment of NN chromium atoms in front of oxygen, chromium atoms replaced the NN nickel atoms existing in front of the oxygen atoms, with the increase in the number of NN chromium atoms. On comparing the diffusion in pure nickel with those of 1NN chromium (A) and 2NN chromium (A), the activation energies were found to decrease from 1.44 eV to 0.76 eV along the O-O path and from 1.12 eV to 0.49 eV along the O-T-O path. Furthermore, with the 2NN chromium atoms existing at the back of the oxygen, the activation energies were found to decrease. When the NN nickel existed in front of oxygen were replaced by chromium (Table 4-1), the activation energies along the O-O and O-T-O path were calculated to be 1.89 eV and 1.45 eV, respectively, in case of 3NN Cr_2 and 1.83 eV and 1.34 eV, respectively, in case of 4NN Cr. On analyzing the results from 2NN Cr (B), 3NN Cr_2, and 4NN Cr cases it could be observed that, as the NN nickel atoms existed in front of oxygen atoms, the activation energies decreased from 1.98 eV to 1.83 eV along the O-O diffusion path and from 1.57 eV to 1.34 eV along the O-T-O diffusion

4.2.2. Increase of NN chromium at the back of oxygen

In case of increment of NN chromium atoms at the back of oxygen, the chromium atoms replaced the NN nickel atoms existing at the back of the oxygen, with the increase in the number of NN chromium atoms (Table 4-2). On comparing with pure nickel, 1 NN Cr (B) and 2 NN Cr (B), it could be observed that the activation energies increased from 1.44 eV to 1.98 eV along the O-O diffusion path and from 1.12 eV to 1.57 eV along the O-T-O diffusion pathway. Moreover, in case of 2

NN chromium atoms already existing in front of oxygen, the activation energies were found to increase. As the chromium atoms replaced the NN nickel atoms existing at the back of the oxygen, the calculated activation energies increased from 0.76 eV to 1.83 eV along the O-O diffusion path and from 0.49 eV to 1.34 eV along the O-T-O diffusion path. Since the replaced 3rd and 4th NN chromium atoms exist in the direction opposite to that of the oxygen diffusion, the diffusing oxygen atoms would be far from 3rd and 4th chromium atoms. However, the chromium has very strong oxygen affinity, thereby requiring higher energy for the oxygen to diffuse along the pathways. Finally, the activation energy for oxygen diffusion with 4NN chromium atoms is found to be higher than that of pure nickel.

4.3. Oxide analysis using in-situ Raman spectroscopy

4.3.1. Reference Raman spectra for oxide powders

Figure 4-6 shows the measured Raman spectra obtained a black-colored NiO powder sample in comparison with Maslar et al.'s [25], Kim and Hwang's work [26]. The reference Raman spectrum for NiO powder in this study measured at ca. 490 cm^{-1}. This result is well matched with most intense green NiO spectrum of previous references. Figure 4-7 shows the measured Raman spectrum for Cr$_2$O$_3$ powder with 532nm radiation in comparison with Maslar et al.'s [22], Kim and Hwang's work [26]. The spectrum of Cr$_2$O$_3$ power in this study exhibits the peaks at 608, 550, 340 and 300cm^{-1}. The most intense peak obtained at 550 cm^{-1}, and these results are well matched with these of reference literatures. Figure 4-8 shows the measured Raman spectra for the NiFe$_2$O$_4$ powder in comparison with the reference spectra reported in literature [23]. The most intense peaks were observed at ca. 704cm^{-1} in this experiment. The measured Raman spectrum for NiFe$_2$O$_4$ powder agrees well with reference spectra reported in literature.   Finally, Figure 4-9 shows the measured Raman spectra for the NiCr$_2$O$_4$ powder.   The Raman peak wavenumbers of the reference powder spectra care compared with those reported for NiCr$_2$O$_4$ powder. The reference spectrum measured in this study exhibited significant features at ca. 429, 509, 551, and 680 cm^{-1}. Raman features of the reference powder spectra for these oxides show good agreements between the measurement in this study and literature data.

4.3.2. In-situ Raman spectroscopy for as-welded dissimilar metal weld

Figure 4-10 shows the in situ Raman spectra of the as-welded dissimilar metal weld interface in the simulated primary water environment at 300 ℃ for 50 h. The baseline correction of the Raman spectra was performed without any smoothing process. The Raman peaks at ca. 417 cm^{-1} observed in all the samples and a broad peak with low intensity observed at around 735–747 cm^{-1} could be attributed to the sapphire window of the immersion optics [26]. The high intense Raman peak for

boric acid was observed at 868 cm^{-1}. Additionally, the peak at 550 cm-1 could be attributed to Cr_2O_3 and that at 665 cm^{-1} represents Fe_3O_4. These peaks were continuously observed until 50 h, exhibiting high intensity. The peak of the iron-chromium spinel was observed as a low intensity peak at 684 cm-1. After the completion of 15 h from the beginning of measurement, the peak intensity of the iron-chromium spinel increases and continues to increase with measurement time. Several peaks can be considered to have originated from spinels such as nickel-chromium or nickel-ferrite. However, the signals of these peaks are weak and observed in the background of noise. Even the most intense peaks of nickel-chromium or nickel-ferrite spinel could not be observed at 512 cm^{-1} and 700 cm^{-1}, respectively.

4.3.3. In-situ Raman spectroscopy for thermally aged dissimilar metal weld

Figure 4-11 shows the in situ Raman spectra of the thermally aged dissimilar metal weld interface in the simulated primary water environment at 300 ℃ for 50 h. Similar to the as-welded DMW, the Raman peaks corresponding to the sapphire window could be observed at 417 and 735–737 cm^{-1}, and the peak at 868 cm^{-1} could be attributed to boric acid in the water. The peaks attributed to iron-chromium spinel were observed at 548, 636, and 684cm^{-1} with very low intensity close to noise. The peaks were continuously observed even increase the exposure time at same positions. Therefore, it can be consider as peaks of iron chromium spinel not noise. The peaks corresponding to the nickel-iron spinel was observed at 485 cm^{-1} (strong peak) and 700 cm^{-1}. In addition, the Raman peak at 512 cm^{-1} was attributed to the nickel-chromium spinel. As the time was increased from 1 to 50 h, the peak intensity of nickel-chromium observed at 512 cm^{-1} tended to decrease, while the peak intensity of the nickel-iron spinel at 700 cm^{-1} was increased.

4.3.4. Ex-situ characteristic

To compare the in situ measured results, an ex situ observation was conducted using SEM, TEM, EDS for as-welded and thermally aged DMW.

Figure 4-12 shows the SEM images and EDS profile results for the cross-section of the oxides on the as-welded DMW interface. The SEM analysis indicates that the thickness of the oxide layer on the A152 surface is approximately 0.6 μm or less. However, an approximately 1-μm-thick oxide layer was observed on the low alloy steel surface. The elemental analysis of the oxide on the A152 surface, as determined from the EDS profile, indicates that the alloy mainly composed of Ni and Cr, while the LAS mainly composed of Fe. In the case of thermally aged DMW, the thickness of the oxide layer on the A152 surface is found to be approximately 0.6 μm and that of low alloy steel is approximately 1.5–1.8 μm. The oxide layers of the thermally aged DMW are thicker than those of the as-welded DMW. The oxide mainly composed of Ni, Cr, and Fe on the surfaces of A152 and A533Gr.B (Figure 4-13).

Figure 4-14 shows the TEM images and EDS mapping results for the oxides on the as-wleded DMW interfaces. A very thin oxide layer was observed on the A152 surface, while particle type oxides observed on the A533Gr.B. The EDS results show that the components for those oxide layers are Ni and Cr for A152 and Fe for A533Gr.B, In the case of thermally aged DMW, particle type oxide layer observed not only A533Gr.B but A152 surfaces. Furthermore, the EDS results show that the oxides were composed of Ni and Fe as shown in figure 4-15.

Based on these results, it can be considered that Ni and Cr in A152 diffuse to A533Gr.B, while Fe in A533Gr.B diffuses to A152. The measured region for the EDS is only 20–30 μm away from the interface line. Therefore, the in situ measured regions include the regions where ex situ EDS measurements were conducted.

TABLE 4-1. Summary of the calculated results as increasing of NN Cr atoms in front of oxygen.

Pure Ni [56]		1NN Cr (A)[56]		2NN Cr (A)		2NN Cr (B)		3NN Cr_2		4NN Cr	
O O	OTO	O O	OTO	O O	OTO	O O	OTO	O O	OTO	O O	OTO
1.44	1.12	0.93	0.71	0.76	0.49	1.98	1.57	1.89	1.45	1.83	1.34

＊ n NN Cr: The number of nearest-neighbor (NN) chromium atoms for oxygen

＊ A, B : the NN chromium atoms existing in front of oxygen and at the back of oxygen, respectively.

＊ 3NN Cr_2: Two NN chromium atoms existing at the back of oxygen and the one exiting in front of oxygen

TABLE 4-2. Summary of the calculated results as increasing of NN Cr atoms at the back of oxygen.

Pure Ni [56]		1NN Cr (B)		2NN Cr (B)		2NN Cr (A)		3NN Cr_1		4NN Cr	
O O	OTO	O O	OTO	O O	OTO	O O	OTO	O O	OTO	O O	OTO
1.44	1.12	1.61	1.23	1.98	1.57	0.76	0.49	1.25	0.80	1.83	1.34

＊ n NN Cr: The number of nearest-neighbor (NN) chromium atoms for oxygen

＊ A, B : the NN chromium atoms existing in front of oxygen and at the back of oxygen, respectively.

＊ 3NN Cr_1: Two NN chromium atoms, one existing in front of oxygen and the other exiting at the back of oxygen
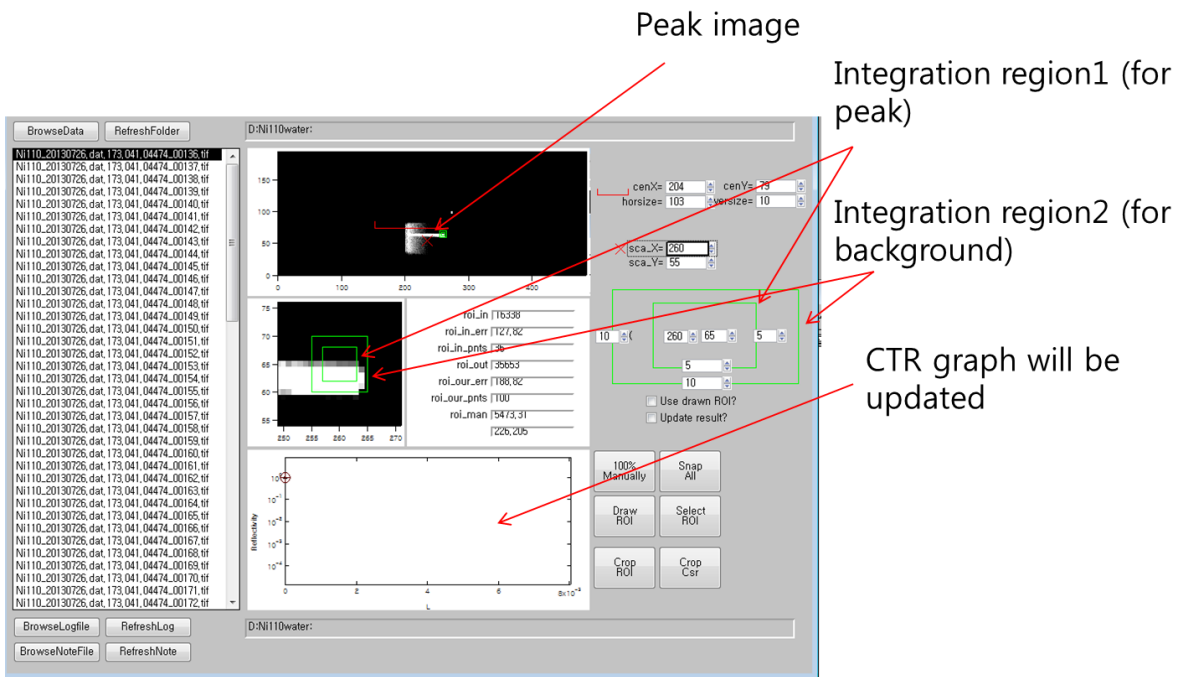
Figure 4-1 Peak integration using IGOR
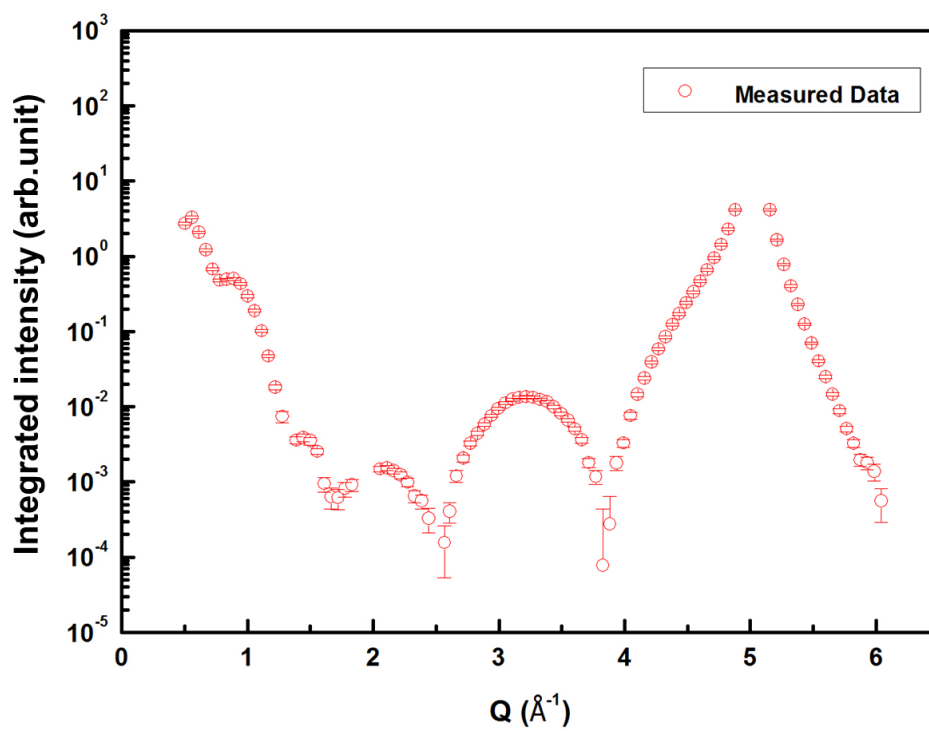
Figure 4-2 Integrated CTR data for Ni(110)/NiO-helium structure
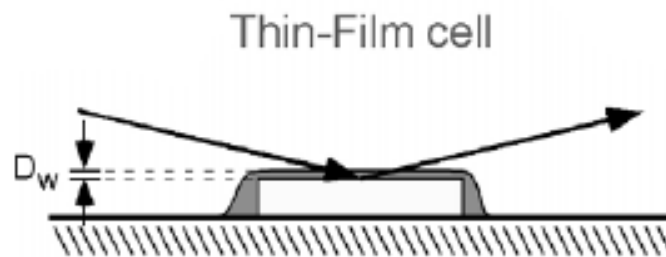
(a)
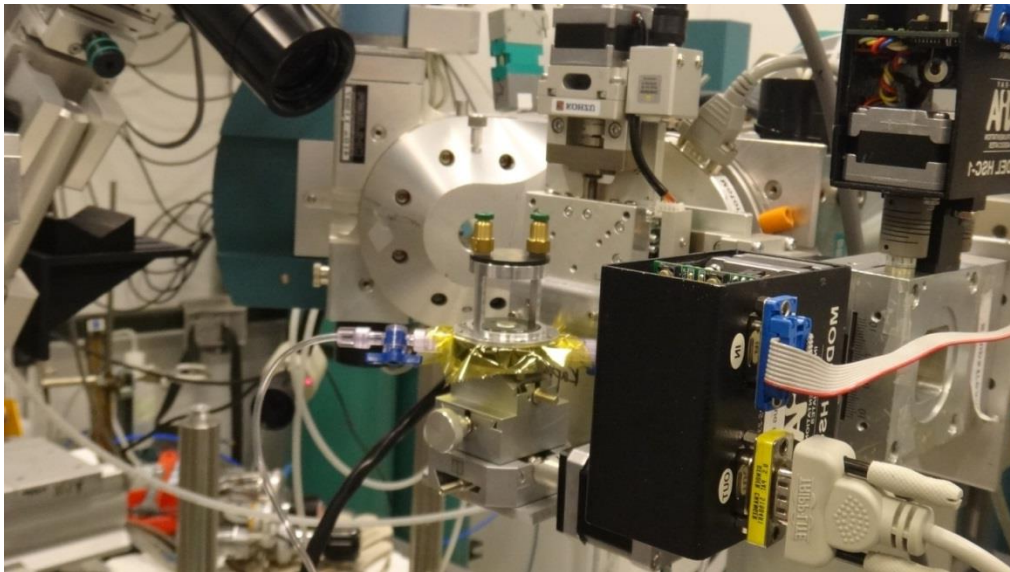
(b)

Figure 4-3. The schematic diagram of (a)thin film cell and (b) real picture of thin film cell on the APS facility used in this study.
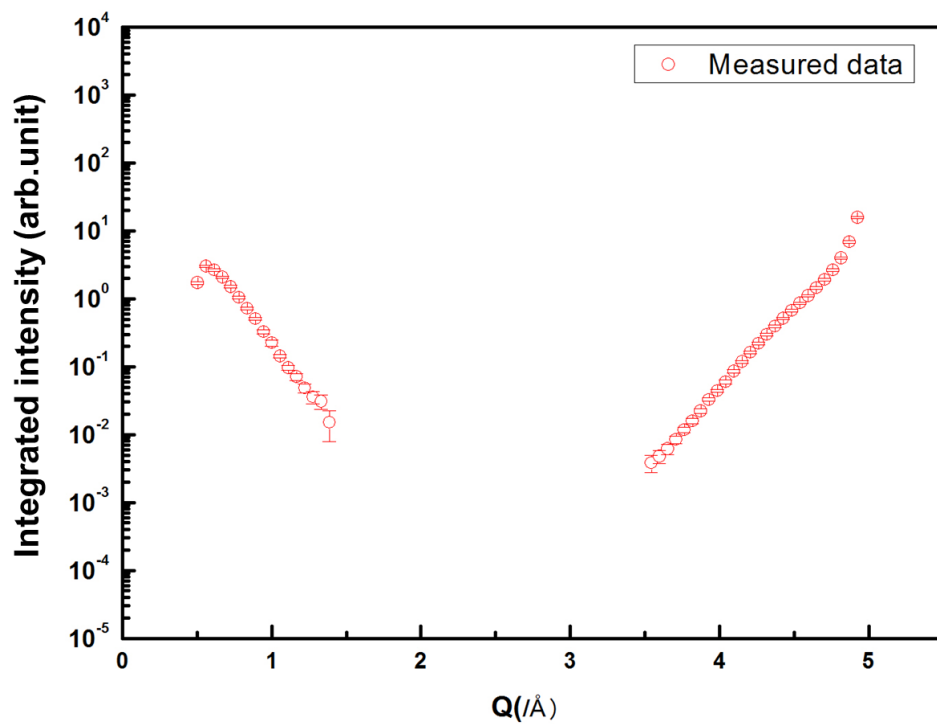
Figure 4-4 Integrated CTR data for Ni(110)/NiO-water structure

c

d

e

f
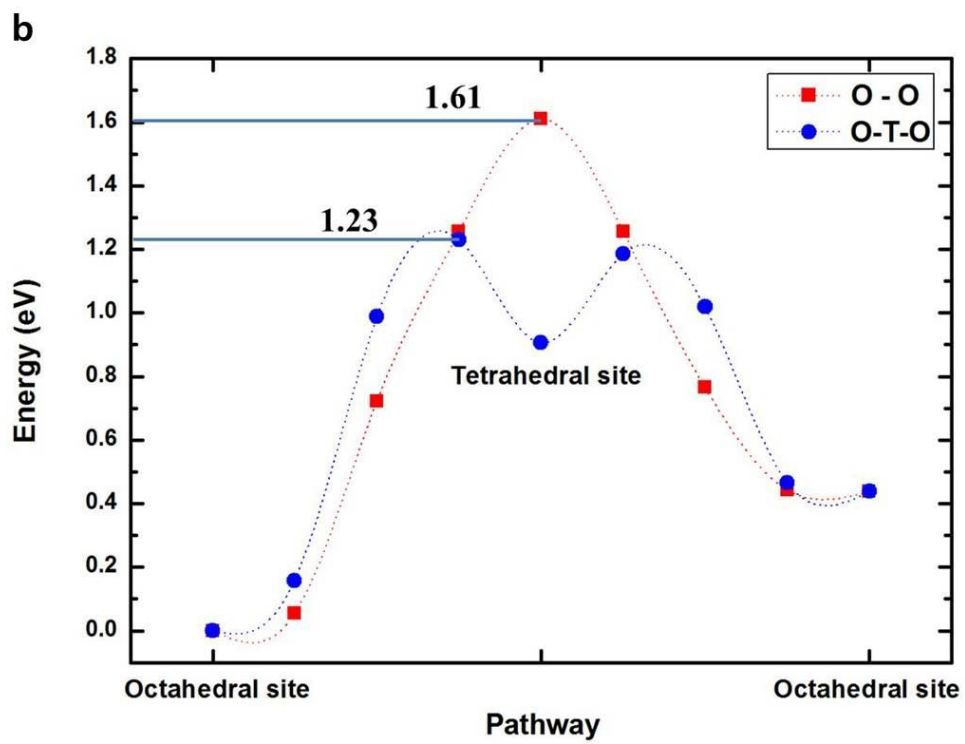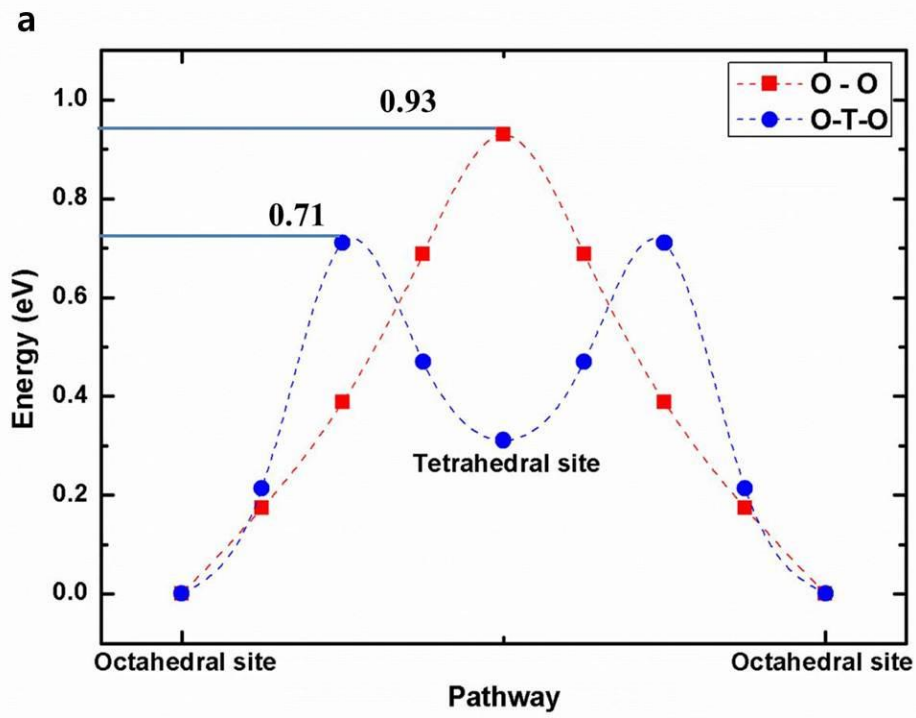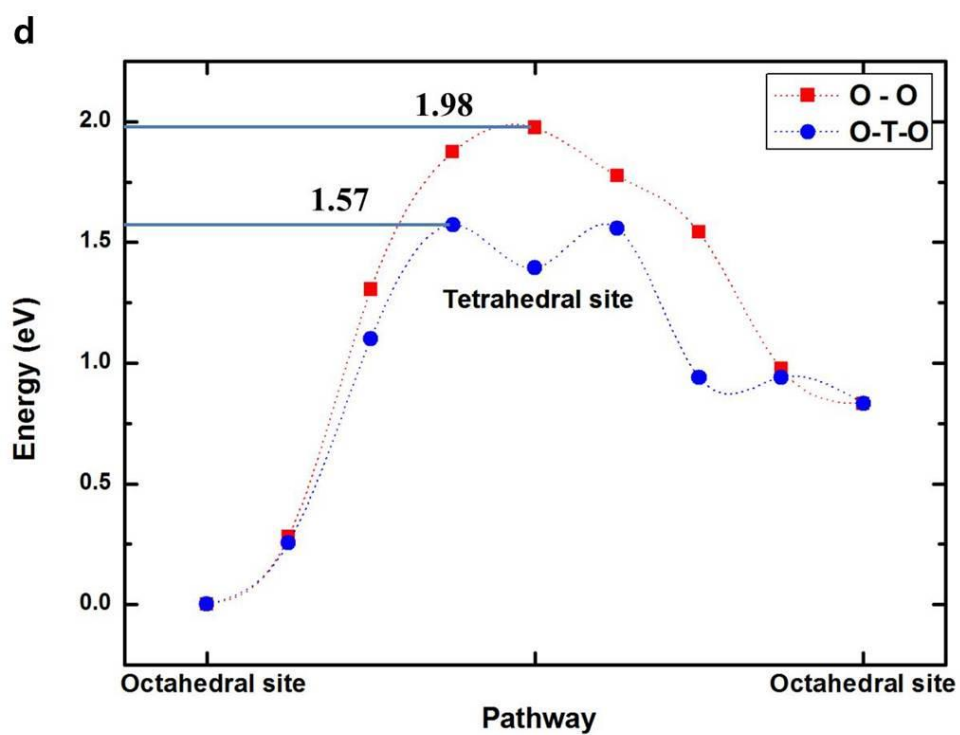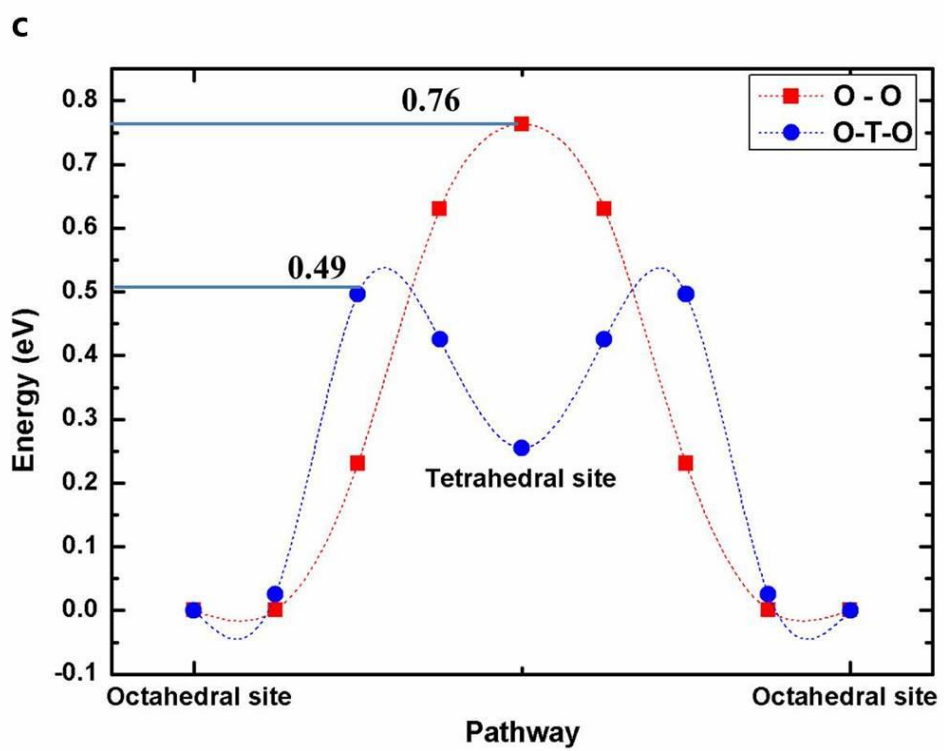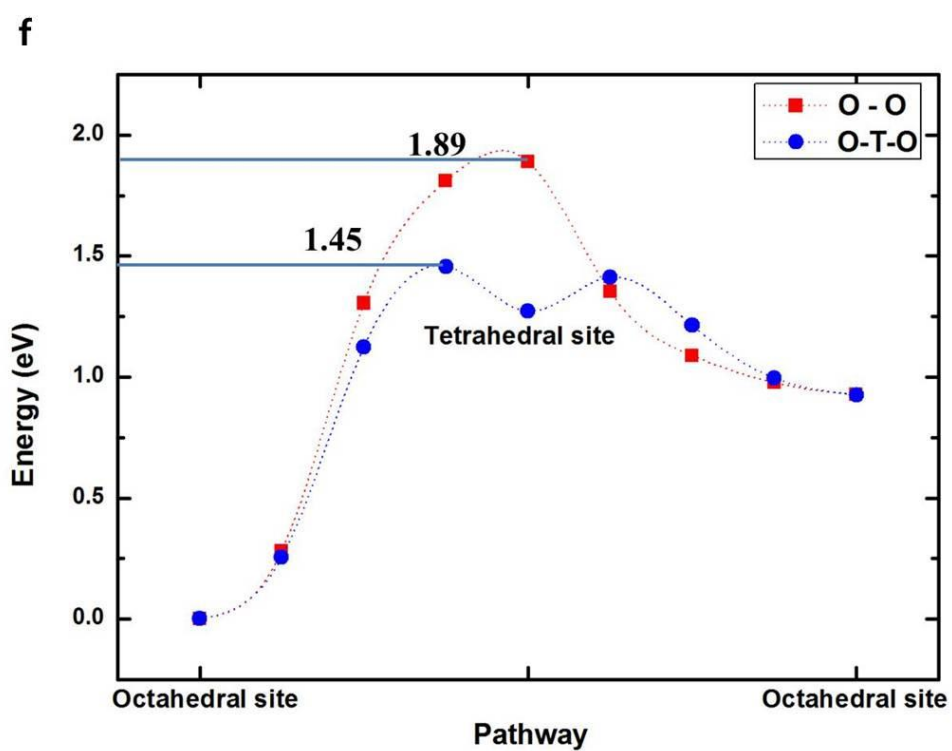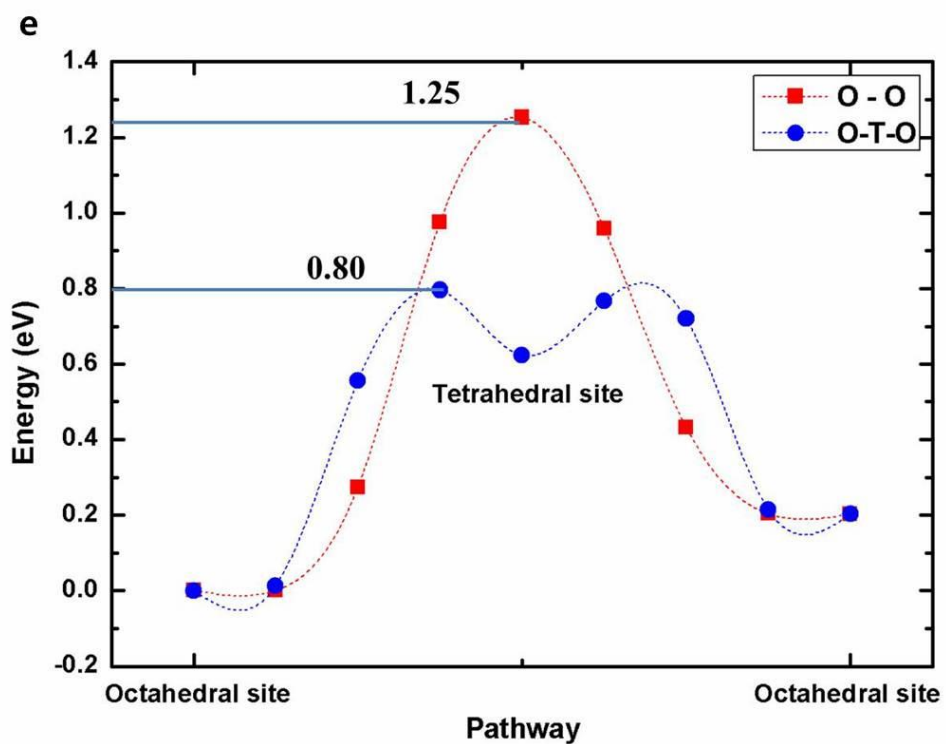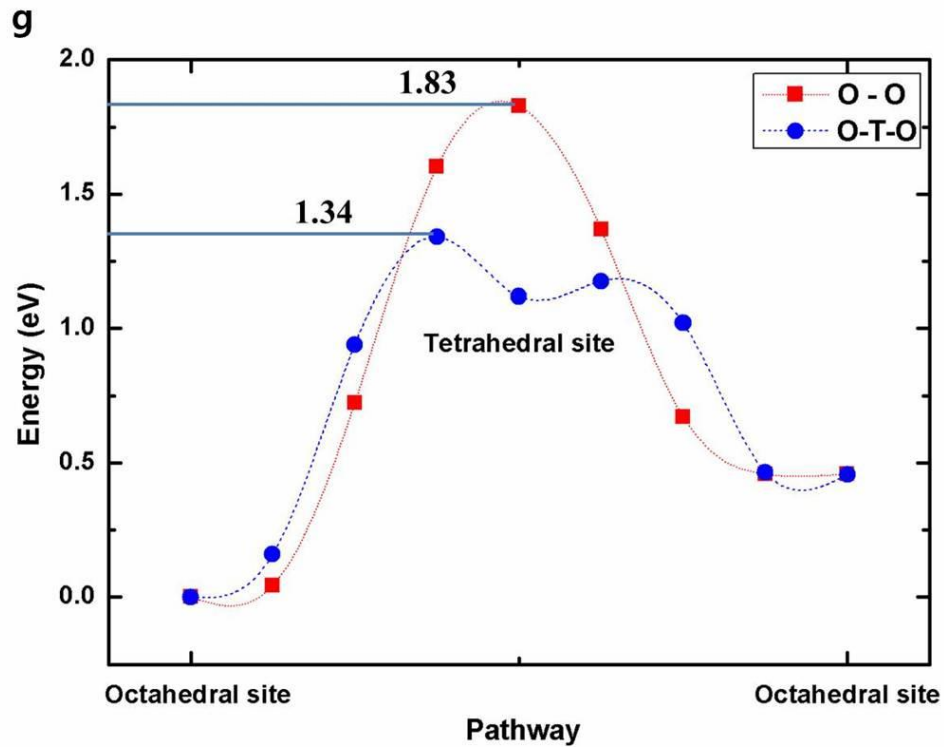
Figure 4-5. Energy of oxygen transport calculated by NEB method for the Ni-Cr binary alloy system, for one nearest-neighbor(NN) Cr atom, (a) the Cr atom exist in front of oxygen (1NN Cr (A)) [56] and (b) at the back of oxygen (1NN Cr (B)), for two NN Cr atoms, (c) the Cr atoms exist in front of oxygen (2NN Cr(A)) and (d) at the back of oxygen (2NN Cr (B)), for three NN Cr atoms, (e) two Cr atoms exist in front of oxygen and the other exist at the back of oxygen (3NN Cr_1) and (f) two Cr atoms exist at the back of oxygen and the other exist in front of oxygen (3NN Cr_2) and (g) four NN Cr atoms.
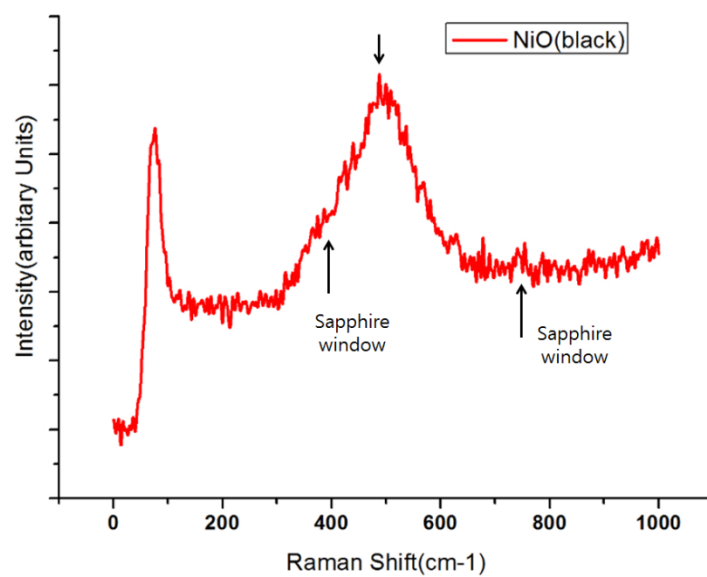
Figure 4-6. Measured Raman spectra for the NiO powder exited with 532nm laser
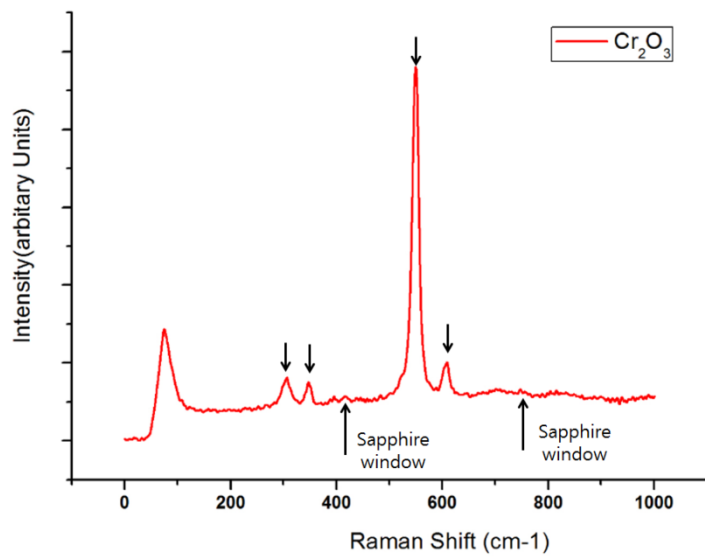
Figure 4-7. Measured Raman spectra for the Cr_2O_3 powder exited with 532nm laser
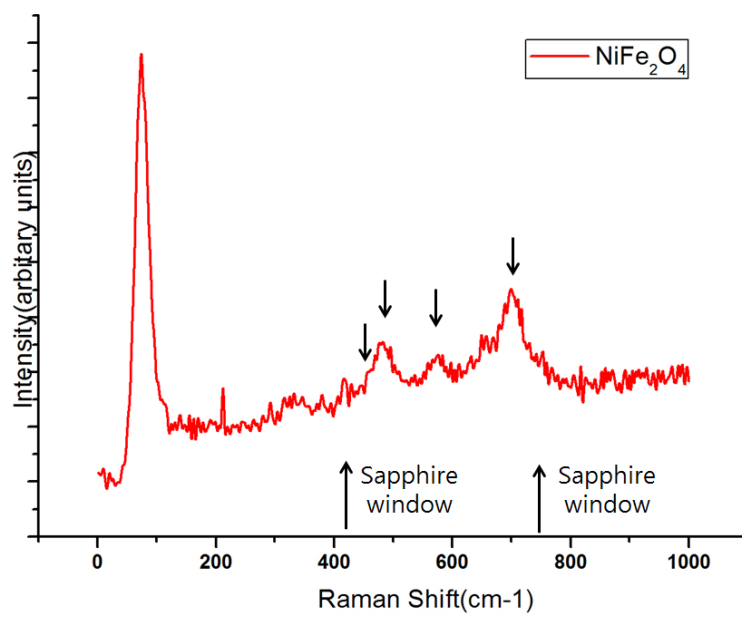
Figure 4-8. Measured Raman spectra for the NiFe$_2$O$_4$ powder exited with 532nm laser
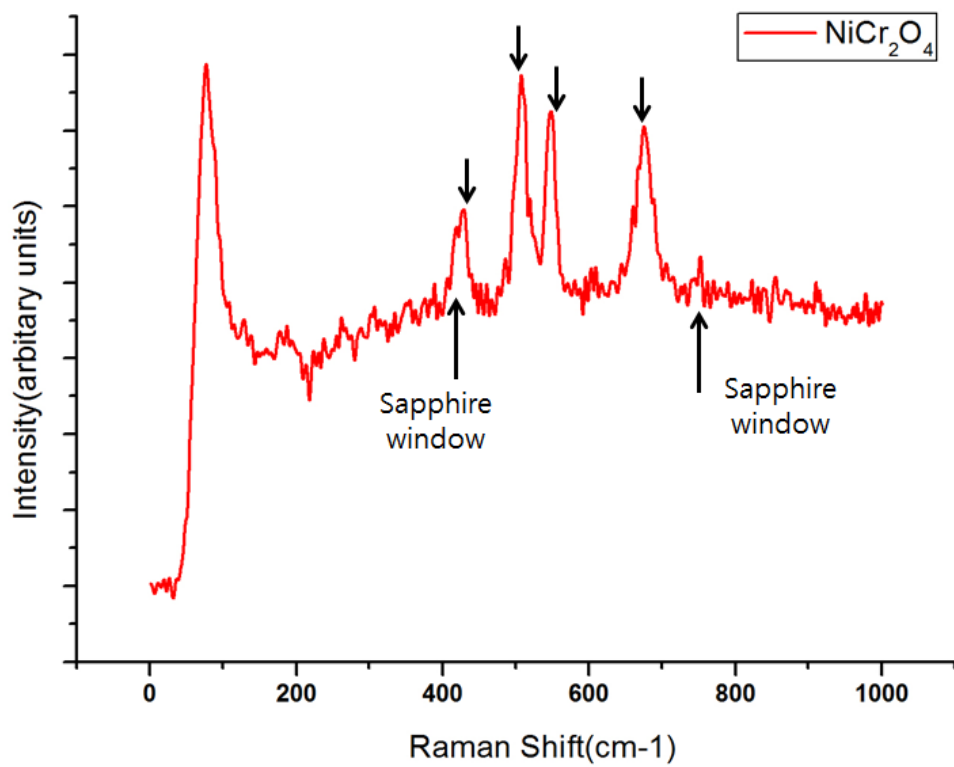
Figure 4-9. Measured Raman spectra for the NiCr$_2$O$_4$ powder exited with 532nm laser
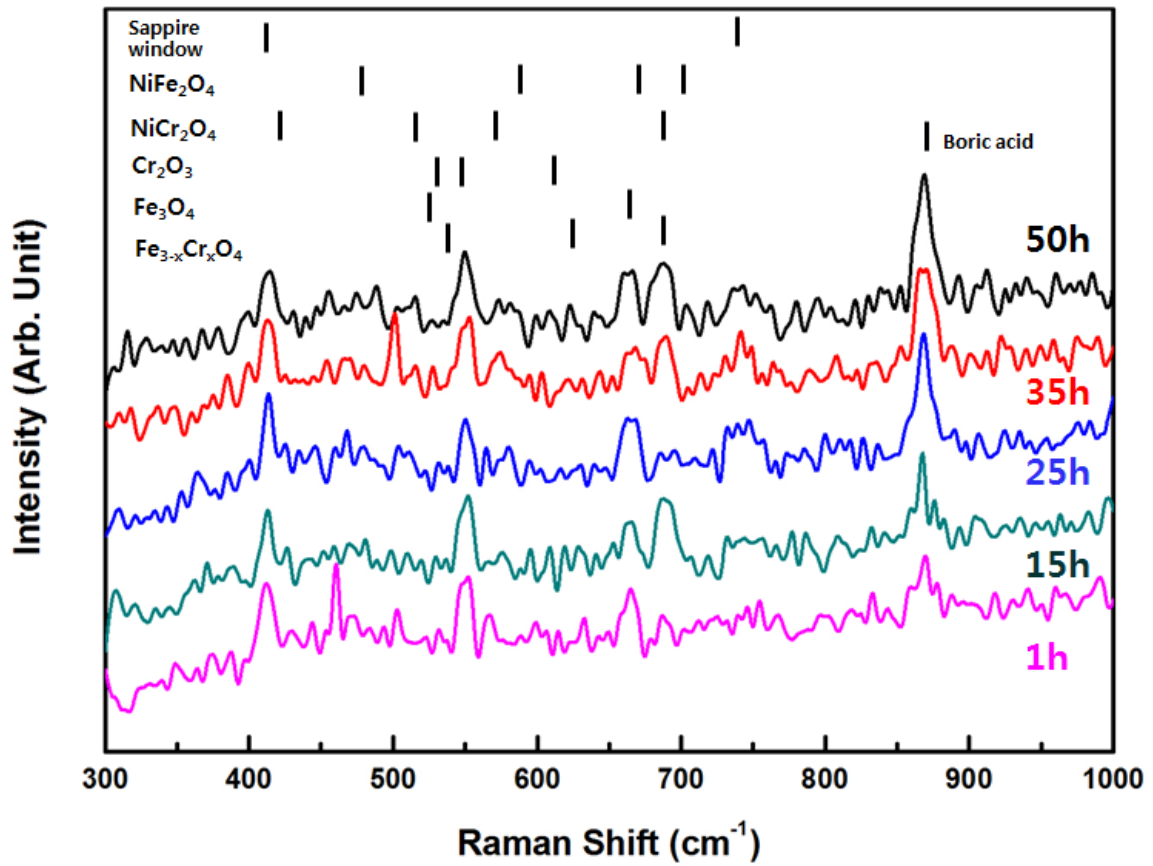
Figure 4-10. In situ Raman spectra of as-welded DMW interface at 300 ℃ for 50 h in simulated primary water condition
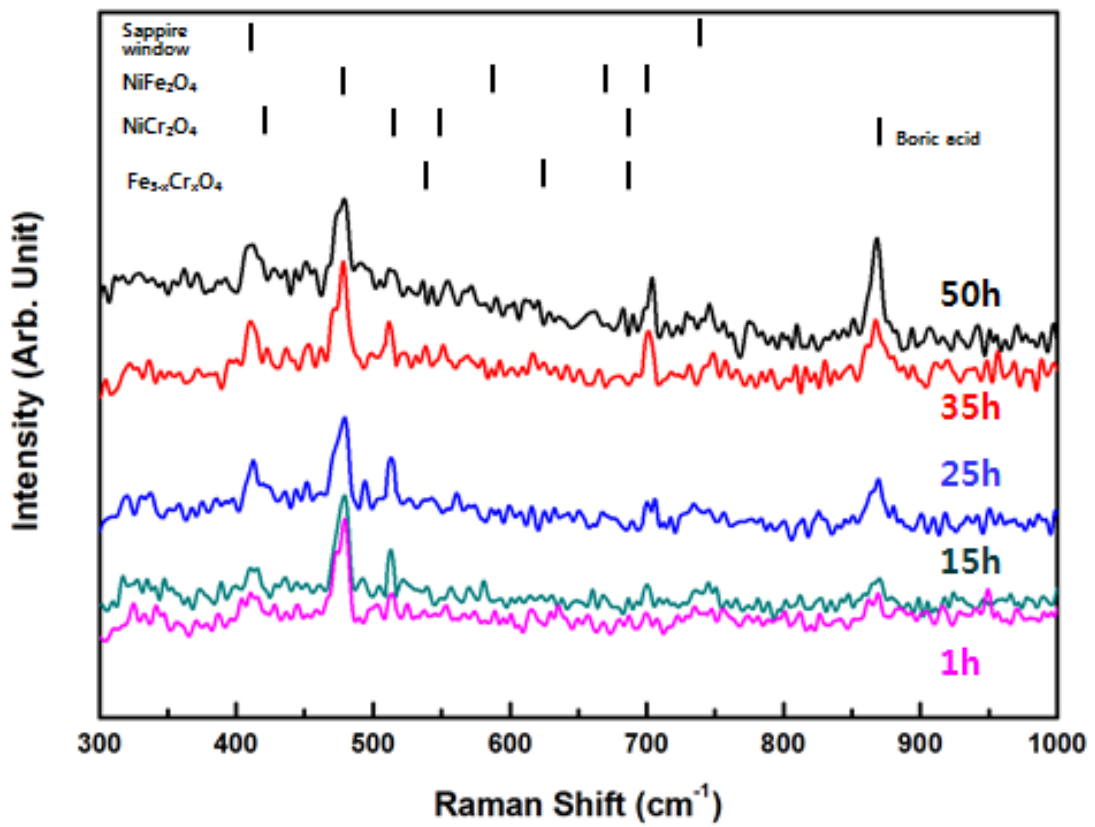
Figure 4-11. In situ Raman spectra of thermally aged DMW interface at 300 ℃ for 50 h in simulated primary
water condition
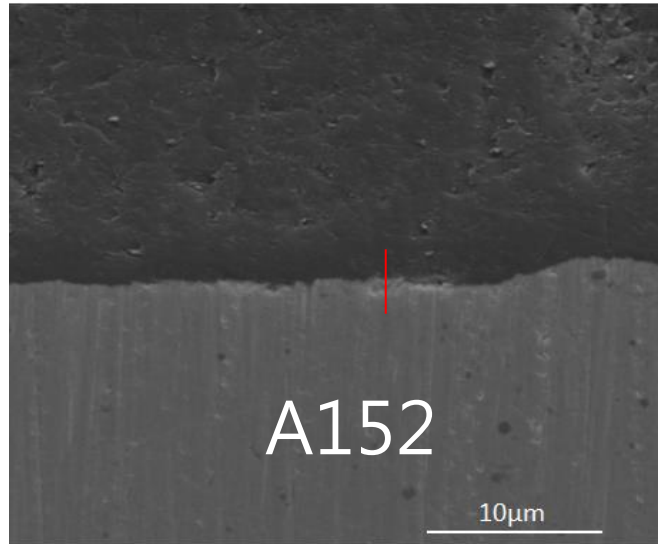
(a) SEM image of oxide film of DMW interface on A152 region
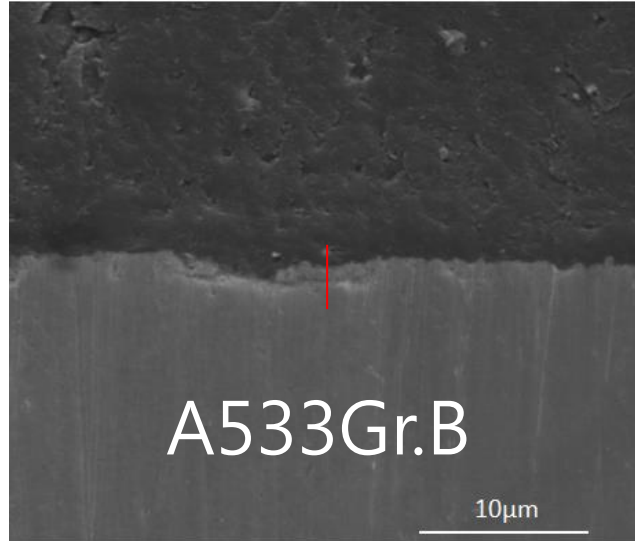
(b) SEM image of oxide film of DMW interface on A533Gr.B region
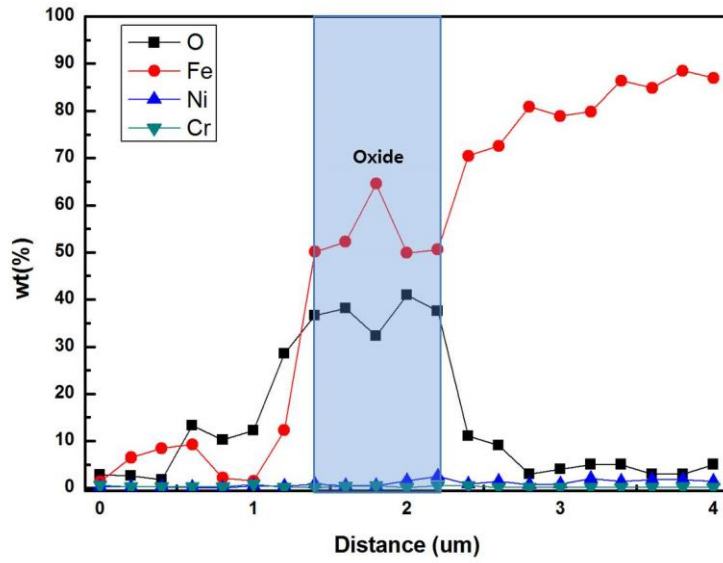
(c) EDS profiles of oxide film of DMW interface on A533Gr.B region
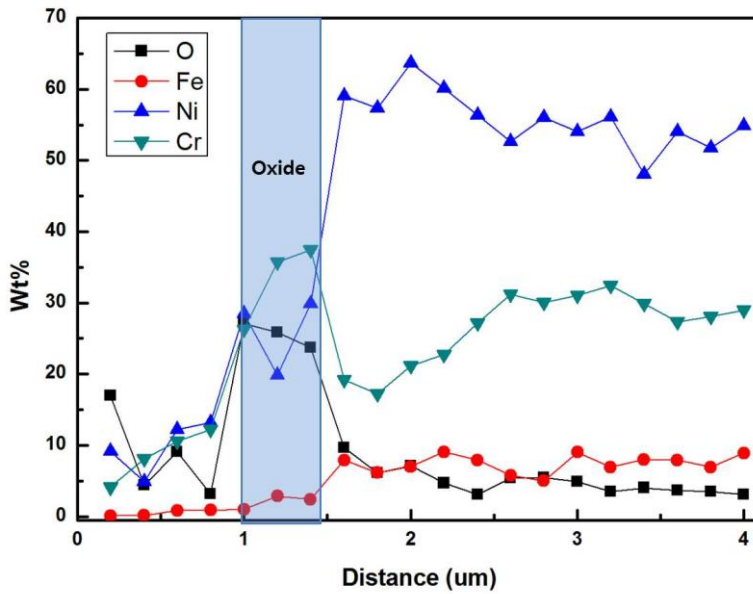
(d) EDS profiles of oxide film of DMW interface on A152 region

Figure 4-12 SEM images and EDS profiles of the oxide films on as-welded DMW interface region between A533Gr.B and A152
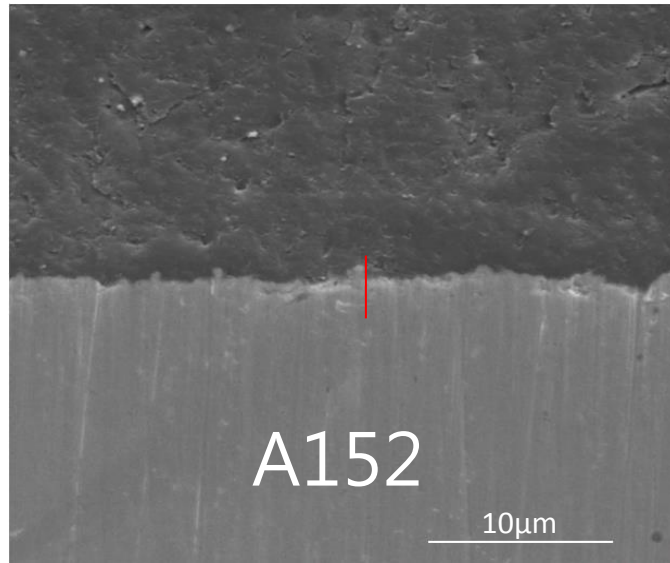
(a) SEM image of oxide film on thermally aged DMW interface of A152 region
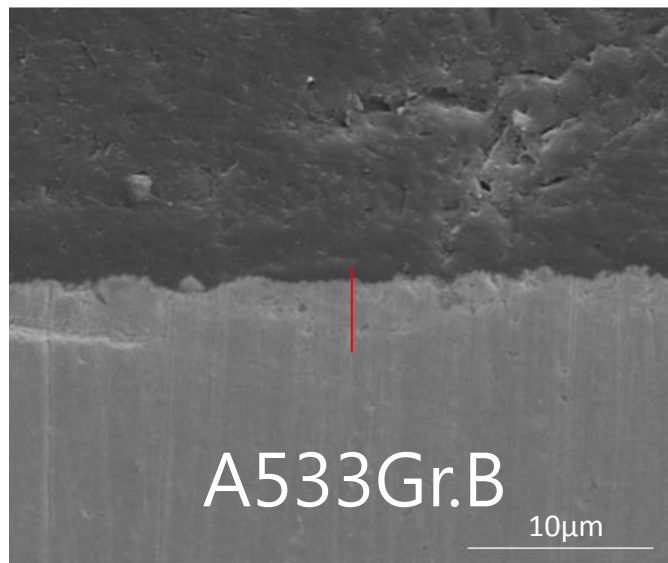
(b) SEM image of oxide film on thermally aged DMW interface of A533Gr.B region
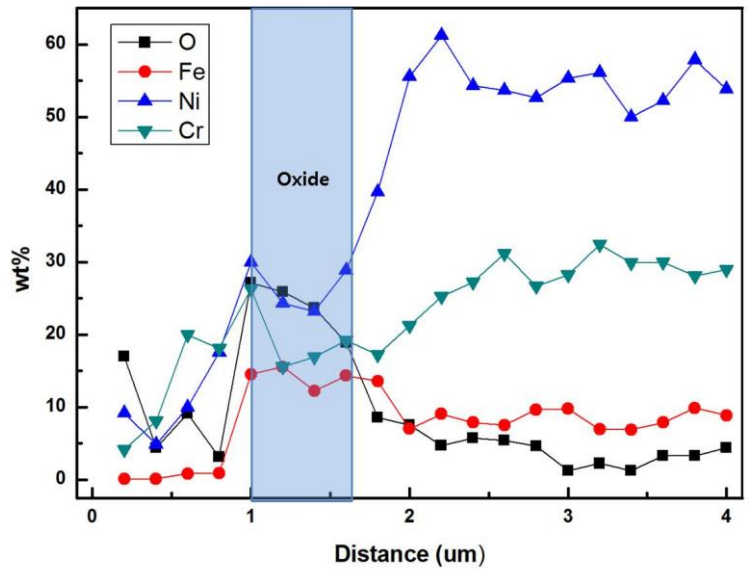
(c) EDS profiles of oxide film on thermally aged DMW interface of A152region
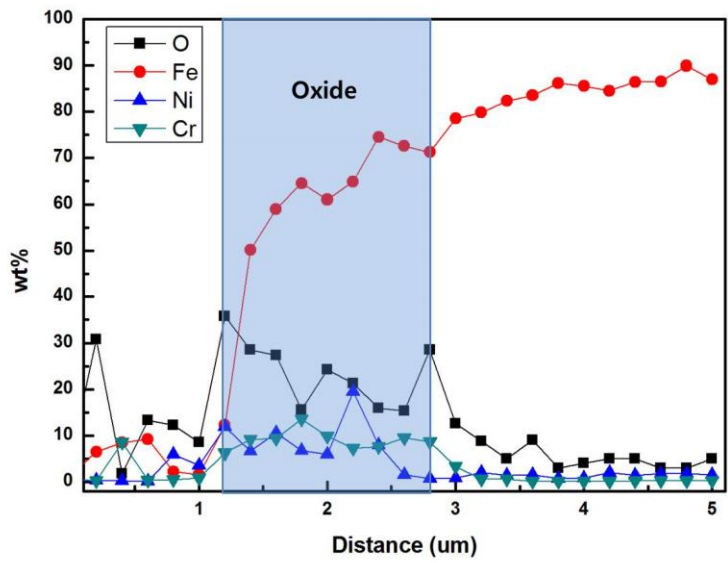
(d) EDS profiles of oxide film on thermally aged DMW interface of A533Gr.B region

Figure 4-13. SEM images and EDS profiles of the oxide films on thermally aged DMW interface region between A533Gr.B and A152

68
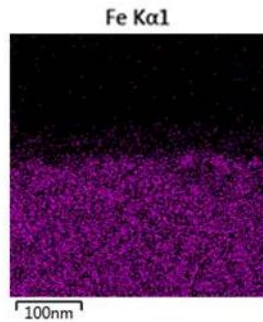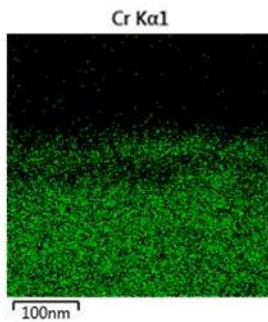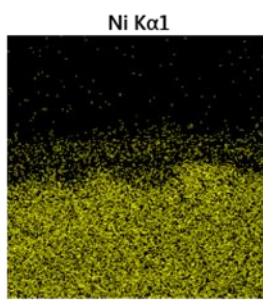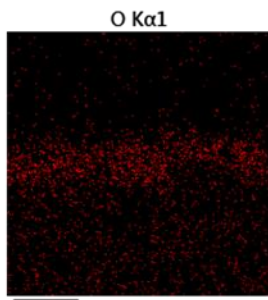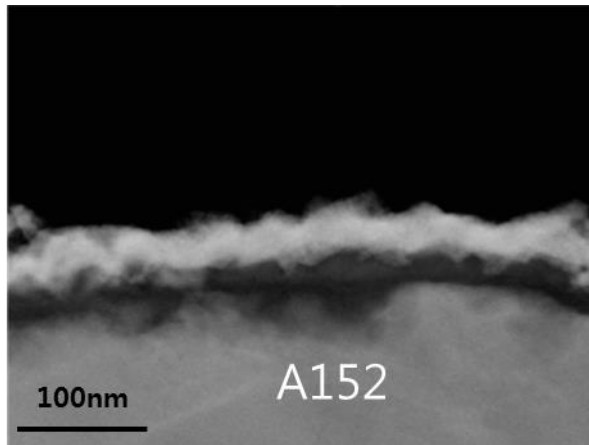
(a)
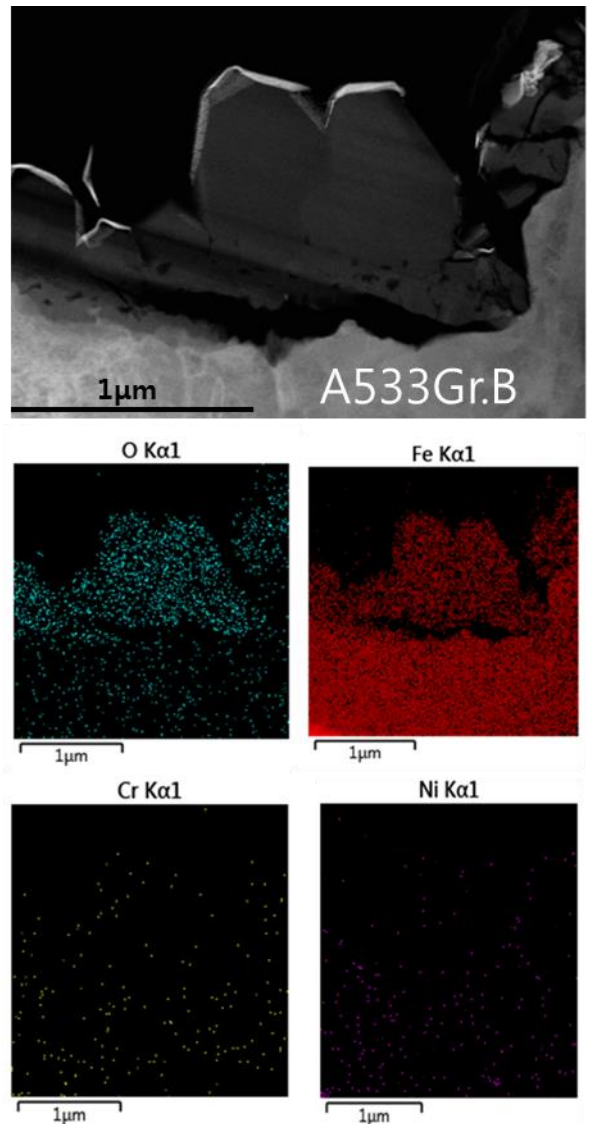
(b)

Figure 4-14. TEM images and EDS profiles of the oxide films on as welded DMW interface region between (a) A152 and (b) A533Gr.B
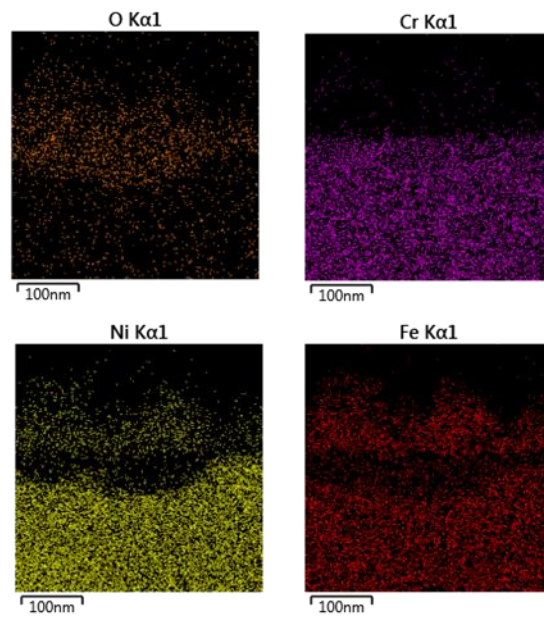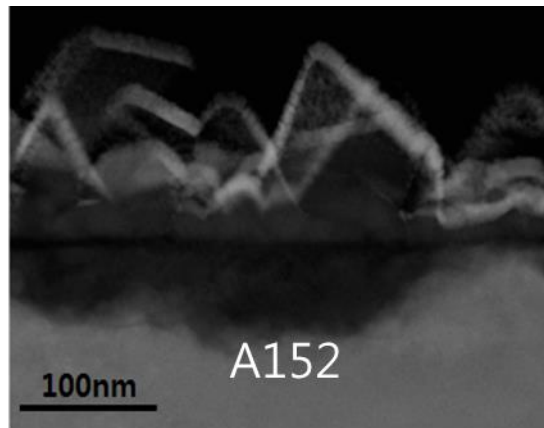
(a)
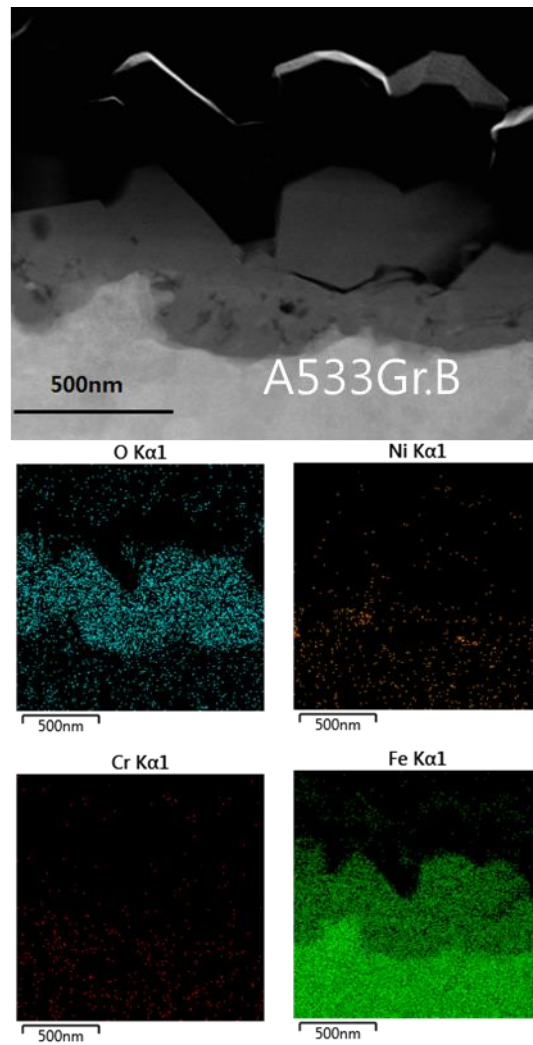
(b)

Figure 4-15. TEM images and EDS profiles of the oxide films on thermally aged DMW interface region between (a) A152 and (b) A533Gr.B

V. Discussion

5.1. Analysis of measured X-ray reflectivity data

Before analysis of measured X-ray reflectivity data, the data quality can be evaluated. The acquired data shows the very high quality even in low intensity reason. Refer to literatures [12, 77], CTR measurements were performed only for NiO(111) single crystal or Ni(111) and the measured data were available to estimate the atomistic structure of NiO(111) only. Comparing the Medway et al. work [12] with results in this study as shown in figure 5-1, they measured the CTR for Ni(111) in KOH solution with $10^{-1} \sim 10^{2}$ intensity range and there are no data point below 10^{-1} intensity. While the intensity range of the CTR data in this study is from 10^{-4} to 10^{1}, and the several data points in low intensity region($<10^{-1}$)with low error were measured. The data in low intensity region contain key information of interface structure. For this reason, the interface structure can be defined not only NiO-liquid also Ni/NiO.

For the data analysis, set up the structure factors and fitting procedure were conducted. Firstly, setting the structural model for the test specimen was performed. Figure 5-2 shows the Specular X-ray reflection from a stack of unit cells. The X-rays are reflected from a stack of unitcells consisting of Ni layers and NiO layers on the Ni substrate. The total intensity is proportional to the square of the sum of structure factors for each layer. The structure factor is defined as

$$F_{total} = F_{uc}F_{ctr} + F_{interface} + F_{amorphous} \qquad (5\text{-}1)$$

Where the $F_{uc}F_{ctr}$ is structure factor for substrate and $F_{interface}$ is structure factor of nickel layer and layered nickel oxide layer. The $F_{amorphous}$ layer is structure factor for amorphous nickel oxide layer. The unit cell structure factor for specular X-ray reflectivity is known and given by

$$F_{uc} = \sum_{k=0}^{N_{uc}} O_{uc}[k] \cdot f_{uc}[k] \cdot e^{(-1/2 \cdot u_{uc}[k] \cdot q^2)} \cdot e^{(i \cdot d_{Ni} \cdot r_{uc}[k] \cdot q)} \qquad (5\text{-}2)$$

where the $O_{uc}[k]$ is electron occupancy of Kth atom, $f_{uc}[k]$ is scattering factor for kth atom and thermal displacement of kth atom is $u_{uc}[k]$. The position of kth atom is also contained as $r_{uc}[k]$ and d_{Ni} is atomic separation distance of nickel.

The structure factor of F_{ctr} is defined as follow

$$F_{ctr} = 1/(1 - e^{i \cdot q \cdot d_{Ni}}) \qquad (5\text{-}3)$$

Therefore, the structure factor of substrate is multiply the structure factor of unit cell with structure factor of CTR

The structure factor of interface is sum of surface and oxide layer. That is,

$$F_{interface} = F_{surf} + F_{ox} \tag{5-4}$$

The structure factor of surface and oxide can calculate using follow equations

$$F_{surf} = \sum_{k=0}^{N_{surf}} O_{surf}[k] \cdot f_{surf}[k] \cdot e^{(-1/2 \cdot u_{surf}[k] \cdot q^2)} \cdot e^{(i \cdot d_{Ni} \cdot r_{surf}[k] \cdot q)} \tag{5-5}$$

$$F_{ox} = \left[\sum_{k=0}^{N_{ox}} O_{ox}[k] \cdot f_{ox}[k] \cdot e^{(-1/2 \cdot u_{ox}[k] \cdot q^2)} \cdot e^{(i \cdot d_{NiO} \cdot r_{ox}[k] \cdot q)} \right] \cdot e^{(i \cdot q \cdot H_{suf})} \tag{5-6}$$

Where, the $N_{surf} = 3$ and O_{surf} and O_{ox} are electron occupancy of kth atom of surface and oxide, respectively. The d_{nio} is distance between Ni and oxygen and f_{surf} and f_{ox} is scattering factor for surface and oxide layer.

The structure factor for amorphous layer is defined as follows

$$F_{l1} = N_{m1} f_{l1} \cdot e^{\{-\frac{1}{2} \cdot (q \cdot \sigma_{01})^2\}} \cdot e^{\{i \cdot q \cdot pos1\}} \tag{5-7}$$

$$F_{l2} = N_{m2} f_{l2} \cdot e^{\{-\frac{1}{2} \cdot (q \cdot \sigma_{02})^2\}} \cdot e^{\{i \cdot q \cdot pos2\}} \tag{5-8}$$

Where N_{m1} and N_{m2} are number of molecule of layer 1 and 2, and σ_{01} and σ_{02} are width of layer 1 and 2, respectively. The positions of the layer are defined as pos1 and pos2. Therefore, the structure factor for amorphous layer can defined as summation of F_{l1} and F_{l2}

$$F_{amorphous} = F_{l1} + F_{l2} \tag{5-9}$$

After setting up the all structure factors the least square fitting were performed to find best value for all parameters. The initial values for all parameters were summarized in Table 5-1. The fitting were performed by IGOR software. The fitting results are shown in Figure 5-3 and the parameters after fit summarized in table 5-2.

74

5.2. Atomistic structure of Ni(110)/NiO and water effect

The relationship between $\triangle Q$ and distance is shown in eq. (5-10).

$$\triangle Q = n2\pi/d \qquad (5\text{-}10)$$

Using eq. 5-10 and fitted parameters, the changes in the position of atoms and thickness of layers can be analyzed. According to the fitted results, slightly stressed Ni and NiO layer about 5Å thick were formed on the relaxed Ni layer, and the top layer would be amorphous NiO layer with 13Å thick. Figure 5-4 shows the illustration of the atom position and thickness of each layer.

In order to analysis the water effect, structure factor of water layer added in to the total structure factor F_{total}. The structure factor of water can be written as eq. (5-11)

$$F_{water} = f_{water} \cdot e^{\left\{-\frac{1}{2}(q \cdot \sigma_0)^2\right\}} / \left[1 - e^{\left\{-\frac{1}{2} \cdot (q \cdot \sigma_{bar})^2\right\}} \cdot e^{i \cdot q \cdot c_w}\right] \qquad (5\text{-}11)$$

where σ_0 is interpreted as the vibration amplitude of the water layer, and σ_{bar} is a parameter that specifies how quickly the vibration amplitude increases for successive layer into the fluid. c_w is separation distance of Gaussian peaks. This expression shows that the σ_0 acts as an overall Debye-Waller factor, as it would for any atom in the structure factor calculation.

Figure 5-5 shows the fitted result for CTR data from water injection and all fitted parameters summarized in Table 5-3. As shown in figure 5-5, the curvature features within middle Q range which showed inNi(110)/NiO-helium results, were disappeared. There are many possibilities to fit the data due to the absence of data in middle Q range. The curvature features related the atomic structure of middle layer of the structure or interface. The disappearance of the curvature in the middle range only can explained through changes in atomic position at middle layers or interface. It can be consider that the water affects the atomic structure of middle layers or interface. Generally, the water affects only few top layers not middle layer but in this study, the water affects the middle layers. In order to figure out the reason, characterization of top oxide layer is very important. Unfortunately, the characterization had not been performed before and after X-ray reflectivity measurements. According to the Mitchell and M.J. Graham work [78], the condition of the oxide can be estimated whether single crystal or polycrystalline. They found that single crystal oxide converts to polycrystalline oxide as decreasing oxygen pressure at a particular temperature as shown in figure 5-6. The sample temperature at the oxide were formed on the surface is would be 200~250°C and the oxygen gas injected at 10^{-7}torr pressure. Therefore, the oxide on the top surface of the sample would be polycrystalline NiO at that temperature and pressure conditions.

5.3. Role of chromium for the oxygen diffusion in Ni and Ni-Cr binary alloy

The results showed different tendency depending on the position of the NN chromium atoms. In case of 1NN chromium atom existing in front of oxygen (figure 4-5 (a)), the calculated activation energies for diffusion of oxygen were 0.93 eV and 0.71 eV along the O-O and O-T-O diffusion pathways, respectively22. In case of 1NN chromium atom existing at the back of oxygen (figure 4-5 (b)), the calculated activation energies were 1.61 eV and 1.23 eV along the O-O and O-T-O pathways, respectively. In case of 2NN chromium atoms existing in the front of oxygen, the activation energies were calculated to be 0.76 eV and 0.49 eV along the O-O path and O-T-O diffusion paths, respectively. Likewise, with 2NN chromium atoms existing at the back of the oxygen, the calculated energies were 1.98 eV and 1.57 eV as shown in figure 4-5 (d). This shows that, despite the same number of NN chromium atoms, the activation energies varied with variations in the relative position of chromium atoms.

According to the framework, the activation energies of oxygen diffusion in pure Ni were found to be 1.44 eV for O-O path and 1.12 eV for O-T-O path [56].Comparing the calculated activation energies for pure nickel with that of the 1NN chromium cases, the observed variation trend can be summarized as follows. In case of 1NN chromium atom existing in front of the oxygen, the activation energies decreased from 1.44 eV to 0.76 eV along the O-O path, and from 1.12 eV to 0.49 eV along the O-T-O path. On contrary, when the 1NN chromium atom existed at the back of the oxygen, the activation energies increased from 1.44 eV to 1.61 eV along the O-O path, and from 1.12 eV to 1.23 eV along the O-T-O path. This could be attributed to factors such as higher oxygen affinity of chromium, smaller van der Waals radius and fewer numbers of electrons in chromium (128 pm radius and 24 electrons) compared to nickel (165 pm radius and 28 electrons).

In particular, the oxygen affinity could be explained based on Gibbs free energy for the formation of oxides. The standard Gibbs free energy for the formation of Cr_2O_3 at 773K is -927.7 KJ/mol, while that of NiO is reported to be -168.9 KJ/mol [79]. This clearly indicates that chromium could easily form an oxide layer than nickel. When these chromium atoms exist in front of the oxygen, the chromium atoms tend to pull the oxygen atom because of their higher oxygen affinity. Additionally, the diffusion space along the path of oxygen diffusion between nickel and chromium or chromium and chromium is larger than that between nickel and nickel. Furthermore, when the oxygen atoms come closer, the smaller number of electrons in chromium causes a lower repulsive force than nickel. This accounts for the lower activation energy in chromium than that of pure nickel.

On analogy, when oxygen is diffused with the NN chromium atoms at the back, the activation energies are higher than that of pure nickel. This is because, the high oxygen affinity of chromium

atoms tend to pull the oxygen atoms, requiring higher energy for the diffusion of oxygen along chromium than in nickel. In other words, the chromium atoms increase the activation energy for the diffusion of oxygen. Table 4-1 and 4-2 show the summary of the calculated activation energies as increasing of NN chromium atoms in front of oxygen or at the back of oxygen, respectively.

In case of increment of NN chromium atoms in front of oxygen, chromium atoms replaced the NN nickel atoms existing in front of the oxygen atoms, with the increase in the number of NN chromium atoms. On comparing the diffusion in pure nickel with those of 1NN chromium (A) and 2NN chromium (A), the activation energies were found to decrease from 1.44 eV to 0.76 eV along the O-O path and from 1.12 eV to 0.49 eV along the O-T-O path. Furthermore, with the 2NN chromium atoms existing at the back of the oxygen, the activation energies were found to decrease. When the NN nickel existed in front of oxygen were replaced by chromium (Table 4-1), the activation energies along the O-O and O-T-O path were calculated to be 1.89 eV and 1.45 eV, respectively, in case of 3NN Cr_2 and 1.83 eV and 1.34 eV, respectively, in case of 4NN Cr. On analyzing the results from 2NN Cr (B), 3NN Cr_2, and 4NN Cr cases it could be observed that, as the NN nickel atoms existed in front of oxygen atoms, the activation energies decreased from 1.98 eV to 1.83 eV along the O-O diffusion path and from 1.57 eV to 1.34 eV along the O-T-O diffusion path.

In case of increment of NN chromium atoms at the back of oxygen, the chromium atoms replaced the NN nickel atoms existing at the back of the oxygen, with the increase in the number of NN chromium atoms (Table 4-2). On comparing with pure nickel, 1 NN Cr (B) and 2 NN Cr (B), it could be observed that the activation energies increased from 1.44 eV to 1.98 eV along the O-O diffusion path and from 1.12 eV to 1.57 eV along the O-T-O diffusion pathway. Moreover, in case of 2 NN chromium atoms already existing in front of oxygen, the activation energies were found to increase. As the chromium atoms replaced the NN nickel atoms existing at the back of the oxygen, the calculated activation energies increased from 0.76 eV to 1.83 eV along the O-O diffusion path and from 0.49 eV to 1.34 eV along the O-T-O diffusion path. Since the replaced 3rd and 4th NN chromium atoms exist in the direction opposite to that of the oxygen diffusion, the diffusing oxygen atoms would be far from 3rd and 4th chromium atoms. However, the chromium has very strong oxygen affinity, thereby requiring higher energy for the oxygen to diffuse along the pathways. Finally, the activation energy for oxygen diffusion with 4NN chromium atoms is found to be higher than that of pure nickel.

The highest activation energy for each diffusion path is seen in the case of 2NN Cr (B). The calculated activation energy was found to be 1.91 eV along the O-O path and 1.57 eV along the O-T-O path as shown in Figure 4-5(d). They were obtained by the presence of two nickel atoms in the middle of diffusion path, with the chromium atoms existing at the back position to the direction of

oxygen diffusion. Such a configuration means that the space for oxygen diffusion is similar to that of pure nickel. This implies that the oxygen needs higher energy to diffuse. These 2NN Cr (B) results provide detailed explanation on the effects of oxygen affinity and diffusion space on oxygen diffusion, in Ni-Cr binary alloy.

The diffusion coefficient can be classically expressed in terms of Arrhenius law, as shown in the following equation:

$$D = D_0 e^{-Q/kT} \qquad\qquad (2\text{-}3)$$

,where D_0 is the temperature-independent pre-exponential factor, Q is the activation energy, and k is the Boltzmann constant. According to this equation, higher activation energy implies lower diffusion coefficient. Referring to the work of Chattopadhyay and Wood [80], the oxygen diffusion coefficient at 1000 ℃ was calculated to be 2.4×10^{-9} cm^2/s and 1.74×10^{-11} cm^2/s in nickel and Ni-Cr (12 wt%) binary alloy, respectively. On comparing these diffusion coefficients, it could be confirmed that Ni-Cr binary alloy has higher activation energy than that of pure nickel.

The experimental activation energy of oxygen in Ni-Cr binary alloy was found to be 1.69 eV35. It has been reported that, the Ni-Cr binary alloy forms FCC structure when chromium is less than 20 wt% [81]. The chromium atoms gather and distribute in the nickel matrix. Consequently, the oxygen diffusion in Ni-Cr binary alloy is expected to be very similar to the case of 4NN Cr analyzed in this study, in which case, the activation energies were calculated to be 1.81 eV and 1.34 eV along the O-O and O-T-O diffusion path, respectively. The activation energy obtained from experimental data was found to be located in the middle range of results from 4NN Cr case. Hence, the results obtained from this theoretical study were found to be in good agreement with the experimental values. It seems evident that the activation energy increases with the inclusion of chromium atoms. Hence, it is obvious that the chromium atoms act as a barrier for the diffusion of oxygen.

However, in Ni-Cr binary alloy, most of the oxidation problems occur along the grain boundary. Consequently, first principles studies on the calculation of grain boundary structure have been reported recently [82]. These studies primarily calculated the structure and bulk energy at grain boundaries. However, understanding the oxidation problems along the grain boundary requires study on atomic position with time, in addition to the calculated energy. Furthermore, grain boundaries can be of several types depending on the formation angle. This demands consideration of more number of atoms that could simulate the oxidation phenomenon at the grain boundaries. Therefore, this model needs to be scaled up using molecular dynamics in order to model the diffusion at the grain boundaries. The parameters obtained from the first principles studies will form the basis for the

molecular dynamics studies in the near future. Hence we believe that, the outcome of this study is expected to act as a cornerstone to link first principles and molecular dynamics study of SCC. Accordingly, our future research will focus on calculating the grain boundary diffusion in metal and alloy by linking the first principles and molecular dynamics methods.

5.4. Aging effect on the oxide formation at the nickel base alloy/low alloy steel dissimilar metal weld interface

The results obtained by in situ Raman spectroscopic measurements match well with the data reported in the literature. The minor variations observed between the data obtained in this study and the reported data could be attributed to the difference in the incident laser wavelength, test temperature, and pressure on the Raman signal of the two data [83, 84]. In general, temperature and pressure cause isotropic and anisotropic deformations in molecules and crystals, respectively. Variations of wave number as the temperature or pressure strongly depend on the structural phase transitions.

Based on the extensive analysis, the possible chemical reactions involved in the phase formation of oxide and spinel from the Ni-Cr-Fe ternary system in water are described as follows.

$$Ni^{2+} + H_2O \rightarrow NiO + 2H^+ \tag{1}$$

$$Fe^{3+} + H_2O \rightarrow 3FeO^+ 2H^+ \tag{2}$$

$$2CrO_4^{2-} + 5H_2O + 6e \rightarrow Cr_2O_3 + 10OH^- \tag{3}$$

$$Fe + 2H_2O \rightarrow Fe^{2+} + 2OH^- + H_2 \tag{4}$$

$$Fe^{2+} + 2OH^- \rightarrow Fe(OH)_2 \quad (Soluble) \tag{5}$$

$$Fe(OH)_2 \rightarrow Fe_3O_4 (Magnetite) + H_2 + H_2O \tag{6}$$

$$3Fe^{2+} + 4H_2O \rightarrow Fe_3O_4(s) + 6H^+ + H_2(g) \tag{7}$$

$$2Fe^{2+} + 3H_2O \rightarrow Fe_2O_3(s) + 4H^+ + H_2(g) \tag{8}$$

$$NiO + Fe_2O_3 \rightarrow NiFe_2O_4 \tag{9}$$

$$NiO + Cr_2O_3 \rightarrow NiCr_2O_4 \tag{10}$$

$$FeO + Cr_2O_3 \rightarrow FeCr_2O_4 \tag{11}$$
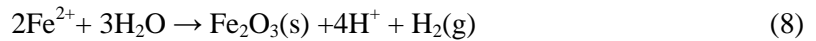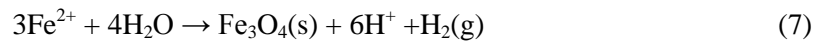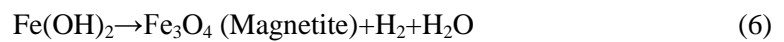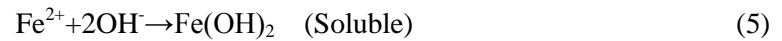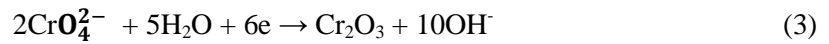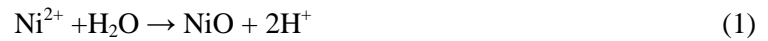
Figure 5-7 illustrates the potential-pH diagram for Ni, Cr, and Fe species for the Ni-Cr-Fe ternary system in water at 300 ℃. The red circle in the figure represents the test condition in this

study. Calculations of the electro-chemical potential-pH diagrams for Ni, Cr, and Fe species in the Ni-Fe-Cr ternary system were performed using the commercial computer program HSC 5.0 [24]. The calculation allows the formation of various stoichiometric spinels. According to the potential-pH diagram, $NiCr_2O_4$ and $FeCr_2O_4$ can be formed in this condition.

In the case of the as-welded DMW, Cr_2O_3 and Fe_3O_4 peaks were continuously observed in the in situ Raman spectra measurement. Although, the peak intensity of the iron-chromium spinel is very low after 1 h of exposure to temperature, the peak intensity increases with increase in the test time. In general, peak intensity is related to the amount of the material. Therefore, the observed increase in the peak intensity with test time could be related to the continuous formation of iron-chromium spinel. The ex situ Raman spectra also show peaks corresponding to the magnetite and iron-chromium spinel. According to the ex situ EDS results, the oxide components after the in situ Raman spectra measurement of the as-welded A152 include Ni and Cr, while that of A533Gr.B include Fe. According to the previously reported studies [23, 26], either Cr_2O_3 or Fe_3O_4 was first observed during the in situ Raman spectroscopic analysis of stainless steel or nickel-based alloy under heating. This could be attributed to the fact that these oxides have low Gibbs free energy to form an oxide. Furthermore, as Cr_2O_3 or Fe_3O_4 meet Cr or Fe ions, new oxide scale grows up on a previous oxide scale. During the welding process, a dilution region, where Ni and Cr diffused from A152 to LAS and Fe diffused from LAS to A152, was formed at the interface of DMW [69]. Therefore, it is possible that the formation of the iron-chromium spinel and nickel-iron spinel on the LAS or A152 surface could occur.

In the case of the thermally aged DMW, various spinel peaks, namely iron-chromium spinel, nickel-chromium and nickel-iron spinel were observed through in situ Raman measurements. In case of as-welded specimen, the peaks of Cr_2O_3 and Fe_3O_4 were detected at 300℃ and the peaks for Ni-Cr or Fe-Cr spinels were detected after 15h or longer. For thermally aged specimen, however, the peaks of $NiCr_2O_4$ and $NiFe_2O_4$ were detected first in an hour and 15 hours, respectively. The change in the intensity of these peaks was observed. It is considered that the oxide layers of Cr_2O_3 or Fe_3O_4 were formed before the temperature reaching 300℃. And, spinel oxides seemed to be formed on them

when the measurement was performed at 300℃. As the time increases, the peak intensity of the nickel-chromium spinel decreases, while that of the nickel-iron spinel increases. Consequently, the nickel-chromium spinel formed on the surface of metal oxides, which subsequently meet the dissolved nickel ion from the base metal to form the nickel-iron spinel. The EDS results show that oxide films on the thermally aged DMW were composed of Ni, Fe, and Cr. Also, the ex situ Raman observation of the oxide films at the interface indicates the formation of nickel-iron oxide and iron-chromium spinel.

These differences can be caused by the diffusion-assisted chemical redistribution during thermal aging. The dilution region is originally created near the interface of the as-welded DMW because of the heat generated during the welding process. At the dilution region, Ni and Cr diffuse from A152 to A533Gr.B, while Fe diffuses from A533Gr.B to A152. The thermal aging assists these diffusion phenomena, which is confirmed by comparing the interface EDS profiles of the as-welded DMW and thermally aged DMW (Figure 5-8) [76]. The region of composition change is observed at the as-welded DMW interface, whereas it disappears for the thermally aged specimen, as shown in Figure 5-8 (a) and (b), respectively. Figure 5-8 (c) and (d) show the enlarged view of the interface, shown with a red box in Figure 5-8 (a) and (b). As evidenced from the Figure 5-8 (c) and (d), the composition gradient slopes for all elements of the as-welded DMW are steeper than those of the thermally aged DMW. It can be considered that the diffusion of Ni and Cr from A152 to LAS and that of Fe from LAS to A152 occur to a greater degree during thermal aging, compared to those in the as-welded DMW. Therefore, it is reasonable to believe that the diffusion-assisted chemical redistribution around the DMW interfaces induces changes in the oxidation behavior. These results are illustrated in Figure 5-9, which signifies the difference between the oxides formed at the as-welded DMW and thermally aged DMW interfaces. In the as-welded DMW interface, spinel of Fe-Cr or chromium oxide mixture is formed on Cr_2O_3 and Fe_3O_4, at the surface of A152 and A533Gr.B, respectively. On the other hand, at the thermally aged DMW interface, the $Fe_{3-x}Cr_xO_4$ layer, where the Ni-Cr spinel grew,

is formed either on the metal oxide or base metal. This is because of the chemical redistribution facilitated by thermal aging, which finally led to the continuous growth of crystalline $NiFe_2O_4$.

According to M. Sennour et. al. studied the oxide films at the surface of A690 in PWR primary water environments by TEM [85]. The oxide layer was divided in two layers. The internal layer was composed of continuous spinel layer such as $Ni_{(1-x)}Fe_xCrO_4$. Nodules of Cr_2O_3 were present at the interface between this spinel oxide and the alloy. The external layer is composed of large crystallites as spinel structure rich in iron($Ni_{(1-z)}Fe_{(2+z)}O_4$). And F. Wang [86]. conducted in situ Raman spectroscopy for films formed on A600 and A690 as a function of electro-chemical potential(ECP) at 320℃. A600 shows that the oxide films formed on the surface changed with ECP. A film of Cr_2O_3 forms at potential which A600 is susceptible to SCC. At potentials below the SCC maximum, the spinel oxide is most likely $FeCr_2O_4$. The films that form on A690, which is resistant to SCC in primary water, composed of mixture of Cr_2O_3 and spinel M_3O_4 at all potential ranges. According to these results, the oxide films on the as-welded DMW surface which were composed of Cr_2O_3 and M_3O_4 spinel mixture, can be considered that have resistance to SCC. While, oxide films on aged DMW surface were not. . According to the first-principles calculation results, the chromium or chromium oxide can take a role of diffusion barrier, and the chromium atoms in nickel layer make good condition for internal oxidation, and from the in-situ Raman results, the oxide films on the thermally aged DMW are manly Ni-rich spinels without chromium oxide. That is, the oxide films on the DMW easily occurs the internal oxidation phenomena and it can result in the decrease the SCC resistance.

TABLE 5-1. Initial values for all parameters

	Variable sin Program	Symbol	Best value
	d_spacing	d_{Ni}	1.247
	d_spacing_NiO	d_{NiO}	1.27
for	i	N_{uc}	1
unit cell	allatom_occupancy[i]	$O_{uc}[k]$	1
and CTR	scatFact_all[i]	$f_{uc}[k]$	28.3567
	allatom_u[i]	$u_{uc}[k]$	0.01
	atom_frac_pos[i]	$r_{uc}[k]$	0
	sumi	N_{surf}	3
	ManualAdd_occupancy[sumi]	$O_{surf}[k]$	1
for	ManualAdd_scaFact[sumi]	$f_{suf}[k]$	28.3567
surface	ManaualAdd_u[sumi]	$u_{surf}[k]$	0.01
	ManualAdd_pos[sumi]	$r_{surf}[k]$	
	ManualAdd_pos[0]	$r_{surf}[0]$	0
	ManualAdd_pos[1]	$r_{surf}[1]$	1
	ManualAdd_pos[2]	$r_{surf}[2]$	2
	TManualAdd_occupancy[sumi2]	$O_{ox}[k]$	
	TManualAdd_occupancy[0]	$O_{ox}[0]$	0.9
	TManualAdd_occupancy[1]	$O_{ox}[1]$	0.7
	TManualAdd_occupancy[2]	$O_{ox}[2]$	0.35
	TManualAdd_occupancy[3]	$O_{ox}[3]$	0.5
	TManualAdd_occupancy[4]	$O_{ox}[4]$	0.15
	TManualAdd_occupancy[5]	$O_{ox}[5]$	0.5
	TManualAdd_occupancy[6]	$O_{ox}[6]$	-0.05

TABLE 5-1. Initial values for all parameters (con't)

	Variable sin Program	Symbol	Best value
	Sumi2	N_{ox}	7
	TManualAdd_scaFact[sumi2]	$f_{ox}[k]$	
	TManualAdd_scaFact[0]	$f_{ox}[0]$	8.00115
	TManualAdd_scaFact[1]	$f_{ox}[1]$	28.3567
	TManualAdd_scaFact[2]	$f_{ox}[2]$	8.00115
for	TManualAdd_scaFact[3]	$f_{ox}[3]$	28.3567
Oxide	TManualAdd_scaFact[4]	$f_{ox}[4]$	8.00115
	TManualAdd_scaFact[5]	$f_{ox}[5]$	28.3567
	TManualAdd_scaFact[6]	$f_{ox}[6]$	8.00115
	TManaualAdd_u[sumi2]	$u_{ox}[k]$	
	TManaualAdd_u[0]	$u_{ox}[0]$	0.01
	TManaualAdd_u[1]	$u_{ox}[1]$	0.01
	TManaualAdd_u[2]	$u_{ox}[2]$	-0.09
	TManaualAdd_u[3]	$u_{ox}[3]$	0.01
	TManaualAdd_u[4]	$u_{ox}[4]$	-0.09
	TManaualAdd_u[5]	$u_{ox}[5]$	0.01
	TManaualAdd_u[6]	$u_{ox}[6]$	-0.09

TABLE 5-2. Parameters after fitting

	value	stand. Dev.(±)	frac
#mole_1	6.59986	1.59	24.09142012
#mole_2	24.294	2.92	12.01942867
offset_1	7.94323	0.0942	1.185915553
sig_0_2	2.4867	0.0749	3.012023968
offset_2	1.5034	0.0355	2.361314354
sigma_1	2.6195	0.107	4.084748998
position0	0.73418	0.0144	1.961371871
position1	1.199	0.00633	0.52793995
position2	2.0545	0.00607	0.295449014
position3	2.6751	0.0145	0.542035812
position4	3.2916	0.00857	0.260359703
position5	4.0604	0.00588	0.144813319
occupancy0	0.57478	0.00894	1.55537771
occupancy1	0.79654	0.0283	3.552866146
occuancy2	0.74931	0.0154	2.05522414
occupancy3	0.3787	0.0163	4.304198574
occupnacy4	0.25987	0.0121	4.656174241
occupnacy5	0.21249	0.00639	3.007200339

TABLE 5-3. Parameters after fitting for CTR data for Ni(110)/NiO-water

	value	stand. Dev.(±)	frac
sigma_zero_la	3.3206	0.917	27.61549
sigma_zero_la_2	2.3112	0.757	32.75355
offset_water1_2	1.5754	0.23	14.59947
num_water_molec_2	23.571	2.68	11.3699
offset_water2	11.952	0.794	6.64324
offset_water1	7.5611	0.697	9.218235
sigma_zero_ar	1.2347	0.469	37.98494
num_water_molec	12.561	9.21	73.32219
Pos[0]	0.73935	0.0573	7.750051
Pos[1]	1.496	0.0476	3.181818
Pos[2]	2.4866	0.0403	1.620687
Pos[3]	3.4182	0.0605	1.769937
Pos[4]	4.3568	0.0696	1.597503
occupancy[0]	0.82726	0.13	15.71453
occupancy[1]	0.97749	0.18	18.41451
occupancy[2]	0.88047	0.171	19.42145
occupancy[3]	0.53325	0.28	52.5082
occupancy[4]	0.47629	0.139	29.1839
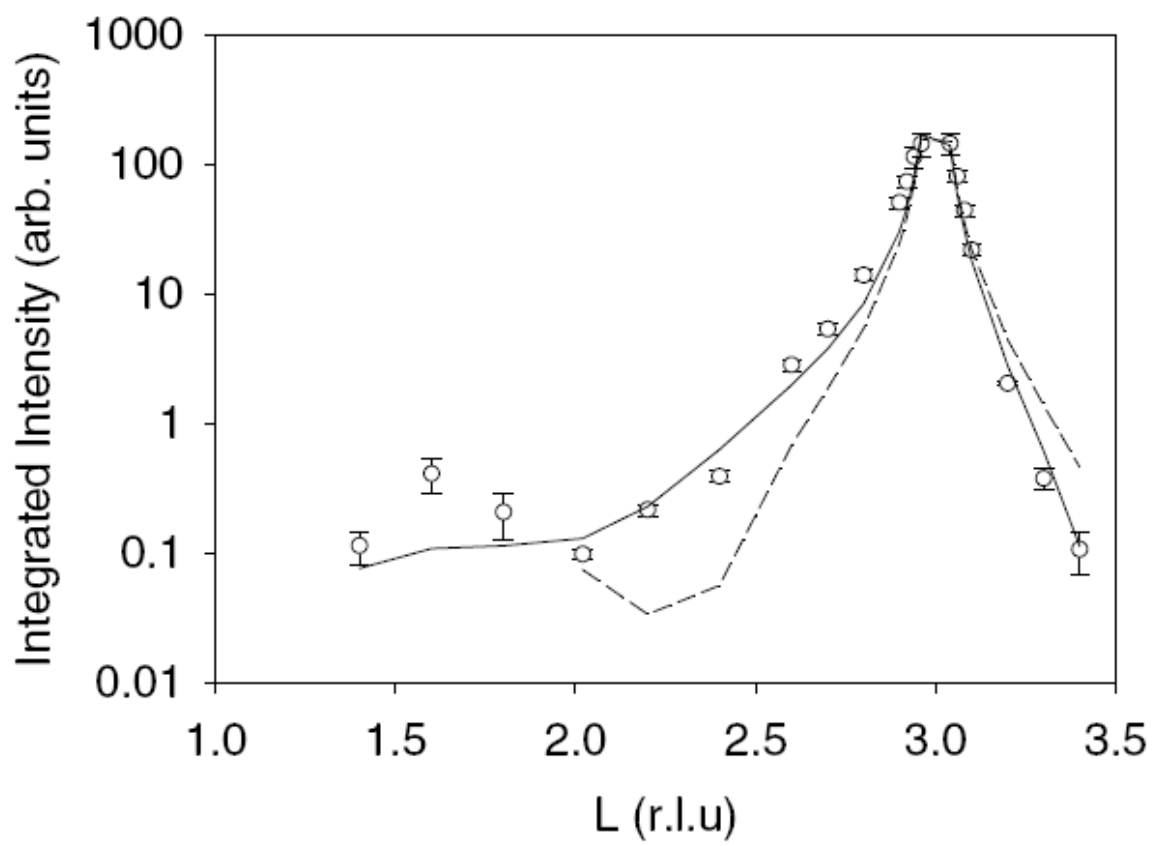
Figure 5-1. The specular (0,0,L) CTR data for the Ni(111) crystal in 1M KOH [12]
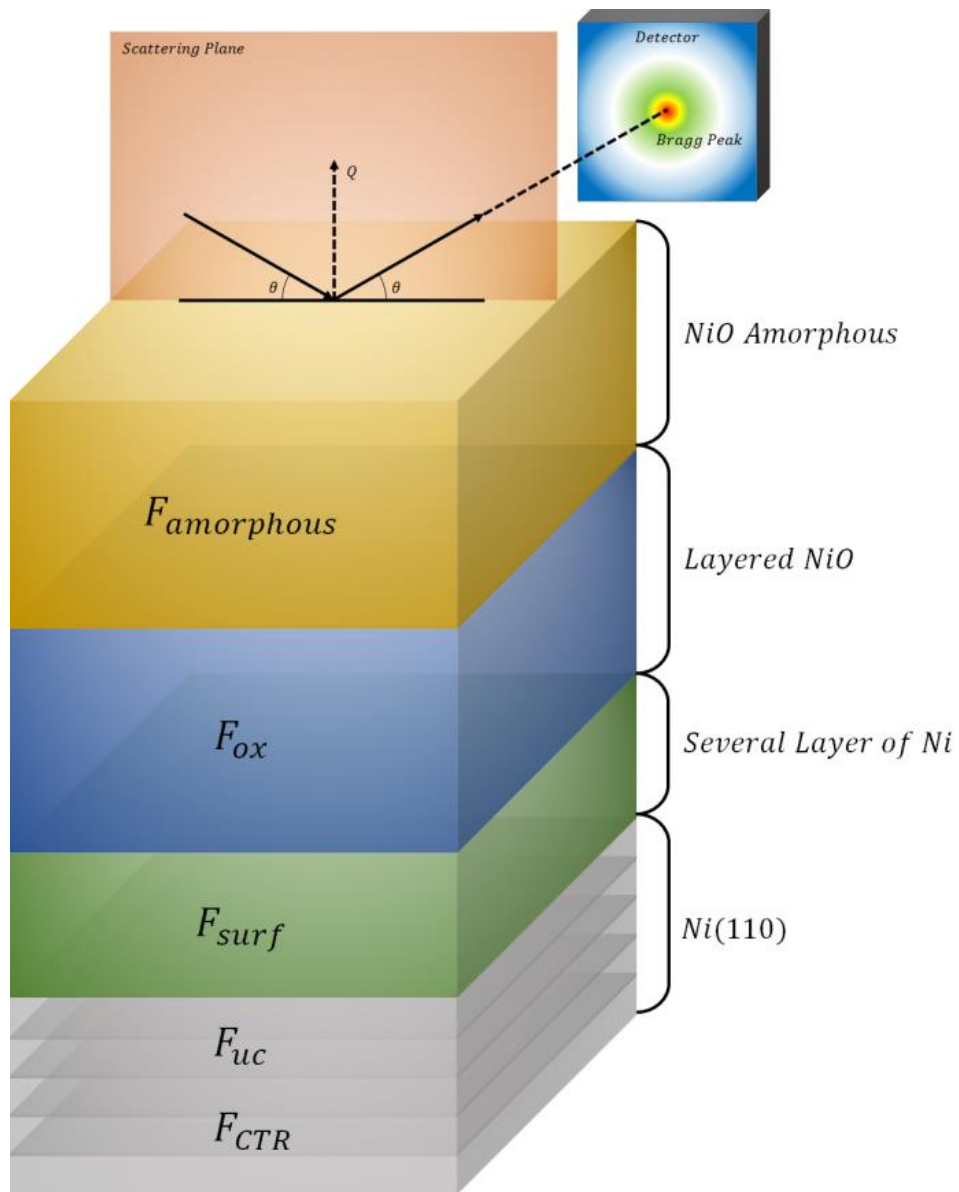
Figure 5-2. The specular X-ray reflection from a stack of unit cells
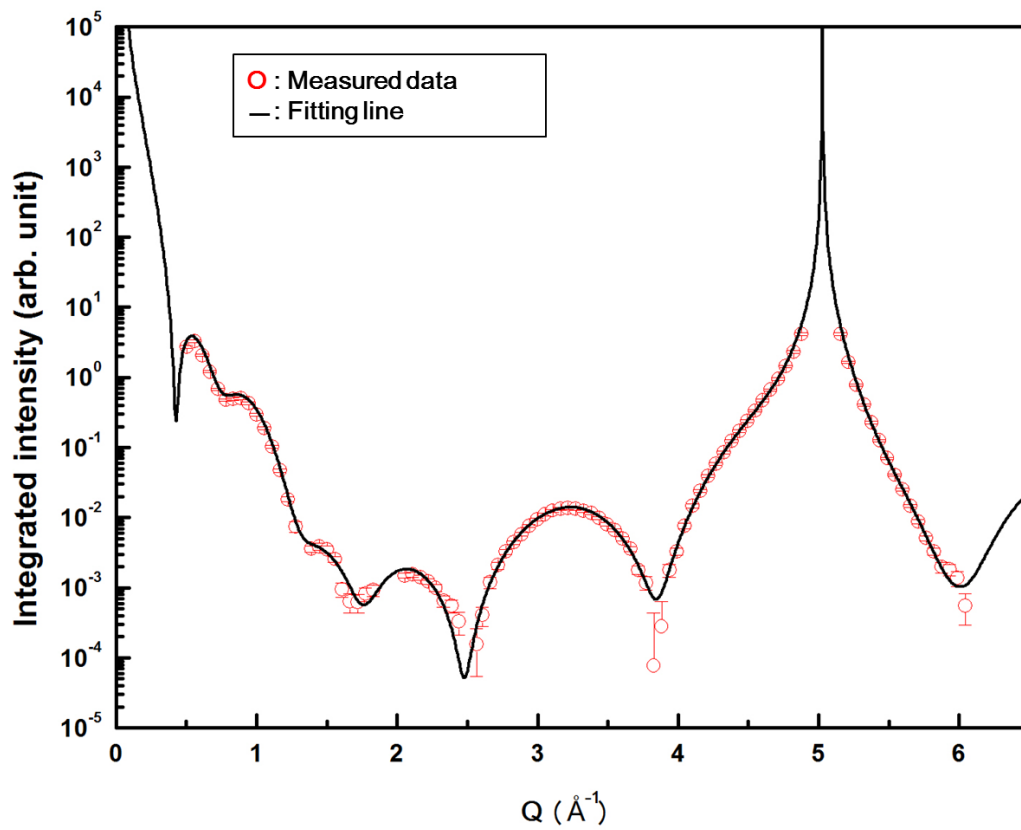
Figure 5-3. The fitting result for Ni(110)/NiO-helium structure
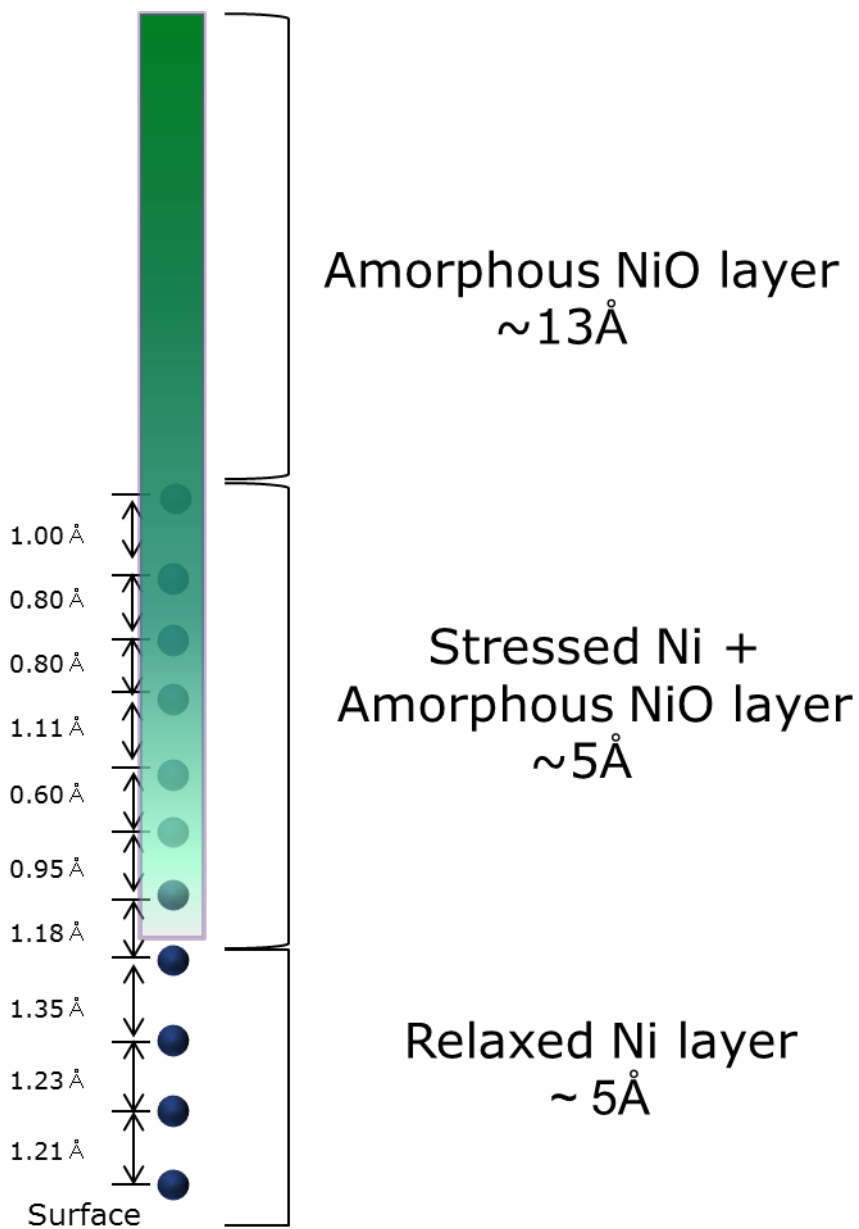
Figure 5-4. Illustration of atom position and thickness of the each layer after fitting
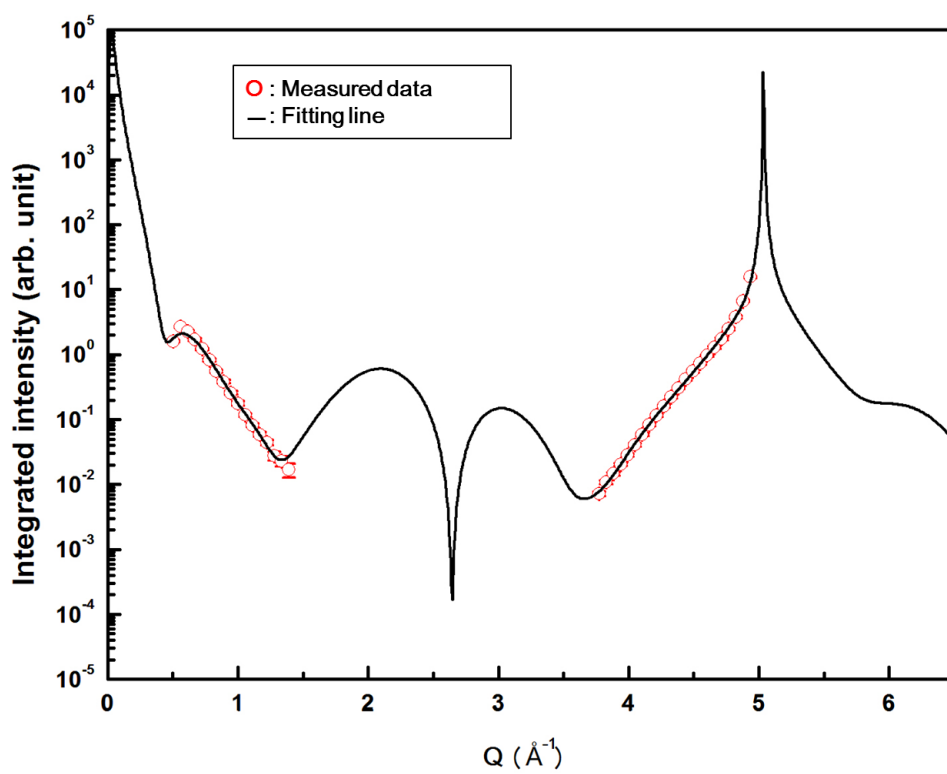
Figure 5-5. The fitting result for Ni(110)/NiO-water structure
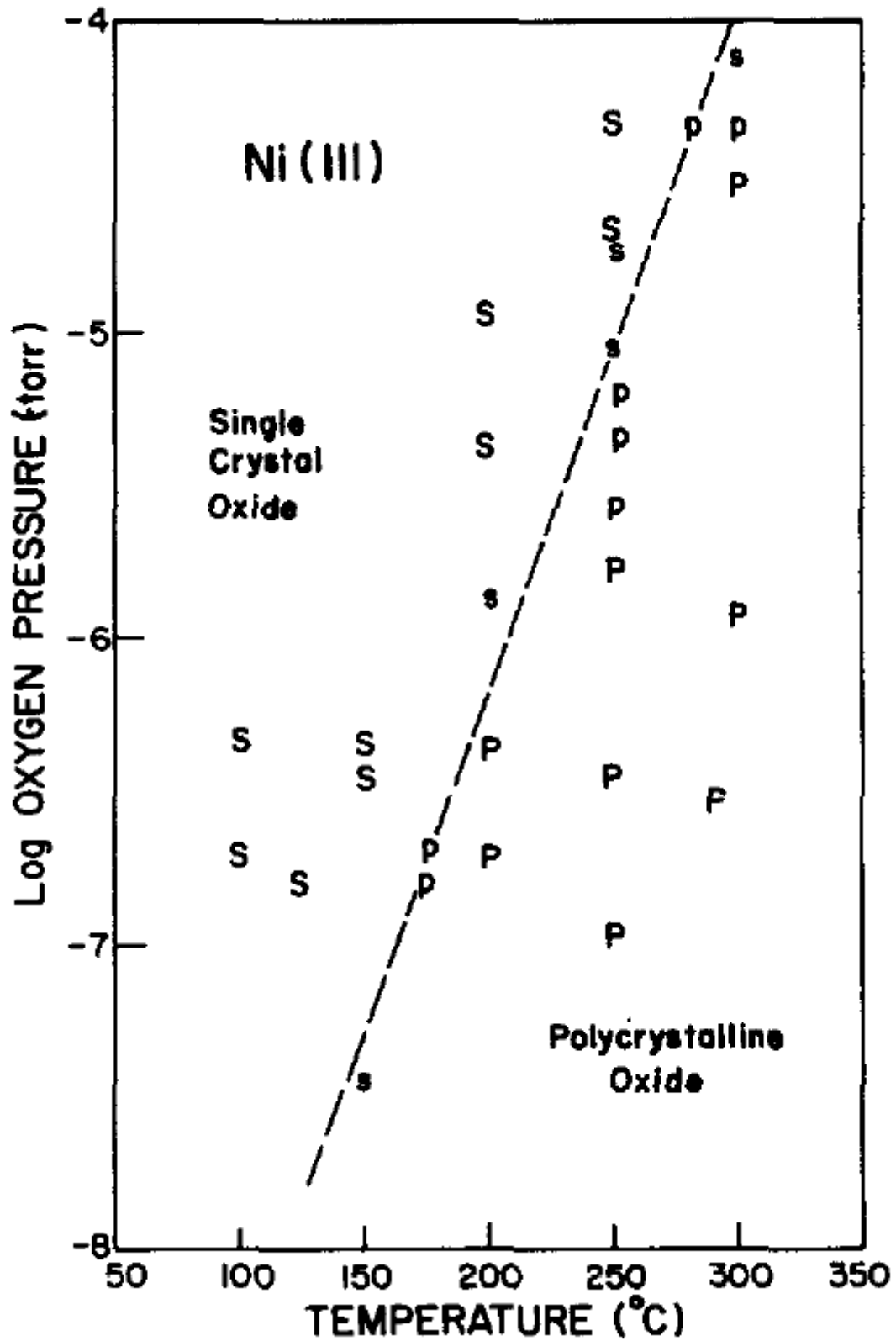
Figure 5-6. Stability regions of single crystal and polycrystalline NiO for oxidation stages 2 and 3 as observed by RHEED. S. single crystal only; s. mostly single crystal, p, mostly polycrystalline; P, polycrystalline only [78]

(a)

94

Eh (Volts)

Fe$_2$O$_3$ (s)

FeO$_2$ (s)

$O_2+4H^++4e^-\rightarrow2H_2O$

Fe^{2+}(aq)

FeCr$_2$O$_4$ (s)

DH=30cc/kg

$2H^++2e^-\rightarrow H_2$

Fe (s)

pH
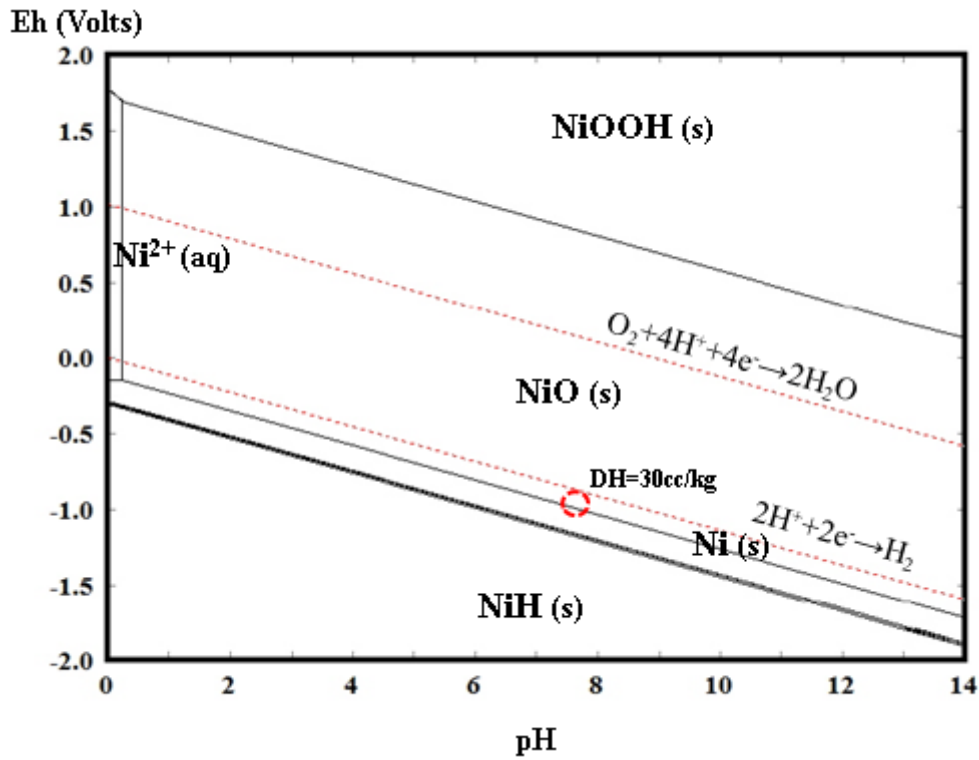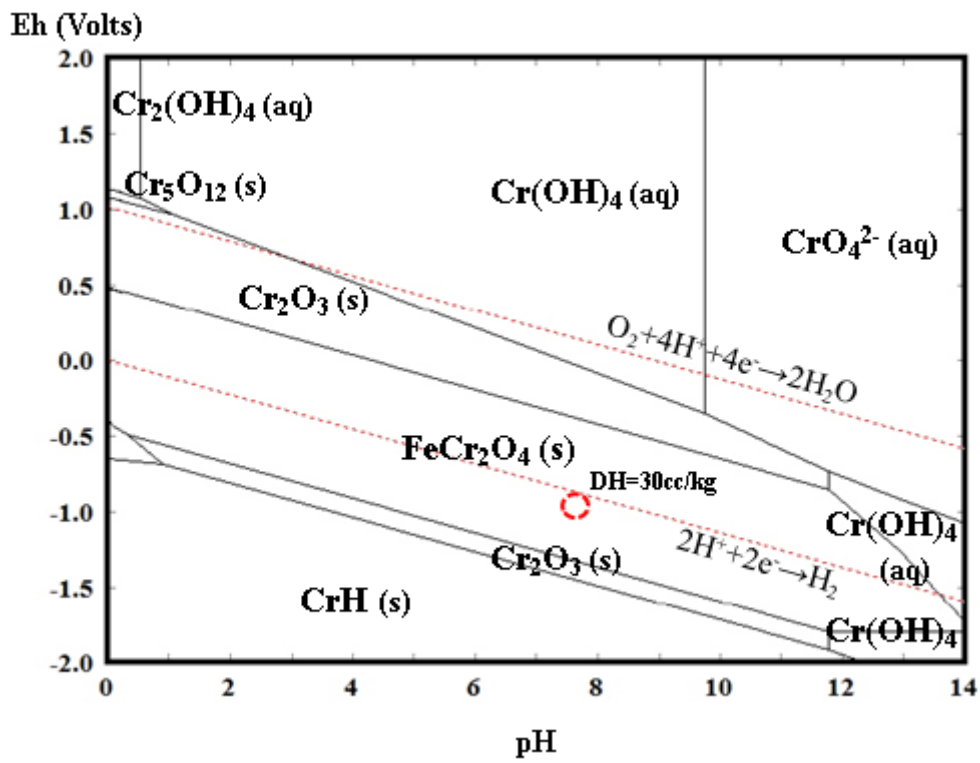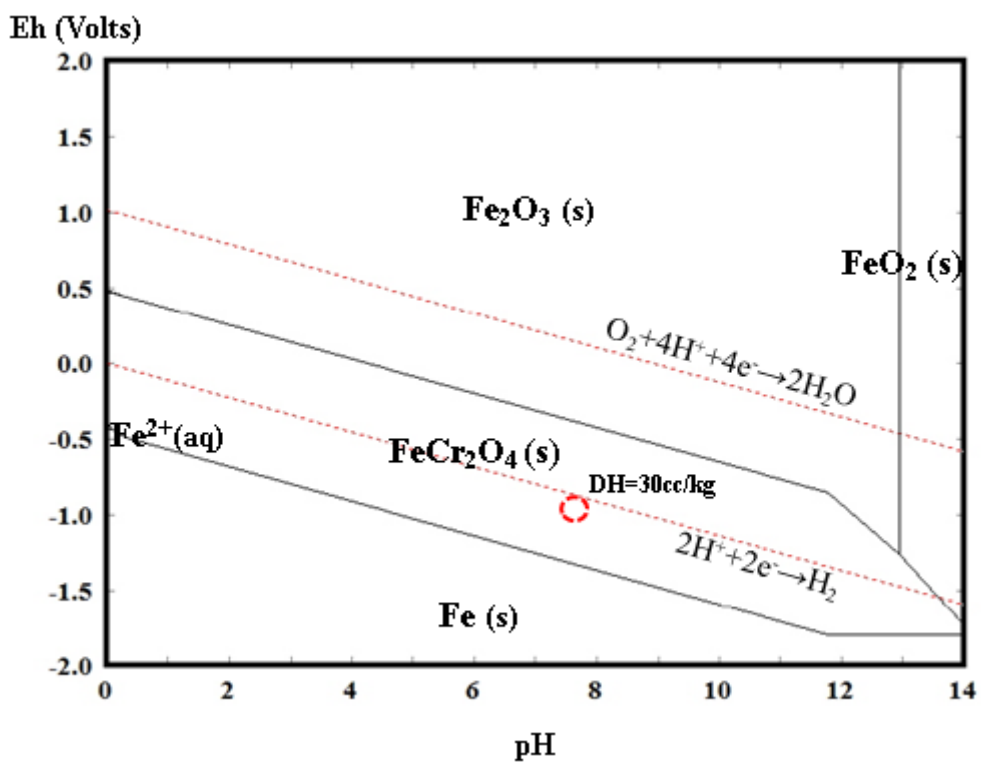
(c)

Figure 5-7. Potential-pH diagram for Ni-Cr-Fe ternary system in water at 300 ℃ for (a) Nickel, (b) Chromium and (c) Iron, the red circles on the diagrams represent the test condition in this study
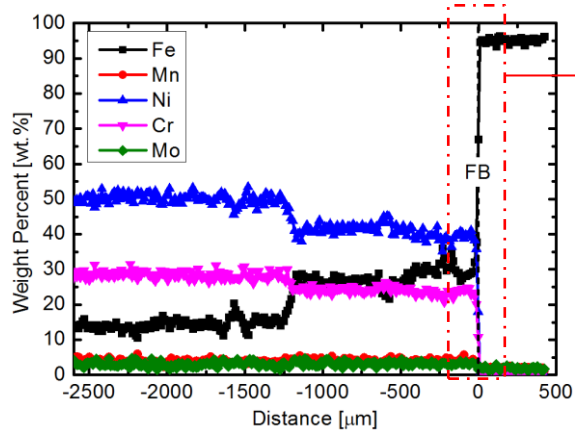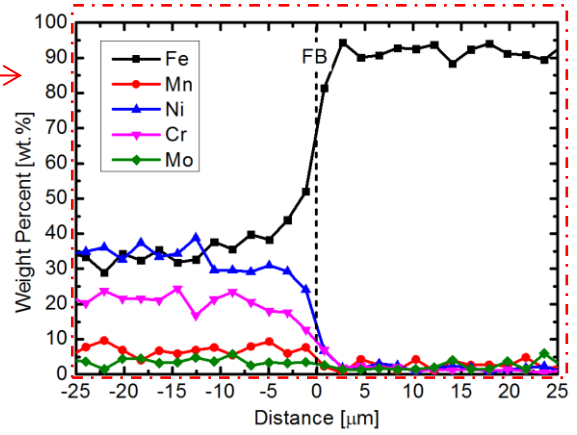
(a)　　　　　　　　　　　　　　　　　　(b)
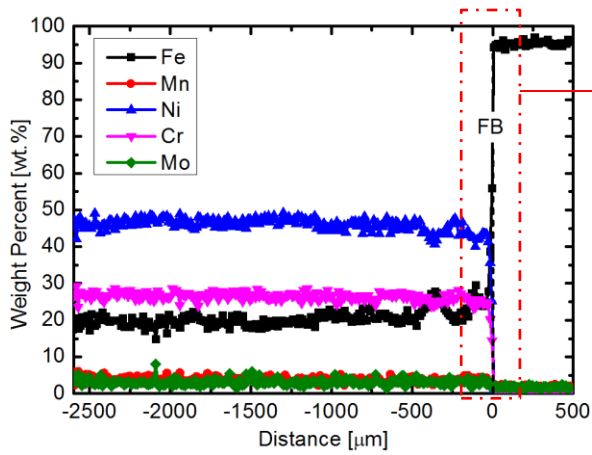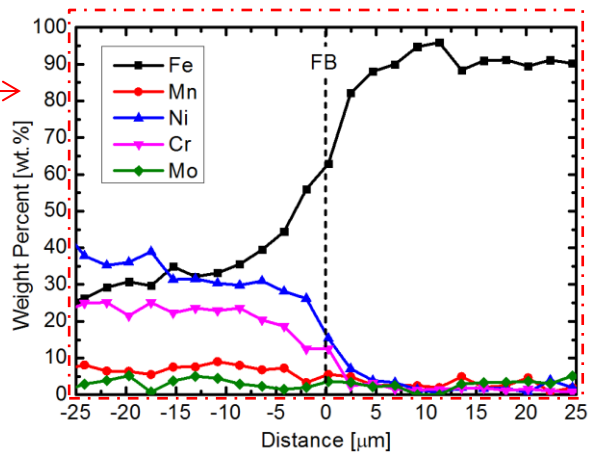
(c)　　　　　　　　　　　　　　　　　　(d)

Figure 5-8. EDS profiles across the interface region of A533Gr.B and Alloy 152 of (a) as-welded and (b) thermally aged DMW interfaces [76]

(a) As-welded DMW   (b) Thermally aged DMW
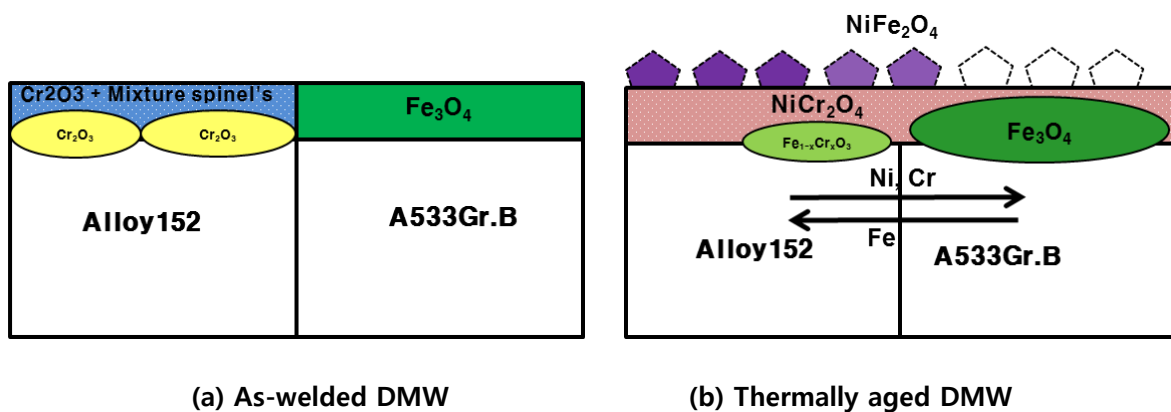
Figure 5-9. Schematic illustration of the oxide layer formed at the interface of DMWs, as suggested by the in situ and ex situ analysis performed in this study

VI. Summary and conclusion

The Synchrotron X-ray reflectivity performed on the Ni(110)/NiO-helium and Ni(110)/NiO-water in order to investigate the atomistic structure change at the interface. To success the X-ray reflectivity measurement at low intensity region, surface treatment method was developed by mechanical-electrochemical polishing and sequence Ar sputtering/annealing. The surface treatment methods to the CTR measurements were confirmed to suitable for the CTR experiments. The CTR measurements were conducted for Ni(110)/NiO structure and for interface of Ni(110)/NiO-water. It was founded that the water can be change the lattice structure of Ni(110)/NiO-water interface.

The atomistic diffusion of oxygen in Ni-Cr binary alloy were modeled and simulated that provides the fundamental insight into the role of chromium atom during the oxidation of nickel-based alloys which are extremely versatile in a wide range of application. In result, it has found that the high oxygen affinity of chromium tends to pulls the oxygen atoms, making it difficult for oxygen diffusion from chromium to nickel in nickel-based alloys and in turn leading to the high corrosion resistance of the alloys. However, the chromium atoms in nickel layer make good condition for internal oxidation phenomena. It is good evidence for the internal oxidation mechanisms in nickel base alloys.

It is investigated that the oxidation behavior of the as-welded/thermally aged Ni-based alloy/low alloy steel DMW by analyzing the oxide film using in situ Raman spectroscopy. The in situ Raman analysis of the surface oxide was conducted at the interface region of the as-welded/thermally aged Ni-based alloy/low alloy steel DME heated to 300 ℃. Furthermore, the ex situ EDS analysis was performed to gain further insight on the results obtained from the Raman spectroscopy. The combined understanding of the in situ and ex situ analyses revealed difference in the oxidation behavior between the as-welded and thermally aged DMW interfaces. The observed difference could be attributed to the diffusion-assisted chemical redistribution at the DMW interface facilitated by thermal aging.

Referring to previous result of films formed on A600 and A690, the oxide films formed in thermally aged DMW showed the similarity to that of A600, and it can be considered that thermally aged DMW is relatively more susceptible to SCC occurrence than as-welded one. It can be consider that the internal oxidation phenomena occur easier on thermally aged DMW than on as-welded DMW. According to the first-principles calculation results, the chromium or chromium oxide can take a role of diffusion barrier, and the chromium atoms in nickel layer make good condition for internal oxidation, and from the in-situ Raman results, the oxide films on the thermally aged DMW are manly Ni-rich spinels without chromium oxide. That is, the oxide films on the DMW easily occurs the internal oxidation phenomena and it causes decrease the SCC resistance.

Reference

[1]   H. X. a. S. Fyfitch, "Laboratory Investigation of PWSCC of CRDM Nozzle 3 and Its J-Groove Weld on the Davis-Besse Reactor Vessel Head," *Proceedings of the 12th International Conference on Environmental Degaradation of Materials in Nuclear Power Systems (Warrendale, PA: The Minerals, Metals, and Materials [TMS],* 2005.

[2]   T. M. Angeliu, P. L. Andresen, and F. P. Ford, "Applying slip-oxidation to the SCC of austenitic materials in BWR/PWR environments," *Corrosion 98,* 1998.

[3]   P. M. Scott and M. Le Calvar, "Some possible mechanisms of intergranular stress corrosion cracking of alloy 600 in PWR primary water," *Proc. Specialist Meeting on Environmental Degradation of Alloy,* 1994.

[4]   P. M. Scott, "An overview of internal oxidation as a possible explanation of intergranular stress corrosion cracking of alloy 600 in PWRs," *9th International Symposium on Environmental Degradation of Materials in Nuclear Power Systems -Water Reactors,* p. 387, 1999.

[5]   G. Was, T. M. Angeliu, and J. K. Sung, "Deformation and intergranular cracking behavior of Ni-Cr-Fe alloys at high temperature," *Proceedings of the "Specialist Meeting on Environmental Degradation of Alloy 600", Airlie House, Va, April 1993,* pp. 24-1, 1996.

[6]   M. M. Hall Jr, "Thermally Activated Low Temperature Creep and Primary Water Stress Corrosion Cracking of Ni Cr Fe Alloys," *Alloy 600 Expert Meeting, April 6-9, (1993), Airlie Conference Center,* 2009.

[7]   P. A. Fenter, "X-ray reflectivity as a probe of mineral-fluid interfaces: A user guide," *Review in mineralogy and geochemistry,* 2002.

[8]   H. You, R. P. Chiarello, H. K. Kim, and K. G. Vandervoort, "X-ray reflectivity and scanning-tunneling-microscope study of kinetic roughening of sputter-deposited gold films during growth," *Physical Review Letters,* vol. 70, pp. 2900-2903, 05/10/ 1993.

[9]   R. P. Chiarello and N. C. Sturchio, "The calcite (10$\bar{1}$4) cleavage surface in water: Early results of a crystal truncation rod study," *Geochimica et Cosmochimica Acta,* vol. 59, pp. 4557-4561, 11// 1995.

[10]   C. Vericat, M. E. Vela, G. A. Andreasen, R. C. Salvarezza, F. Borgatti, R. Felici*, et al.*, "Following Adsorption Kinetics at Electrolyte/Metal Interfaces through Crystal Truncation Scattering: Sulfur on Au(111)," *Physical Review Letters,* vol. 90, p. 075506, 02/21/ 2003.

[11]   C. A. Lucas, N. M. Marković, and P. N. Ross, "The adsorption and oxidation of carbon monoxide at the Pt(111)/electrolyte interface: atomic structure and surface relaxation,"

Surface Science, vol. 425, pp. L381-L386, 4/9/ 1999.

[12]   S. L. Medway, C. A. Lucas, A. Kowal, R. J. Nichols, and D. Johnson, "In situ studies of the oxidation of nickel electrodes in alkaline solution," *Journal of Electroanalytical Chemistry,* vol. 587, pp. 172-181, 2/1/ 2006.

[13]   L. Pauling and E. B. Wilson, "Introduction to Quantum Mechanics with Applications to Chemistry.," 1963.

[14]   P. Hohenberg and W. Kohn, "Inhomogeneous Electron Gas," *Physical Review,* vol. 136, pp. B864-B871, 11/09/ 1964.

[15]   W. Kohn and L. J. Sham, "Self-Consistent Equations Including Exchange and Correlation Effects," *Physical Review,* vol. 140, pp. A1133-A1138, 11/15/ 1965.

[16]   E. H. Megchiche, M. Amarouche, and C. Mijoule, "First-principles calculations of the diffusion of atomic oxygen in nickel: thermal expansion contribution," *J Phys Condens Matter,* vol. 19, p. 296201, Jul 25 2007.

[17]   Y. Mishin, A. Y. Lozovoi, and A. Alavi, "Evaluation of diffusion mechanisms in NiAl by embedded-atom and first-principles calculations," *Physical Review B - Condensed Matter and Materials Physics,* vol. 67, pp. 142011-142019, 2003.

[18]   M. W. Finnis, A. Y. Lozovoi, and A. Alavi, "The oxidation of NiAl: What can we learn from ab initio calculations?,"   vol. 35, ed, 2005, pp. 167-207.

[19]   S. Choudhury, L. Barnard, J. D. Tucker, T. R. Allen, B. D. Wirth, M. Asta*, et al.*, "Ab-initio based modeling of diffusion in dilute bcc Fe–Ni and Fe–Cr alloys and implications for radiation induced segregation," *Journal of Nuclear Materials,* vol. 411, pp. 1-14, 2011.

[20]   C. S. Kumai and T. M. Devine, "Oxidation of Iron in 288℃, Oxygen-Containing Water," *Corrosion,* vol. 61, pp. 201-218, 2005/03/01 2005.

[21]   C. S. Kumai and T. M. Devine, "Influence of Oxygen Concentration of 288℃ Water and Alloy Composition on the Films Formed on Fe-Ni-Cr Alloys," *Corrosion,* vol. 63, pp. 1101-1113, 2007/12/01 2007.

[22]   J. E. Maslar, W. S. Hurst, W. J. Bowers Jr, J. H. Hendricks, M. I. Aquino, and I. Levin, "In situ Raman spectroscopic investigation of chromium surfaces under hydrothermal conditions," *Applied Surface Science,* vol. 180, pp. 102-118, 2001.

[23]   J. E. Maslar, W. S. Hurst, W. J. Bowers, and J. H. Hendricks, "In situ Raman spectroscopic investigation of stainless steel hydrothermal corrosion," *Corrosion,* vol. 58, pp. 739-747, 2002.

[24]   J. E. Maslar, W. S. Hurst, W. J. Bowers, J. H. Hendricks, and M. I. Aquino, "In situ Raman spectroscopic investigation of aqueous iron corrosion at elevated temperatures and pressures," *Journal of the Electrochemical Society,* vol. 147, pp. 2532-2542, 2000.

[25] J. E. Maslar, W. S. Hurst, W. J. Bowers, J. H. Hendricks, and M. I. Aquino, "In situ Raman spectroscopic investigation of nickel hydrothermal corrosion," *Corrosion,* vol. 58, pp. 225-231, 2002.

[26] J. H. Kim and I. S. Hwang, "Development of an in situ Raman spectroscopic system for surface oxide films on metals and alloys in high temperature water," *Nuclear Engineering and Design,* vol. 235, pp. 1029-1040, 4// 2005.

[27] V. Maurice, H. Talah, and P. Marcus, "Ex situ STM imaging with atomic resolution of Ni(111) electrodes passivated in sulfuric acid," *Surface Science,* vol. 284, pp. L431-L436, 3/20/ 1993.

[28] V. Maurice, H. Talah, and P. Marcus, "A scanning tunneling microscopy study of the structure of thin oxide films grown on Ni(111) single crystal surfaces by anodic polarization in acid electrolyte," *Surface Science,* vol. 304, pp. 98-108, 3/1/ 1994.

[29] F.-R. F. F. Sheuh-Lin Yaun, Thomas P. Moffat, and Allen J. Bard, "In situ scanning tunneling microscopy of Ni(100) in 1M NaOH," *J. Phys. Chem. ,* vol. 98, 1994.

[30] D. Zuili, V. Maurice, and P. Marcus, "In situ Scanning Tunneling Microscopy Study of the Structure of the Hydroxylated Anodic Oxide Film Formed on Cr(110) Single-Crystal Surfaces," *The Journal of Physical Chemistry B,* vol. 103, pp. 7896-7905, 1999/09/01 1999.

[31] O. M. Magnussen, J. Scherer, B. M. Ocko, and R. J. Behm, "In Situ X-ray Scattering Study of the Passive Film on Ni(111) in Sulfuric Acid Solution," *The Journal of Physical Chemistry B,* vol. 104, pp. 1222-1226, 2000/02/01 2000.

[32] T. Suzuki, T. Yamada, and K. Itaya, "In Situ Electrochemical Scanning Tunneling Microscopy of Ni(111), Ni(100), and Sulfur-Modified Ni(100) in Acidic Solution," *The Journal of Physical Chemistry,* vol. 100, pp. 8954-8961, 1996/01/01 1996.

[33] J. Scherer, B. M. Ocko, and O. M. Magnussen, "Structure, dissolution, and passivation of Ni(111) electrodes in sulfuric acid solution: an in situ STM, X-ray scattering, and electrochemical study," *Electrochimica Acta,* vol. 48, pp. 1169-1191, 4/20/ 2003.

[34] V. Maurice and P. Marcus, "Passive films at the nanoscale," *Electrochimica Acta,* vol. 84, pp. 129-138, 12/1/ 2012.

[35] P. A. Fenter, *Applications of synchrotron radiation in low-temperature geochemistry and environmental sciences* vol. 49: Geochemical Society, 2002.

[36] C. Park and P. A. Fenter, "Phasing of resonant anomalous X-ray reflectivity spectra and direct Fourier synthesis of element-specific partial structures at buried interfaces," *Journal of Applied Crystallography,* vol. 40, pp. 290-301, 2007.

[37] Z. Zhang, P. Fenter, S. D. Kelly, J. G. Catalano, A. V. Bandura, J. D. Kubicki, *et al.*, "Structure of hydrated Zn2+ at the rutile TiO2 (110)-aqueous solution interface: Comparison

of X-ray standing wave, X-ray absorption spectroscopy, and density functional theory results," *Geochimica et Cosmochimica Acta,* vol. 70, pp. 4039-4056, 8/15/ 2006.

[38]   P. Fenter, C. Park, L. Cheng, Z. Zhang, M. P. S. Krekeler, and N. C. Sturchio, "Orthoclase dissolution kinetics probed by in situ X-ray reflectivity: effects of temperature, pH, and crystal orientation," *Geochimica et Cosmochimica Acta,* vol. 67, pp. 197-211, 1/15/ 2003.

[39]   C. Park, P. A. Fenter, N. C. Sturchio, and K. L. Nagy, "Thermodynamics, Interfacial Structure, and pH Hysteresis of Rb+ and Sr2+ Adsorption at the Muscovite (001)−Solution Interface," *Langmuir,* vol. 24, pp. 13993-14004, 2008/12/16 2008.

[40]   S. S. Lee, P. Fenter, C. Park, N. C. Sturchio, and K. L. Nagy, "Hydrated Cation Speciation at the Muscovite (001)−Water Interface," *Langmuir,* vol. 26, pp. 16647-16651, 2010/11/16 2010.

[41]   A. Bouzoubaa, B. Diawara, V. Maurice, C. Minot, and P. Marcus, "Ab initio study of the interaction of chlorides with defect-free hydroxylated NiO surfaces," *Corrosion Science,* vol. 51, pp. 941-948, 4// 2009.

[42]   C. D. Taylor, R. G. Kelly, and M. Neurock, "First-Principles Prediction of Equilibrium Potentials for Water Activation by a Series of Metals," *Journal of The Electrochemical Society,* vol. 154, pp. F217-F221, December 1, 2007 2007.

[43]   T. M. Pollock and S. Tin, "Nickel-based superalloys for advanced turbine engines: Chemistry, microstructure, and properties," *Journal of Propulsion and Power,* vol. 22, pp. 361-374, 2006.

[44]   Y. Shu, F. Wang, and W. Wu, "Corrosion behavior of pure Cr with a solid NaCl deposit in O2 plus water vapor," *Oxidation of Metals,* vol. 54, pp. 457-471, 2000.

[45]   F. H. Stott and C. Y. Shih, "High-temperature corrosion of iron-chromium alloys in oxidizing-chloridizing conditions," *Oxidation of Metals,* vol. 54, pp. 425-443, 2000.

[46]   L. Zheng, C. Xiao, G. Zhang, B. Han, and D. Tang, "Primary α phase and its effect on the impact ductility of a high Cr content cast Ni-base superalloy," *Journal of Alloys and Compounds,* vol. 527, pp. 176-183, 2012.

[47]   L. G. H. Coriou, L. Legall and S. Vettier, "Stress corrosion cracking of Inconel in high temperature water," *Jeme collooque de metallurgie, Saclay, France,* p. 161, 1959.

[48]   P. Arnoux, "Atomistic simulations of stress corrosion cracking," *Corrosion Science,* vol. 52, pp. 1247-1257, 2010.

[49]   K. Li, X. Du, Y. Yan, H. Wang, Q. Zhan, and H. Jin, "First-principles study on ferromagnetism in C-doped AlN," *Physics Letters A,* vol. 374, pp. 3671-3675, 2010.

[50]   H. Peng, "First-principles study of native defects in rutile TiO2," *Physics Letters A,* vol. 372, pp. 1527-1530, 2008.

[51]   G. A. Young, W. W. Wilkening, D. S. Morton, E. Richey, and N. Lewis, "The Mechanism and

Modeling of Intergranular Stress Corrosion Cracking of Nickel-Chromium-Iron Alloys Exposed to High-Purity Water," *Proc. 12th Int. Symp. on Environmental Degradation of Materials in Nuclear Power Systems (Warrendale, PA: The Minerals, Metals, and Materials [TMS],* 2005.

[52]   S. Garruchet, O. Politano, P. Arnoux, and V. Vignal, "Diffusion of oxygen in nickel: A variable charge molecular dynamics study," *Solid State Communications,* vol. 150, pp. 439-442, 2010.

[53]   P. Laghoutaris, J. Chêne, C. Guerre, O. Raquet, M. Sennour, R. Molins, *et al.*, "Contribution to understanding of stress corrosion cracking of Alloy 600 in PWR primary water," *Energy Materials: Materials Science and Engineering for Energy Systems,* vol. 3, pp. 119-125, // 2008.

[54]   G. Kresse, Furthm, uuml, and J. ller, "Efficient iterative schemes for ab initio total-energy calculations using a plane-wave basis set," *Physical Review B,* vol. 54, p. 11169, 1996.

[55]   G. Kresse and J. Hafner, "Ab initio molecular dynamics for liquid metals," *Physical Review B,* vol. 47, pp. 558-561, 1993.

[56]   J.J. Kim, S.H. Shin, J.A. Jung, K.J. Choi, and J.H. Kim, "First-principles study of interstitial diffusion of oxygen in nickel chromium binary alloy," *Applied Physics Letters,* vol. 100, 2012.

[57]   W. Kohn and L. J. Sham, ""Self-consistent equations including exchange and correlation,"" *Phys. Rev. B,* 2006.

[58]   P. E. Blöchl, "Projector augmented-wave method," *Physical Review B,* vol. 50, pp. 17953-17979, 1994.

[59]   G. Kresse and D. Joubert, "From ultrasoft pseudopotentials to the projector augmented-wave method," *Physical Review B - Condensed Matter and Materials Physics,* vol. 59, pp. 1758-1775, 1999.

[60]   K. Burke, J. P. Perdew, and Y. Wang, "Derivation of a generalized gradient approximation: The PW91 density functional," *Electronic Density Functional Theory: Recent Progress and New Directions,* pp. 81-111, 1998.

[61]   M. Černý, Pokluda, J., Šob, M. Friák, M. and Šandera, "Ab initio calculations of elastic and magnetic properties of Fe, Co, Ni, and Cr crystals under isotropic deformation," *Phys. Rev. B 67,* vol. 67, pp. 151161-351168, 2003.

[62]   E. H. Megchiche, S. Pérusin, J. C. Barthelat, and C. Mijoule, "Density functional calculations of the formation and migration enthalpies of monovacancies in Ni: Comparison of local and nonlocal approaches," *Physical Review B - Condensed Matter and Materials Physics,* vol. 74, 2006.

[63]   H. J. Monkhorst and J. D. Pack, "Special points for Brillouin-zone integrations," *Physical Review B,* vol. 13, pp. 5188-5192, 1976.

[64]   G. Henkelman, G. Jóhannesson, and H. Jónsson, "Methods for finding saddle points and minimum energy paths," *Progress in Theoretical Chemistry and Physics,* vol. 5, pp. 269-300, 2000.

[65]   G. Henkelman, B. P. Uberuaga, and H. Jónsson, "Climbing image nudged elastic band method for finding saddle points and minimum energy paths," *Journal of Chemical Physics,* vol. 113, pp. 9901-9904, 2000.

[66]   P. L. A. R.M. Horn, and J. Hickling, "BWR alloy 182 stress corrosion cracking experience," *Proc. 5th Int. Symp. on Contribution of Materials Investigation to the Resolution of Problems Encountered in Pressurized Water Reators(Fontevraud 5), Fontevraud, France, Sep. 23 - 27,* 2002.

[67]   J. Hou, Q. Peng, Y. Takeda, J. Kuniya, and T. Shoji, "Microstructure and stress corrosion cracking of the fusion boundary region in an alloy 182-A533B low alloy steel dissimilar weld joint," *Corrosion Science,* vol. 52, pp. 3949-3954, 2010.

[68]   Q. Peng, H. Xue, J. Hou, K. Sakaguchi, Y. Takeda, J. Kuniya*, et al.*, "Role of water chemistry and microstructure in stress corrosion cracking in the fusion boundary region of an Alloy 182-A533B low alloy steel dissimilar weld joint in high temperature water," *Corrosion Science,* vol. 53, pp. 4309-4317, 2011.

[69]   J. J. K. K.J. Choi, S.H.Shin, S.I.Choi, J.H. Kim, "Nano Structural and Nano-chemical Analysis of Ni-base alloy/Low Alloy Steel Dissimilar Metal Weld Interfaces," *Nuclear Engineering and Technology,* vol. 44, pp. 491-500, 2012.

[70]   K.J. Choi, J.J. Kim, S.H.Shin, S.I.Choi, J.H. Kim, "Three Dimensional Atom Probe Study Of Ni-Base Alloy/Low Alloy Steel Dissimilar Metal Weld Interfaces," *Nuclear Engineering and Technology,* pp. 673-682, 2012.

[71]   H. Shah Hosseini, M. Shamanian, and A. Kermanpur, "Characterization of microstructures and mechanical properties of Inconel 617/310 stainless steel dissimilar welds," *Materials Characterization,* vol. 62, pp. 425-431, 2011.

[72]   M. Sireesha, S. K. Albert, V. Shankar, and S. Sundaresan, "Comparative evaluation of welding consumables for dissimilar welds between 316LN austenitic stainless steel and Alloy 800," *Journal of Nuclear Materials,* vol. 279, pp. 65-76, 2000.

[73]   A. M. Al-Rumaih and M. A. Al-Anezi, "Environmental cracking of dissimilar metal welds," *Saudi Aramco Journal of Technology,* pp. 2-11, 2008.

[74]   S. R. H.P. Seifert, T. Shoji, Q.J. Peng, Y. Takeda, and   Z.P. Lu, "Environmentally-assisted

cracking behaviour in the transition region of an Alloy182/SA 508 Cl.2 dissimilar metal weld joint in simulated boiling water reactor normal water chemistry environment," *Journal of Nuclear Materials,* vol. 378, pp. 197-210, 2008.

[75]   A. S. o. M. E. (ASME), "Welding and Brazing Qualifications" *Boiler and Pressure Vessel Code (BPVC), Section IX,* 2010.

[76]   K. J. Choi, J. J. Kim, B. H. Lee, C. B. Bahn, and J. H. Kim, "Effects of thermal aging on microstructures of low alloy steel-Ni base alloy dissimilar metal weld interfaces," *Journal of Nuclear Materials,* vol. 441, pp. 493-502, 2013.

[77]   A. Barbier, C. Mocuta, H. Kuhlenbeck, K. F. Peters, B. Richter, and G. Renaud, "Atomic Structure of the Polar NiO(111)-p(2x2) surface," *Physical Review Letters,* vol. 84, pp. 2897-2900, 03/27/ 2000.

[78]   D. F. Mitchell and M. J. Graham, "A kinetic study of the initial oxidation of Ni (111) and (211) surfaces by rheed and X-ray emission," *Surface Science,* vol. 114, pp. 546-562, 2/1/ 1982.

[79]   J. C. Sauerwein, "Standard reference data publications," *NBS special publication 708, Suppl. 1,* 1986.

[80]   B. Chattopadhyay and G. C. Wood, "The transient oxidation of alloys," *Oxidation of Metals,* vol. 2, pp. 373-399, 1970.

[81]   H. K. a. H. Langer, "Alloy Phase Diagrams " *ASM Handbook 3,* 1992.

[82]   S. Dai, Y. Xiang, and D. J. Srolovitz, "Structure and energy of (111) low-angle twist boundaries in Al, Cu and Ni," *Acta Materialia,* 2012.

[83]   R. L. McCreery, "Calibration and Validation," in *Raman Spectroscopy for Chemical Analysis*, ed: John Wiley & Sons, Inc., 2005, pp. 251-291.

[84]   G. Lucazeau, "Effect of pressure and temperature on Raman spectra of solids: anharmonicity," *Journal of Raman Spectroscopy,* vol. 34, pp. 478-496, 2003.

[85]   M. Sennour, L. Marchetti, F. Martin, S. Perrin, R. Molins, and M. Pijolat, "A detailed TEM and SEM study of Ni-base alloys oxide scales formed in primary conditions of pressurized water reactor," *Journal of Nuclear Materials,* vol. 402, pp. 147-156, 7/31/ 2010.

[86]   F. Wang, "In-situ surface enhanced Raman spectroscopy investigation of the surface films on alloy600 and alloy690 in pressurized water reactor-primary water," *Electronic thesis and dissertations UC Berkeley,* 2012.

Acknowledgement (감사의 글)

2009년 3월, 아직 완공 되지도 않은 UNIST의 자연과학관에서 Nuclear engineering text book을 처음 접했던 때가 엊그제 같은데, 어느덧 박사학위를 수여 받으며 졸업하는 날이 오게 되네요. 이 정도로 될까 싶은 걱정, 열심히 하자는 다짐, 그 동안 도움 주신 분들에 대한 한없는 고마움 등이 모여 형언할 수 없는 기분을 느낍니다.

한걸음 한걸음 나아갈 때 마다 끊임없이 격려해 주시고 난관에 부딪힐 때 마다 그 난관을 뚫는 방법을 깨우치도록 해주시며, 지치고 힘들 때 마다 온화한 미소와 무뚝뚝함 속에 베어있는 자상함으로 감싸주신 김지현 교수님께 감사 드리며 진심으로 존경합니다. 교수님께서 주신 많은 배움의 기회와 베풀어주신 은혜는 가슴 깊이 세기며, 원자력에 크게 공헌하여 부끄럽지 않은 제자가 되도록 최선을 다하겠습니다. 그리고, 귀중한 시간을 내주시어 항상 학생들의 올바른 마음가짐과 자세, 원자력의 안전한 이용 등 많은 부분에서 조언을 아끼지 않아 주신 방인철 교수님 감사 드립니다. 많이 바쁘신 와중에도 시간 내 주시어 항상 꼼꼼히 논문 내용을 살펴 주시며, 미국에서 한두 달 체류하며 실험을 할 때에도 많은 가르침 주시고, 음식 때문에 고생할까 맛있는 한식을 해주셨던, 반치범 교수님과 사모님 은혜 잊지 않겠습니다. 감사합니다. 또한 처음 계산과학을 접해 헤매고 있을 때 나아가야 할 방향과 방법을 제시해주신 권준현 박사님, 귀한 시간 내주셔서 논문의 구성을 잡아주셨던 권순용 교수님, 논문에 서명해주시면서 이제부터 시작이야 라고 해주셨던 말씀 명심하고 초심으로 돌아가 열심히 하도록 하겠습니다. 정말 감사 드립니다.

UNIMAT! 운전 중 번뜩 떠올라 제안한 이름이 우리 랩의 이름이 되고 교수님 그리고 제자 둘로 시작되었던 연구실이 10명의 연구실이 되었네요 돌이켜보면 참 짧은 5년.. 그 동안에 많은 사람들과 함께 교감하며 즐겁고도 소중한 시간을 보낼 수 있었던 것 같습니다. 먼저 개교와 함께 같이 들어온, 우리 1기 3명. 먼저 졸업한 열수력의 이승원 박사님, 우리 연구실 상훈 형. 함께 나눈 많은 얘기들 그 동안 함께 어려움 헤쳐나간 경험들이 앞으로 많은 도움이 될 것 같습니다. 그리고 우리 연구실 후배들.. 경준, 상일, 승현 태호, 광범 너희들이 없었으면 실험 못 했을지 몰라 정말 고맙다. 이제 입학을 앞둔 승창, 정현, 재선. 지금 먼저 들어와 있는 선배들 잘 따르고 배우면 너희도 곧 잘 적응 할거라 믿는다. 연구실 먼저 졸업해서 사회생활을 하고 있는 정석형, 주앙이 함께 했던 시간들이 너무 그립고 우리 연구실과 단짝인 열수력 연구실의 든든한 맴버들, 성대, 사라, 한, 경모,

106

인국, 성보, 영신, 효. 너무 고맙고 하는 일 다 잘되길 바랍니다. 406호 같이 쓰며 동거동락한 방사선 랩의 동한 형, 욱제 핵연료 랩의 병진, 주영, 제균, 태원, 지현 고맙습니다. 그리고 바쁜 시간 내줘서 clean room에서 니켈 표면처리를 도와주셨던 권순용 교수님 연구실 곽진성 박사님 그리고 재환이 덕분에 좋은 X-ray 실험결과를 얻었어요. 정말 고맙습니다. 미국 Argonne 연구소의 Hongping, 박창용 박사님 정말 감사합니다. 그 외에도 일일이 열거를 할 수 없을 정도로 많은 UNIST 분들께 도움을 받았습니다. 정말 감사드립니다.

처음 연구실 꾸미고 실험해 나갈 때 아무런 노하우 없어 전전긍긍할 때 많은 도움을 주었던 서울대 연구실의 남효온 박사님, 원창형님, 재영이 정말 감사합니다. 그리고 많은 노하우를 전수해 주고, 실험실 셋팅 등 많은 부분에서 도움을 받았던 KAIST 연구실의 장훈 박사님, 종대 정말 감사합니다.

고등학교 때부터 지금까지 10년 넘게 우정을 변함없이 지켜오고 있는, 진명, 창원, 도현, 도환, 우열, 대경, 준영, 장희, 웅빈아 힘들 때 마다 너희들과 기울이는 술 한잔이 무엇보다 큰 힘이 되었어. 정말 고맙다.

아버지 어머니, 두분 덕분에 잘 크고 바르게 성장했으며 행복을 느낍니다. 항상 사위 걱정해주시는 장인어른, 묵묵히 사위 믿어주시는 장모님께도 감사 드립니다. 못난 오빠를 항상 믿어주는 동생 진희, 친형처럼 대해주는 우리 처남. 항상 고마워. 항상 챙겨주셨던 작은 아버지, 어머니, 큰고모, 작은고모. 공부하고 있으면 잘 하고 있는지 아버지처럼 와서 봐주셨던 큰외삼촌, 작은외삼촌 내외분, 항상 맛난 것 사주셨던 우리 이모들 정말 감사합니다. 마지막으로 함께 박사과정 공부중인 나의 사랑하는 아내. 시선. 자기 덕분에 잘 마칠 수 있었어요. 앞으로도 같이 연구하는 학자로, 사랑하는 연인으로, 다정다감한 친구로 늘 함께 합시다. 고맙고 사랑합니다.

2014년 2월

김종진